10-2011

Large–Scale Laboratory Observations of Wave Forces on a Highway Bridge Superstructure

Chris Bradner
Oregon State University

Thomas Schumacher
Portland State University, thomas.schumacher@pdx.edu

Daniel Cox
Oregon State University

Christopher Higgins
Oregon State University

Recommended Citation

Bradner, Chris, Thomas Schumacher, Daniel Cox and Christopher Higgins. Large–Scale Laboratory Observations of Wave Forces on a Highway Bridge Superstructure. OTREC RR-11-10. Portland, OR: Transportation Research and Education Center (TREC), 2011. https://doi.org/10.15760/trec.81

OTREC

FINAL REPORT

OREGON
TRANSPORTATION
RESEARCH AND
EDUCATION CONSORTIUM

Large–Scale Laboratory Observations of Wave Forces on a Highway Bridge Superstructure

OTREC-RR-11-10
October 2011

A National University Transportation Center sponsored by the U.S. Department of Transportation's Research and Innovative Technology Administration

LARGE-SCALE LABORATORY OBSERVATIONS OF WAVE FORCES ON A HIGHWAY BRIDGE SUPERSTRUCTURE

Final Report

OTREC-RR-11-10

by

Chris Bradner
Thomas Schumacher
Daniel Cox
Chris Higgins
Oregon State University

for

Oregon Transportation Research
and Education Consortium (OTREC)
P.O. Box 751
Portland, OR 97207

OTREC
OREGON TRANSPORTATION RESEARCH
AND EDUCATION CONSORTIUM

October 2011

Technical Report Documentation Page

1. Report No. OTREC-RR-11-10	2. Government Accession No.	3. Recipient's Catalog No.
4. Title and Subtitle LARGE-SCALE LABORATORY OBSERVATIONS OF WAVE FORCES ON A HIGHWAY BRIDGE SUPERSTRUCTURE		5. Report Date October 2011 6. Performing Organization Code
7. Author(s) Chris Bradner Thomas Schumacher Daniel Cox Chris Higgins		8. Performing Organization Report No.
9. Performing Organization Name and Address Oregon State University School of Civil & Construction Engineering 220 Owen Hall Corvallis, OR 97331-3212		10. Work Unit No. (TRAIS) 11. Contract or Grant No. 2008-161
12. Sponsoring Agency Name and Address Oregon Transportation Research and Education Consortium (OTREC) P.O. Box 751 Portland, Oregon 97207		13. Type of Report and Period Covered Final Report 14. Sponsoring Agency Code
15. Supplementary Notes		

16. Abstract

The experimental setup and data are presented for a laboratory experiment conducted to examine realistic wave forcing on a highway bridge superstructure. The experiments measure wave conditions along with the resulting forces, pressures, and structural response of a 1:5 scale, reinforced concrete model of a typical section of the I-10 Bridge over Escambia Bay, Florida that failed during Hurricane Ivan in 2004. A unique feature of this model is its roller and rail system which allowed the specimen to move freely along the axis of wave propagation to simulate the dynamic response of the structure. The data are analyzed to study the relative importance of the impulse load versus the sustained wave load, the magnitudes of the horizontal to vertical forces, and their time histories to identify the modes of failure. The thesis examines the relationship between measured forces and wave momentum flux. The measured forces are also compared to recently published AASHTO guidelines. The author evaluates the distribution of forces under random wave conditions and proposes a method that calculates design loads based on exceedance probabilities.

17. Key Words Hurricane Wave Forces, Coastal Hazards, Coastal Infrastructure, Natural Disasters, Hurricane Katrina, Highway Bridges, Large Scale Experiments		18. Distribution Statement No restrictions. Copies available from OTREC: www.otrec.us	
19. Security Classification (of this report) Unclassified	20. Security Classification (of this page) Unclassified	21. No. of Pages 166	22. Price

ACKNOWLEDGEMENTS

This project was jointly funded by the Oregon Transportation Research and Education Consortium (OTREC), the Kiewit Center for Infrastructure and Transportation, and the National Science Foundation (CMMI-0800822). The efforts of the O.H. Hinsdale Wave Research Laboratory staff (Linda Fayler, Jason Killian and Sungwon Shin) in assisting with the experiments are greatly appreciated. The work of Julie Barlow in preparing the final report is greatly appreciated.

DISCLAIMER

TABLE OF CONTENTS

LIST OF TABLES

LIST OF FIGURES

EXECUTIVE SUMMARY

The experimental setup and data are presented for a laboratory experiment conducted to examine realistic wave forcing on a highway bridge superstructure. The experiments measure wave conditions along with the resulting forces, pressures, and structural response of a 1:5 scale, reinforced concrete model of a typical section of the I-10 Bridge over Escambia Bay, FL, which failed during Hurricane Ivan in 2004. A unique feature of this model is its roller and rail system, which allowed the specimen to move freely along the axis of wave propagation to simulate the dynamic response of the structure. The data are analyzed to study the relative importance of the impulse load versus the sustained wave load, the magnitudes of the horizontal to vertical forces, and their time histories to identify the modes of failure. The thesis examines the relationship between measured forces and wave momentum flux. The measured forces are also compared to recently published AASHTO (American Association of State Highway and Transportation Officials) guidelines. The author evaluates the distribution of forces under random wave conditions and proposes a method that calculates design loads based on exceedance probabilities.

1.0 INTRODUCTION

During Hurricanes Ivan in 2004 and Katrina in 2005, at least 11 highway and railroad bridges along the U.S. Gulf Coast were damaged by a combination of storm surge and wave action (*Douglass et al., 2004; Padgett et al., 2008*). Damage to these bridges ranged from moderate to catastrophic and necessitated over $850 million in repairs and replacement costs (*Florida DOT, 2008; Padgett et al., 2008*). Figure 1.1 shows the location of the major bridges damaged. The damaged bridges shared three common characteristics:

1. Each structure consisted of a series of simply supported, noncontinuous concrete spans.

2. The connections between superstructure and the bent caps were inadequate, or in some cases nonexistent.

3. The bottom elevation of the spans was at or near the storm surge elevation.

The design of the spans varied from bridge to bridge, but in general each superstructure element was composed of a reinforced concrete deck supported by multiple, prestressed concrete girders oriented parallel to the direction of traffic and transverse to the principal wave loading. A typical connection between the superstructure and the supporting bent cap consisted of bolted bearing plates with shear keys, but in some cases the spans simply rested on the bent caps, with no physical connections to resist uplift or lateral forces (*Douglass et al., 2006; NIST, 2006*). Inspections of the damaged bridges found that the failure of the bent cap connections was the specific cause of the overall failure (*Douglass et al., 2006; Chen et al., in press; Robertson et al., 2007*).

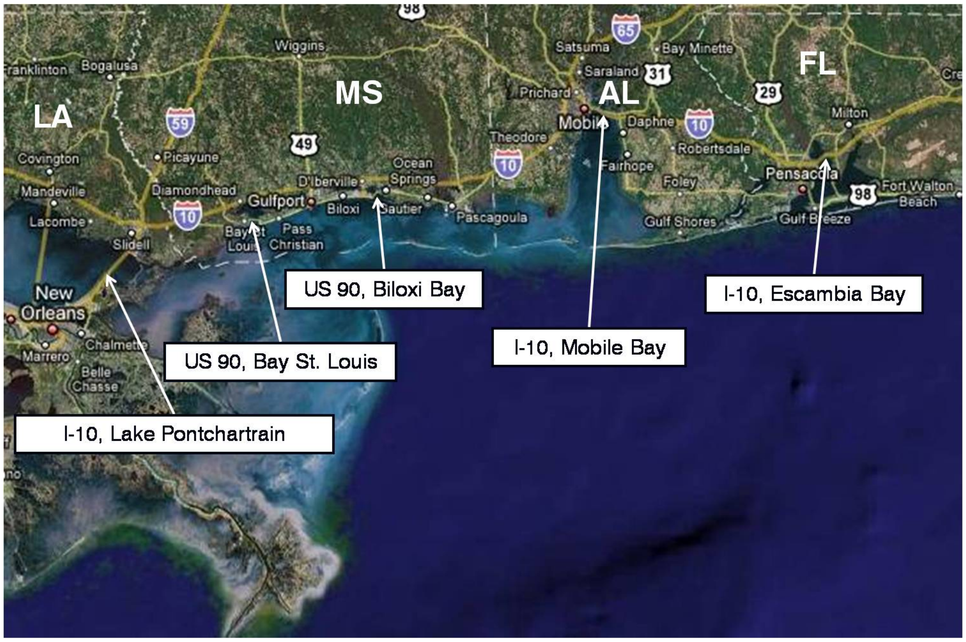

Figure 1.1. Major highway bridges damaged along the U.S. Gulf Coast during Hurricanes Ivan and Katrina (Source: Google Maps)

Preliminary analysis of these failures indicated that the low elevation of the superstructure relative to the mean water level (MWL) was a significant factor (*Douglass et al., 2006; Chen et al., in press; Robertson et al., 2007*). Historic storm surges during Hurricanes Ivan and Katrina raised the water level to elevations that approached or exceeded the low chord of the girders (*Douglass et al., 2004; Graumann, et al., 2005; Douglass et al., 2006*). This increase in water level not only allowed the waves to strike the superstructure, it also allowed larger depth-limited waves to be generated by the hurricane winds in the (normally) shallow waters where the bridges were located. In cases where the MWL exceeded the bottom of the superstructure, the storm surge produced an uplift force due to buoyancy, which countered the dead weight of the structure. Buoyancy may have been enhanced by air pockets trapped between the girders and diaphragms. For some of the bridge spans that failed, self weight and resulting friction were the only sources of resistance to uplift and lateral forces, respectively. Investigations of the failure mechanism for theses bridges theorize that the uplift force due to buoyancy combined with the horizontal and vertical hydrodynamic forces due to impacting waves imposed a large enough force to overcome the weight of a bridge superstructure element and the capacity of any bent cap connections (Douglass *et al*., 2006; NIST, 2006). Once the bent cap connections failed, subsequent waves were able to push the element off of the supporting bents caps. Figure 1.2 shows the damage to the U.S. 90 Bridge over Biloxi Bay, MS, caused by Hurricane Katrina.

Figure 1.2. Damage to the U.S. 90 Biloxi Bay Bridge caused by Hurricane Katrina (courtesy of Solomon Yim, Oregon State University).

The National Institute of Standards and Technology (NIST) inspected the bridges damaged during Hurricane Katrina and found that because the bridge superstructure elements were pre-cast offsite and then placed on the supporting bent caps, each span acted independently in failure, with little interaction between spans (*NIST, 2006*). The I-10 Bridge over Escambia Bay, FL, that failed during Hurricane Ivan also exhibited this independent behavior, as shown in Figure 1.3.

While some of the bridge superstructures were completely inundated at the peak of the storm surge, both the I-10 Bridge over Escambia Bay and the U.S. 90 Bridge over Biloxi Bay are believed to have failed while the MWL was below the bottom of the superstructure (*Douglass et al., 2004; OEA, Inc., 2005; Douglass et al., 2006*). This would suggest that the hydrodynamic wave forces alone were large enough to cause failure for these bridges.

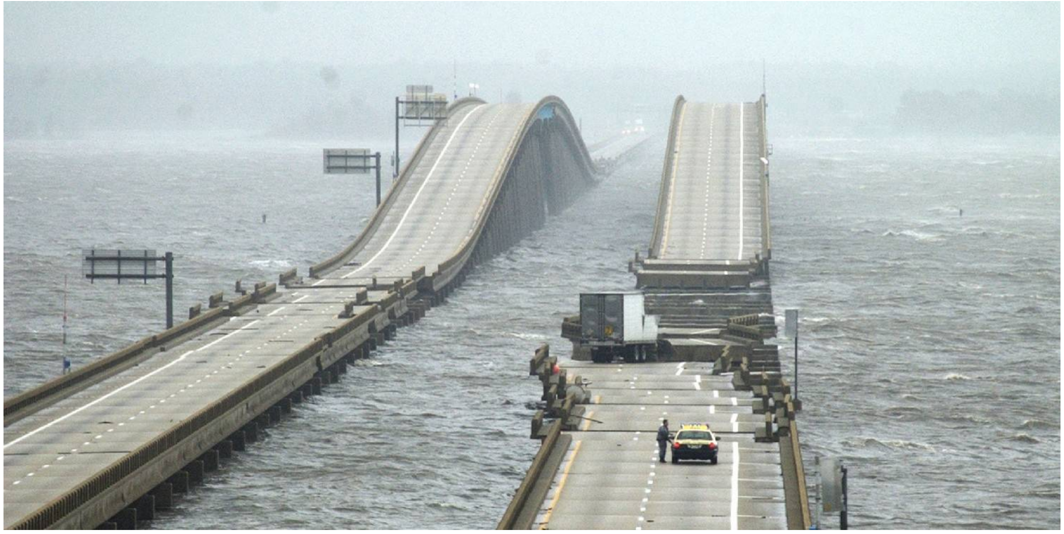

Figure 1.3. I-10 Bridge over Escambia Bay, FL, during Hurricane Ivan. (Source: Pensacola News Journal)

Since 2005, many of the damaged bridges, including the I-10 Bridge over Escambia Bay, the U.S. 90 Bridge over Biloxi Bay, and the U.S. 90 Bridge at Bay St. Louis, have been replaced by bridges with significantly higher superstructure clearance. While the storm surge of future hurricanes will not likely reach the superstructures of these new bridges, dozens of existing bridges are still vulnerable to storm surge and it may not always be practical to design future bridges with a large clearance. To prevent future failures of coastal bridges during storms, engineers must first be able to estimate the forces on the structure. These forces are the focus of this thesis. The experimental setup and plan are described in detail. The measured loads are presented and analyzed to determine a relationship with commonly available wave parameters. The loads are also compared to new guidelines published by the American Association of State Highway and Transportation Officials (AASHTO). In an effort to predict design forces based on acceptable risk, loads measured under random wave conditions are fitted to a probability distribution and exceedance probabilities are computed. The research described herein represents a first step towards estimating the hydrodynamic wave forces on a realistic highway bridge superstructure.

2.0 LITERATURE REVIEW

Calculation of the hydrostatic forces due to buoyancy is a straightforward analytical process, but accurate estimation of the hydrodynamic forces is far more difficult. While previous research on forces associated with flat plates (*Shih & Anastasiou, 1992*), circular members (*Kaplan, 1992*), and offshore platforms (*Bea et al., 1999*) has developed analysis methods, these may not be well suited for bridges. Highway bridge superstructures pose a unique challenge due to their complex geometries, bluff profile, and their relatively large width-to-wavelength ratio. When the added complexities of trapped air, turbulence and structural response are incorporated, analytical solutions become impractical and available empirical solutions based on small-scale experiments may be biased by scale effects. Finite element modeling may be able to provide accurate force estimates, but these models must be calibrated using data from physical models. Unfortunately, very few experimental studies are available with high-quality measurements of wave loads for realistic bridge geometries.

Douglass et al. (2006)

Douglass *et al*. (2006) investigated the bridge failures of Hurricanes Ivan and Katrina and estimated the forces required to cause such damage. Using numerical models to hindcast storm surge, significant wave height and peak period, the report estimated the environmental conditions at the bridges during the hurricanes. The report also conducted a review of existing methods to predict wave forces on structures and analyzed their applicability to bridge superstructures. After concluding that none of the reviewed methods would accurately predict the observed damage, the report presents interim guidance for calculation of horizontal and vertical, quasi-static and impact forces on bridge superstructures. The equations contain empirical coefficients based on the hindcast wave heights and water depths and the estimated forces commensurate with damage observed in the field. The coefficients were further supported by data collected from small-scale experiments presented by McConnell *et al*. (2004). The report also recommends that additional, more sophisticated experiments be performed. Among the suggestions for future experiments were the modelling of support stiffness and the measurement of bridge accelerations.

Cuomo et al. (2007)

Cuomo *et al*. (2007) did not specifically study coastal highway bridges, but their work on wave-in-deck loads on exposed piers may be applicable to bridges. The article presents a new method for determining both impact and quasi-static forces, based on data from a small-scale physical model. Wave forces and pressures were measured on a 1:25 scale wooden deck with cross and longitudinal down-standing beams. Horizontal and vertical forces were measured on internal and seaward elements. Unfortunately, overturning moment could not be calculated with the experimental setup presented. Pressures were measured with two pressure transducers mounted in the face of the seaward beam. Overall forces were estimated by applying these local forces and pressures over the appropriate surface area. The study found the forces to be dependent on wave height and the clearance between the superstructure and the still water level (SWL).

AASHTO (2008)

AASHTO has developed a series of equations to calculate design loads on coastal bridges due to waves (*AASHTO, 2008*). The equations are designed to calculate:

1. Maximum vertical quasi-steady force with the associated horizontal force, overturning moment and vertical slamming force.

2. Maximum horizontal quasi-steady force with the associated vertical force, overturning moment and vertical slamming force.

These equations are parameterizations of a physics-based model (PBM) derived from Kaplan's equations of wave forces on platform deck structures, originally developed for offshore oil platforms (*Kaplan, 1992; Kaplan et al., 1995*). The PBM was developed at the University of Florida and was verified through a series of 2-D experiments conducted on a 1:8 scale model of a section of the I-10 Bridge over Escambia Bay, FL.

The equations account for the bridge span design (slab vs. girder), as well as the type of girders used. The geometry of the bridge span is also considered, including girder depth, span width, and rail height. Other input factors include wave height, wave crest elevation, bridge elevation, and wave length. The equations also account for the effect of trapped air between the girders. A Trapped Air Factor (TAF) is calculated and is applied to the quasi-steady vertical forces. The TAF is a function of wave height, bridge elevation, and bridge geometry. The recommended application of the TAF allows the designer to calculate a range of quasi-steady vertical forces, based on a minimum and maximum TAF. While the guidance is specific on calculating the range, it is left to the designer to determine the specific TAF used to calculate the forces.

Even with the recent efforts described above, there is still relatively little quantitative measurement of wave loads on realistic bridge decks available. Many of the existing methods rely on models that are small in scale or are not representative of a typical highway bridge superstructure. The system of girders and diaphragms that support the bridge deck create a complex hydraulic problem that calls for a geometrically realistic model. Small-scale experiments may experience scale effects that reduce the accuracy of their results.

In some models, the methods used to measure forces may also be a source of error. Commonly, forces are indirectly determined by integrating locally measured pressures over the surface of the structure. The turbulent flows around a bridge superstructure can create complex, non-uniform surface pressure distributions, leading to inaccuracies in force calculations. Pressures recorded during wave impacts can also be misleading. Past research has shown that pressures due to wave impact followed a common pattern of an initial, short-duration, high-amplitude, impact pressure followed by longer-duration quasi-static pressure (*McConnell et al., 2004; Cuomo et al., 2007*). The significance of the impact pressure and its relevance to the bridge failures of Ivan and Katrina is uncertain. The previously mentioned scale effects of compressed air on these impact pressures, combined with the uncertainty of pressure sensor response in a mixed air-water environment, further clouds the issue.

Previous experiments have treated the structural models as rigid, with no dynamic response to the forcing. The structural response of a bridge may have a significant effect on the forces produced at the bent cap connections. The response of bridges mounted on piles can be modeled as a single-degree-of-freedom spring-mass-damper system. Assuming geometric similitude is met, the density of the material used in the model must match that of the prototype to accurately scale the response. Real-world bridges are constructed of reinforced concrete, yet previous models have been fabricated from wood, plastic or metal due to difficulties working with concrete at small scales.

To address this need, researchers at Oregon State University developed an innovative laboratory setup that enables direct measurements of wave forces on a realistic, large-scale bridge superstructure. A large-scale, reinforced concrete, highway bridge superstructure specimen was constructed and tested under regular and random wave conditions over a range of water depths that included inundation of the structure. The experimental setup allowed direct control of the stiffness of the horizontal support system to simulate different dynamic properties of the bridge substructure (columns, bent cap and foundation) thereby allowing the first dynamic testing of bridge structures subjected to wave loads. The data collected will permit comparison with existing analysis and design methods and allow calibration of future numerical simulations.

3.0 EXPERIMENTAL DESIGN

3.1 GENERAL EXPERIMENTAL SETUP AND WAVE FLUME BATHYMETRY

The experiments were conducted in the Large Wave Flume (LWF) at the O.H. Hinsdale Wave Research Laboratory at Oregon State University. The flume is 104 meters (342 ft.) long, 3.66 meters (12 ft.) wide and 4.57 meters (15 ft.) deep. The flap-type wavemaker can produce waves with a maximum height of about 1.6 meters (5.2 ft.) at a wave period of 3.5 s. A 2-D setup was chosen after analysis of the wave conditions at the U.S. 90 Bridge over Biloxi Bay and the I-10 Bridge over Escambia Bay revealed that the wave directions were nearly perpendicular to the faces of the bridge superstructures during the peak of the storms. In addition, the depth of the LWF allowed for realistic large-scale modeling of water depth and wave heights. Beginning at the wavemaker, the bathymetry was comprised of an impermeable 1:12 slope, followed by a horizontal section approximately 30 meters (98 ft.) in length, and then another 1:12 slope to dissipate waves and minimize reflection off the beach. The specimen was located near the center of the horizontal section. Overall dimensions of the LWF and the location of the test frame with the specimen are illustrated in Figure 3.1.

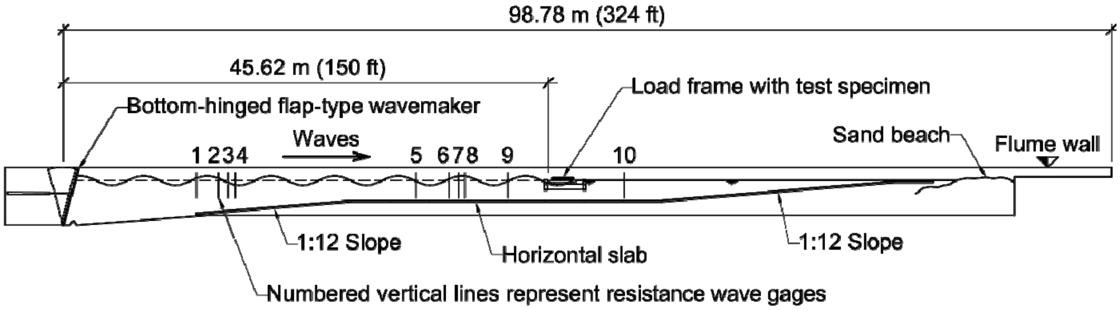

Figure 3.1. Elevation view of wave flume with experimental setup (courtesy of Thomas Schumacher, Oregon State University).

3.2 SCALING

The geometric scaling for this experiment was chosen to allow the testing of a single bridge superstructure element with a representative span length in the LWF. To test the largest scale bridge span possible, a geometric scale of 1:5 (undistorted) was selected. The experiments were designed to be kinematically similar using Froude scaling ($T_{model} = T_{prototype} / \sqrt{5}$).

For the quasi-steady forces related to inertia, dynamic similitude was achieved using Froude scaling. Quasi-steady drag forces were estimated to be insignificant for the conditions tested. Bullock *et al*. (2001) proposes that air between the girders of a bridge, when trapped and compressed by a passing wave, can significantly affect impact (also known as slamming) forces. While there is some debate on the best way to scale the effects of trapped and entrained air, Hughes (1993) suggests using Cauchy scaling when measuring forces due to elastic compression of fluids. Since it is generally impractical to meet both Froude and Cauchy criteria in hydraulic models, the Cauchy criterion is usually disregarded. This is not a problem in most models, as water can be considered incompressible and the role of compressed air is minor, but when modeling wave forces on bridges the role of compressed air may be significant. In small-scale experiments, this discrepancy in Cauchy scaling may result in disproportionately high forces due to the compression of air. Because the scale of these experiments does not lead to significant scale effects, the forces due to compressed air were not separated from inertial forces. All measured forces were scaled using Froude criteria.

3.3 TEST SPECIMEN AND REACTION FRAME

These experiments were a collaborative effort between the Structural and Ocean Engineering programs at Oregon State University. Professor Christopher Higgins and graduate student Thomas Schumacher of the Structural Engineering program designed and oversaw the fabrication and installation of the bridge specimen and reaction frame.

The reinforced concrete test specimen represents a common coastal highway bridge design and is based on prototype dimensions taken from Florida Department of Transportation drawings of the I-10 Bridge over Escambia Bay. Six scaled AASHTO Type III girders, including the full complex cross-sectional geometry, were constructed and connected with twin steel rods through four diaphragms spaced along the span. A cross-section of a typical prototype bridge is shown in Figure 3.2. The total span length, S, of the test specimen was 3.45 meters (11.3 ft.), the width, W, 1.94 meters (6.36 ft.), and the overall height, h_d, 0.28 meters (0.92 ft.). The deck was fastened to the girder and diaphragm sub-assemblage via 13 millimeters (0.5 in.) diameter threaded rods spaced at 0.31 meters (1 ft.) at the edges and 0.46 meters (1.5 ft.) in the center. Figure 3.3 shows the test specimen before assembly. After assembling and placing the specimen on the test frame, all seams between the girders and deck were sealed airtight with silicone. Overall dimensions, weight and mass of the test specimen and corresponding prototype values are given in Table 3.1.

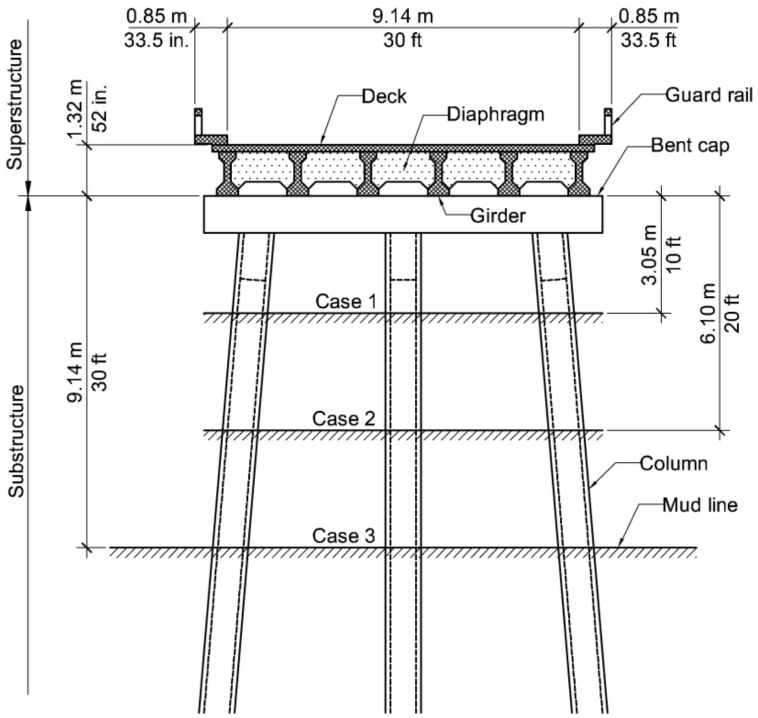

Figure 3.2. Elevation view of typical prototype bridge (courtesy of Thomas Schumacher).

Figure 3.3. Precast bridge specimen prior to attachment of deck.

The test specimen was supported by two HSS7x5x1/2 steel members representing the bent caps. To measure vertical forces, two load cells were mounted underneath each bent cap, in line with the external offshore and onshore girders, respectively. These load cells were mounted on high-precision ball bearing rollers that allowed low-friction motion of the load cells, bent caps and specimen along linear guide rails attached to the top flange of two W18x76 steel profiles (depth = 0.50 m) bolted to each side of the flume wall. To measure horizontal forces, load cells were mounted between the seaward end of the bent caps and end anchorage blocks that were bolted to the flume wall. The test specimen and reaction frame system are shown in Figure 3.4 and Figure 3.5. A photo of the specimen and load frame installed in the LWF can be seen in Figure 3.6.

Table 3.1. Properties of model test specimen (without guard rail) and corresponding prototype bridge

Parameter	**Model (1:5)**		**Prototype (1:1)**	
Total span length, *S*	3.45 m	136 in.	17.27 m	56.7 ft
Span length (simply supported)	3.32 m	131 in.	16.64 m	54.6 ft
Width, *W*	1.94 m	76.4 in.	9.70 m	31.8 ft
Girder height	0.23 m	9.0 in.	1.14 m	45 in.
Girder spacing (CL to CL)	0.37 m	14.4 in.	1.83 m	6.0 ft
Deck thickness	0.05 m	2.0 in.	0.25 m(1)	10 in. (1)
Overall height, h_b	0.28 m	11.0 in.	1.40 m	55 in.
Span weight	19.0 kN	4270 lb	2375 kN	534 kips
Span mass	1940 kg		242 t	

(1) Typical deck thickness is 0.15 m (6 in.)

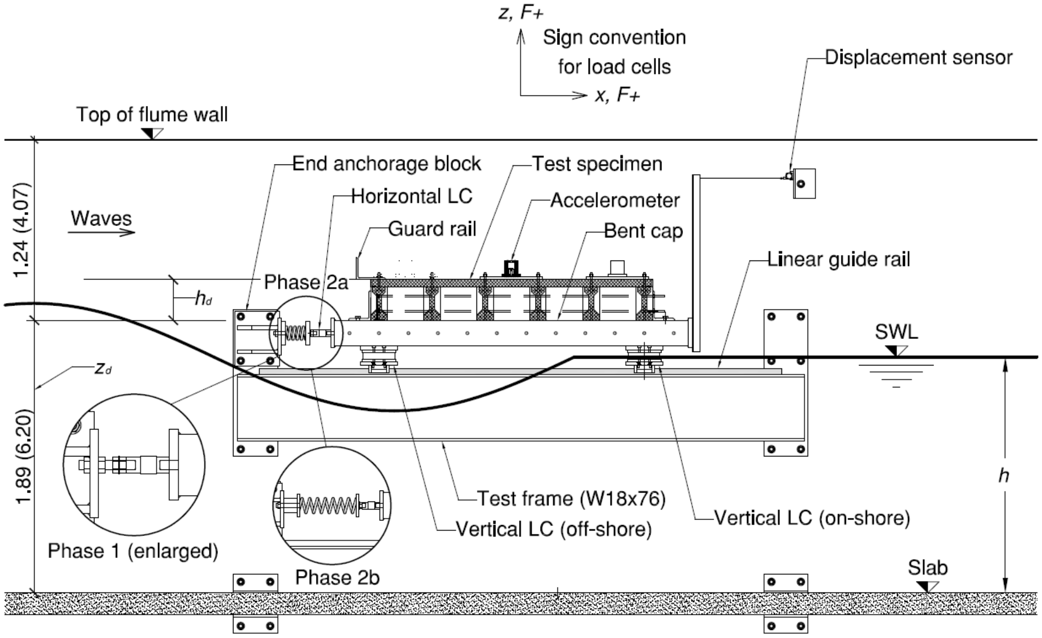

Figure 3.4. Elevation view (side) of test specimen and reaction frame for rigid and dynamic setup. Distances are in m (ft.). (Courtesy of Thomas Schumacher)

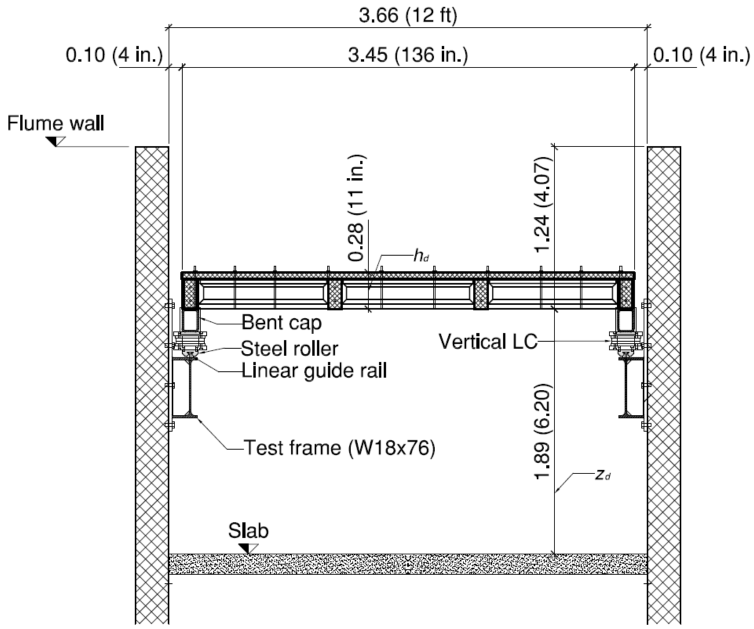

Figure 3.5. Elevation view (end-on) of test specimen with reaction frame and wave flume cross-section. Primary dimensions in meters. (Courtesy of Thomas Schumacher)

The friction force in the linear guide rail system was determined experimentally by disconnecting the lateral force load cells and applying force horizontally to the specimen at the exterior girder centerline. Model displacements were monitored during the friction tests and force was measured with a 2.2 KN (500 lb.) load cell. The mean total, maximum, friction force from 15 replicate tests along different locations along the rail was found to be 450 N (100 lb.) with a standard deviation of 40 N (9 lb.). This force was reached at a displacement of about 3 millimeters (0.1 in.). The force then decreased almost linearly to a mean value of 300 N (67 lb.) with a standard deviation of 50 N (11 lb.) at a displacement of about 20 millimeters (0.8 in.). Depending on the wave period and water-level conditions, the friction of the linear guide rail is between 5% and 10% of the measured peak horizontal forces produced by a wave with a height of 0.6 meters.

Figure 3.6. Photo of rigid test setup installed in Large Wave Flume. In this photo, the horizontal load cell between the bent cap and the end anchorage block has been temporarily replaced by a 1-inch threaded steel rod.

To investigate the effect of substructure flexibility on the wave loading response, a dynamic setup was developed and integrated into the reaction frame. The flexibility of the prototype substructure (bent) was experimentally modeled by a pair of elastic springs. The springs were added to the bent cap-end anchorage block linkage described above, allowing the specimen and bent caps to oscillate along the rail guide. To establish the spring stiffness that would provide a model that was kinematically similar to a realistic prototype, Schumacher performed a finite element (FE) analysis to determine the dynamic properties of the prototype bridge shown in Figure 3.2. The FE model was linear-elastic and the Modulus of Elasticity for concrete was defined as 21,000 MPa (3,046 ksi). The columns were modeled as hollow concrete pipes with an outside diameter of 0.91 m (36 in.) and a wall thickness of 0.13 m (5 in.), and the bent cap as a solid rectangular section with a height and depth of 0.97 m (38 in.) and 0.91 m (36 in.), respectively. The column-bent connections were assumed rigid. The density of the reinforced concrete was assumed as 2,400 kg/m^3 (150 lb./ft.^{3}). Estimated masses based on a prototype span length of 16.64 meters (54.6 ft.) are 223,000 kg (492,000 lb.) for the superstructure, 21,950 kg (48,400 lb.) for the bent caps, and 754 kg/m (507 lb./ft.) for the columns. Using three bent lengths based on actual bridge drawings, the fundamental (first mode) periods, *T*, were calculated and then converted to model scale using Froude criteria. The period for a prototype bridge with a bent length of 9.14 meters (30 ft.) and pinned connections at the foundation was calculated to be 1.01 s, which is kinematically similar to 0.45 s for the scale model. Based on this period, two sets of springs were selected. One set was designed to be relatively soft in order to deliberately exaggerate displacements. The second, stiffer set of springs was chosen to be representative of a realistic bridge substructure. The stiffness of the springs for the test specimen was estimated using the equation for an undamped, lumped mass, single-degree-of-freedom system:

$$K = M\left(\frac{2\pi}{T}\right)^2 \tag{3-1}$$

where K is the total spring stiffness and M the total mass. The total mass for the specimen was estimated to be 2,470 kg (5,445 lb.). The two sets of springs selected for this project had spring constants of 107 kN/m (612 lb./in.) and 458 kN/m (2,614 lb./in.) which produced fundamental periods of 0.95 s and 0.46 s, respectively. A photo of both sets of springs installed in the dynamic setup can be seen in Figure 3.7.

Figure 3.7. Photos of stiff (top photo) and soft (bottom photo) springs installed with horizontal load cell, LC2.

3.4 EXPERIMENTAL PLAN

The experimental plan was designed to meet the major goals of these experiments, which were:

1. Measure the wave-induced forces on a bridge superstructure under realistic conditions.
2. Determine the effect of the dynamic response of the bridge on wave-induced forces.
3. Determine the relative importance of various hydraulic parameters on forces and assess the relationship between these parameters and the resulting forces.
4. Calculate the probability distribution of wave-induced forces under realistic random wave conditions.

The specimen and reaction frame were mounted in the wave flume so that the bottom of the girders was located at z_d = 1.89 meters (6.2ft.) above the horizontal bed to correspond with typical mudline-to-superstructure distances of the failed bridges. Wave conditions and water levels were designed to simulate realistic conditions found at coastal bridges along the Gulf of Mexico during extreme events. Typically these bridges are located in shallow water of 3-10 meters (10-33 ft.) MSL and are somewhat protected by shoals and barrier islands. As a result, waves at these bridges are considerably smaller in height and length relative to ocean waves. Even during catastrophic events such as Hurricane Katrina, numerical modeling by Chen *et al.* (in press) estimates a relatively small maximum significant wave height of 2.6 meters (8.5 ft.) at the U.S. 90 Bridge over Biloxi Bay. Similar wave heights were presented by Ocean Engineering Associates, Inc. (2005) in their report on conditions during Hurricane Ivan at the I-10 Bridge over Escambia Bay. A summary of modeled wave conditions can be found in Table 3.2. Using the conditions hindcast by these models as a guide, a realistic range of wave heights, wave periods and water levels was developed. To represent storm surge, the water depth, *h*, at the specimen was adjusted from 1.61 meters (5.3 ft.) to 2.17 meters (7.1 ft.) in increments of 0.14 meters (5.5 in.) which is equal to one-half the specimen height. The resulting SWL ranged between 0.28 meters (11 in.), below the bottom of the girders to even with the top of the deck. A non-dimensional parameter, d^*, that represents the SWL elevation relative to the bottom of the girders, is equal to

$$d^* = \frac{h - z_d}{h_d} \qquad (3\text{-}2)$$

where z_d is the elevation of the low chord above the mudline and h_d is the height of the bridge deck. For these experiments, values of d^* ranged from -1.0 to +1.0 in increments of 0.5. See Table 3.3 for a summary of corresponding water depths and superstructure clearances.

Table 3.2. Estimated prototype-scale wave conditions at bridges that failed according to numerical models.

Location	**Source**	**H_s (m)**	**H_{max} (m)**	**T_p (s)**
I-10 Escambia Bay	OEA (2005)	1.98	3.97	3.19
U.S. 90 Biloxi Bay	Douglass *et al.* (2006)	2.5-3.0	4.5-5.4*	6.0
U.S. 90 Biloxi Bay	Chen *et al.* (in press)	2.6	4.68*	5.5
U.S. 90 Bay St. Louis	Chen *et al.* (in press)	3.0	N/A	N/A

* assuming Rayleigh distribution of wave heights and one-hour duration

Table 3.3. Values of d* tested and the corresponding water depth and bridge superstructure clearance. A positive value for clearance indicates that the low chord of the superstructure was above the SWL.

d*	**Water Depth, *h* (m)**	**Superstructure Clearance (m)**
-1.0	1.61	+0.28
-0.5	1.75	+0.14
0	1.89	0.00
+0.5	2.03	-0.14
+1.0	2.17	-0.28

For each of the five water depths, regular and random wave conditions were tested. The range of conditions for the regular wave trials was selected to approximate the range of wave heights and periods of the wave spectra at the failed bridges during storms. The random wave conditions were designed to evaluate forces under a range of realistic conditions, with an emphasis on the estimated conditions at the U.S. 90 Bridge over Biloxi Bay during Hurricane Katrina. Random wave trials consisted of a series of approximately 300 waves with a TMA spectrum ($\gamma = 3.3$). Figure 3.8 shows the matrix of measured regular and random wave conditions tested at $d^* = 0.0$. This water level was the most thoroughly investigated, but the range of conditions tested at other water levels was similar. For the regular wave trials, target wave height (H) and period (T) ranged from 0.25 to 1.0 meters (0.8 to 3.3 ft.) and 2.0 to 4.5 s, respectively. Target significant wave height (H_s) and peak period (T_p) ranged from 0.375 to 1.0 meters (1.2 to 3.3 ft.) and 2.0 to 3.0 s, respectively. A summary of parameters is listed in Table 3.4.

Wave heights were limited at the lower water levels to avoid wave breaking, and at the higher water levels to prevent spillage over the top of the wave flume walls. Wave condition matrices for all of the water levels can be found in Appendix A.

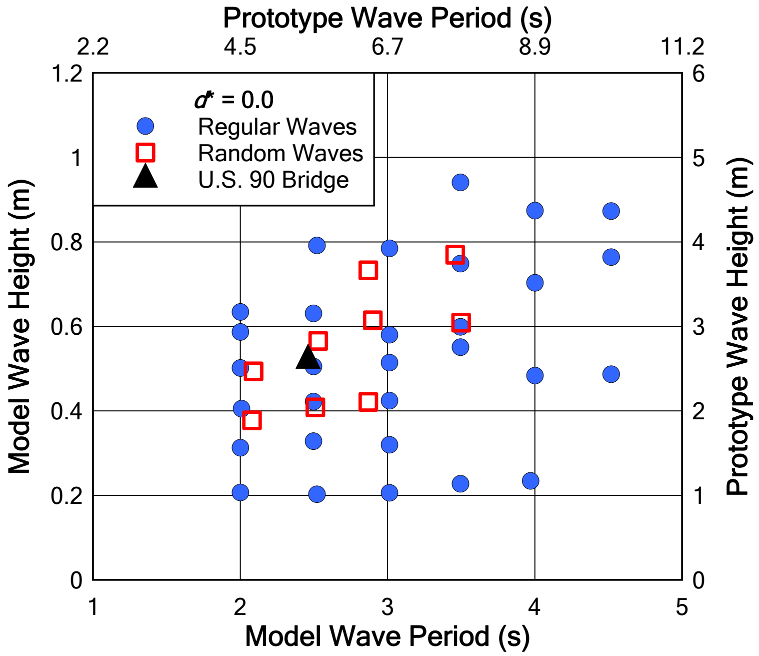

Figure 3.8. Matrix of measured wave conditions for trials conducted at d* = 0.0, Phase 1. Wave height and period for regular wave trials are mean values. Wave height and period for random wave trials are Hs and Tp, respectively. "U.S. 90 Bridge" indicates Hs and Tp at the U.S. 90 Bridge over Biloxi Bay during Hurricane Katrina as estimated by Chen et al. (in press).

The experiments were divided into three phases according to substructure flexibility. Phase 1 simulated a rigid structure. The test specimen was bolted to the bent caps using steel angles, and each bent cap was then connected to an end anchorage block via a load cell. Phase 2a and 2b simulated a flexible substructure using the previously described stiff and soft springs, respectively. Phase 3 was designed to simulate realistic response of the bridge span upon failure of the bent cap connections. For this phase, the bent caps were rigidly connected to the end anchorages as in Phase 1, but the concrete test specimen was disconnected from the bent caps with only the specimen self-weight and the resulting friction providing resistance. The different setups are summarized in Table 3.5.

Table 3.4. Range of model and prototype test conditions.

Test parameter	**Symb.**	**Model (1:5)**	**Prototype (1:1)**
Water depth	h	1.60 - 2.17 m (5.25 – 7.12 ft)	8.0 – 10.9 m (26.2 – 35.6 ft)
Bottom girder clearance to SWL	d_c	± 0.279 m (± 0.92 ft)	±1.4 m (± 4.6 ft)
Wave height [1]	H	0.25 - 1.0 m (0.82 to 3.28 ft)	1.25 - 5.0 m (4.1 to 16.4 ft)
Significant wave height [2]	H_s	0.375 - 1.0 m (1.23 to 3.28 ft)	1.9 - 5.0 m (6.2 to 16.4 ft)
Wave period [1]	T	2.0 - 4.5 s	4.5 – 10.1 s
Peak wave period [2]	T_p	2.0 - 3.0 s	4.5 – 6.7 s

[1] For regular wave trials [2] For random wave trials

Table 3.5. Variations in the experimental setup of horizontal support for the test specimen.

Phase	**Horizontal support**	**Horizontal Stiffness**	**Fundamental Period**	**Connection: Test specimen - bent cap**
1	Rigid	∞*	0.0*	Fixed (rigid)
2a	Dynamic, medium springs	458 (kN/m)	0.46 s	Fixed (rigid)
2b	Dynamic, soft springs	107 (kN/m)	0.95 s	Fixed (rigid)
3	Unconstrained	N/A	N/A	None (free, held by gravity and friction)

* theoretical value

To test the effect of guard railing on the wave-induced forces, a limited number of trials were conducted with a guardrail installed on the model. The guardrail was modeled using a 0.15 meters (6 in.) steel angle mounted on the seaward edge of the specimen deck. The rail configuration was tested at $d^* = 0$ for select regular and random wave trials during all three phases of the experiment.

3.5 INSTRUMENTATION

The sensor suite was designed to measure wave conditions, forces and pressures acting on the specimen, and the corresponding response of the specimen. The different sensors deployed for the experiments are shown in Table 3.6.

Table 3.6. Instrumentation used for experiment, by experiment phase.

Gauge/sensor	**Location**	**Total #**	**Phase**
Wavemaker displacement	Wavemaker flap	1	All
Resistance wave gauges	See Table 3.7	11	All
Sonic wave gauge	Mounted by WG5	1	2, 3
Pressure transducers	Test specimen deck and girders	13	All
Load cells (horizontal)	Between bent cap and end anchorage block	2	All
Load cells (vertical)	Between bent cap and linear guide rail system	4	All
Strain gauges	Test specimen girders	11	All
Displacement sensors	Test specimen deck, on-shore side	2	2, 3
Bi-axial accelerometers	Test specimen deck, top surface	3	2, 3
Acoustic emission sensors	Bent caps	4	3

3.5.1 Wave gauges

To measure water surface elevation, 10 surface piercing resistance wave gauges (WG) were placed along the length of the flume. WG 1-8 were arranged into two arrays of four and positioned offshore of the specimen to resolve incident and reflected waves at two locations. The number and spacing of the gauges in each array was chosen to provide maximum flexibility in the calculation of the incident and reflected wave spectra using the method presented in Mansard and Funke (1980). WG 9 was placed approximately 4 meters (13 ft.) offshore of the specimen to measure water surface elevation in the vicinity of the specimen, and WG10 was located 6 meters (20 ft.) onshore of the specimen. See Table 3.7 for locations of all of the gauges.

Table 3.7. Location of wave gauges relative to the wavemaker. Test specimen was located at x = 46 m (151 ft.).

Gauge #	x-coordinate		Comment/Location
0	0.00 m	0.00 ft	At the wavemaker
1	12.50 m	41.0 ft	Offshore Goda array
2	14.63 m	48.0 ft	Offshore Goda array
3	15.54 m	51.0 ft	Offshore Goda array
4	16.16 m	53.0 ft	Offshore Goda array
5	33.25 m	109 ft	Nearshore Goda array
6	36.29 m	119 ft	Nearshore Goda array
7	37.21 m	122 ft	Nearshore Goda array
8	37.82 m	124 ft	Nearshore Goda array
9	41.86 m	137 ft	Offshore side of test specimen
10	53.89 m	177 ft	Onshore side of test specimen

3.5.2 Load cells

Six hermetically sealed, tension-compression load cells were deployed to measure overall forces on the model. Four ±89 kN (±20 kip) capacity load cells were mounted between the bent caps and rollers on the linear guide rail to measure vertical forces (see **Figure 3.9**). The remaining two load cells were ±44 kN (±10 kip) capacity load cells that measured horizontal forces acting at mid-height of the bent caps. All six load cells were calibrated in the actual test configuration.

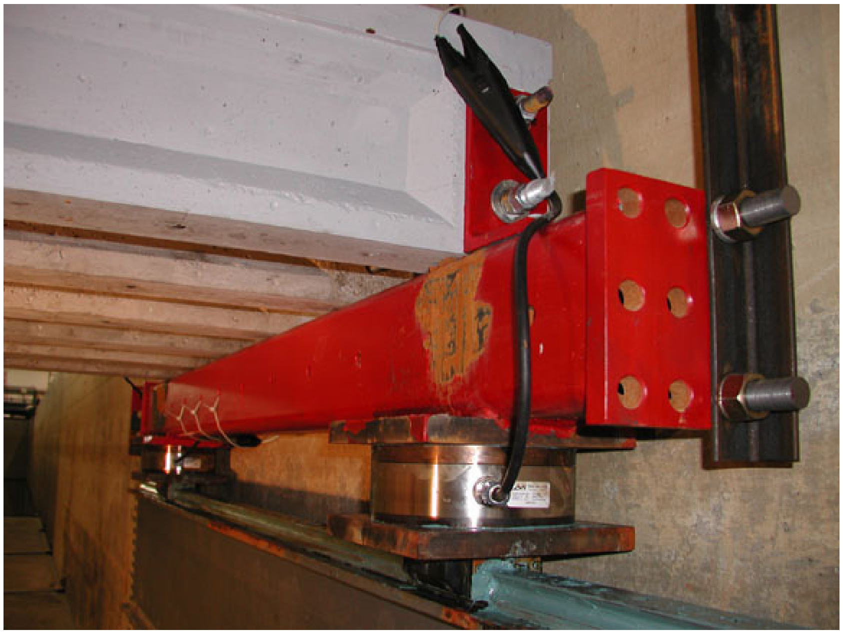

Figure 3.9. Photo of installed vertical load cell, LC5. LC4 can be seen in the background.

3.5.3 Pressure gauges

To measure pressure distribution, 13 pressure transducers were installed in the specimen. Steel mounting plates were cast into the concrete so that the sensors could be securely flush-mounted to the surface of the specimen, minimizing the disruption of flow and sensor response due to vibration. Pressure sensors were mounted in the front face of the deck, the webs of the front and interior girders, and along the underside of the deck between the girders. Locations of pressure gauges and load cells are illustrated in Figure 3.10.

3.5.4 Other instrumentation

Schumacher installed additional instrumentation to measure the specimen's response. The instrumentation is presented for completeness, but the analysis of the data measured by these instruments is beyond the scope of this thesis.

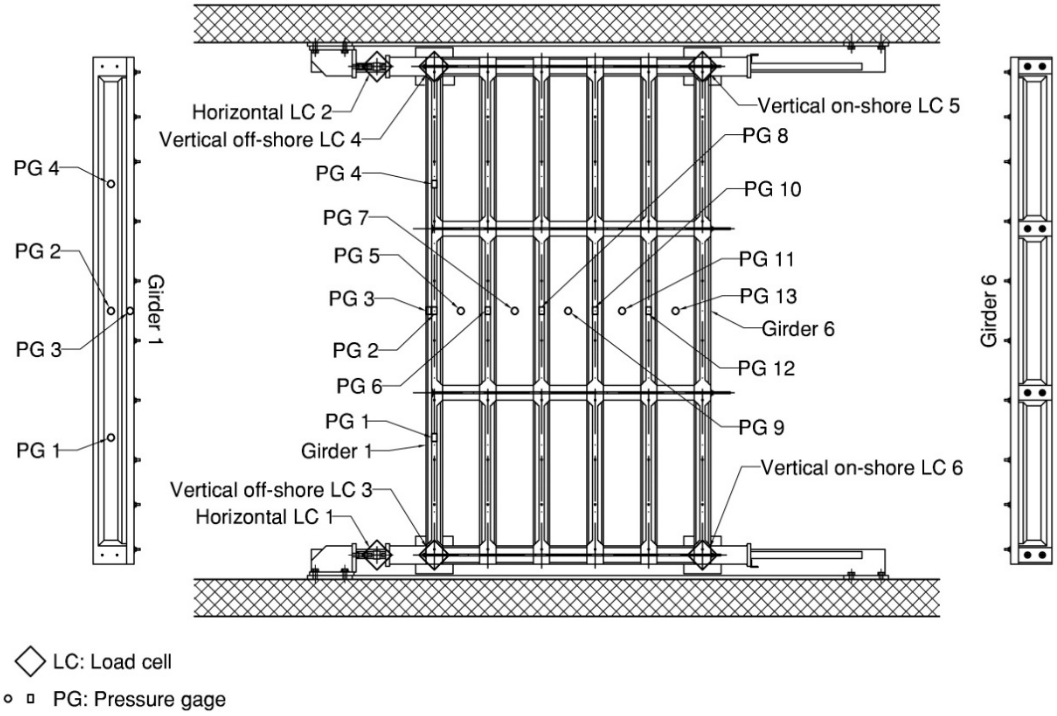

Figure 3.10. Instrumentation plan for pressure gauges and load cells; plan view (deck not shown for clarity). (Courtesy of Thomas Schumacher)

Strain gauges were placed on each girder and measured the flexural response of the specimen. Care was taken in mounting the strain gauges to the concrete since micro as well as macro cracks can allow water to access the back of the gauge. Nevertheless, over the duration of the experiments, some gauges became exposed due to cracks and eventually de-bonded. The critical gauges were replaced to have continuing measurements. To measure the horizontal displacement of the specimen for the dynamic setup, two linear position transducers with a range of 127 millimeters (5 in.) were attached to steel angles at the back of each bent cap. A special enclosure protected these sensors from splash water. For the dynamic setup, six analog accelerometers rigidly mounted to the deck of the test specimen measured accelerations of the test specimen in the horizontal and vertical direction at three different locations. The variable capacitance sensors measure accelerations up to 10 *g* in the range of 0 to 1000 Hz over which the response is practically flat. For calibration purposes, acceleration data were integrated and compared with the derivative of the corresponding displacement data. Excellent correlation was found between the two individually obtained sets of velocity data. Locations of strain gauges, displacement sensors, and accelerometers are illustrated in Figure 3.11.

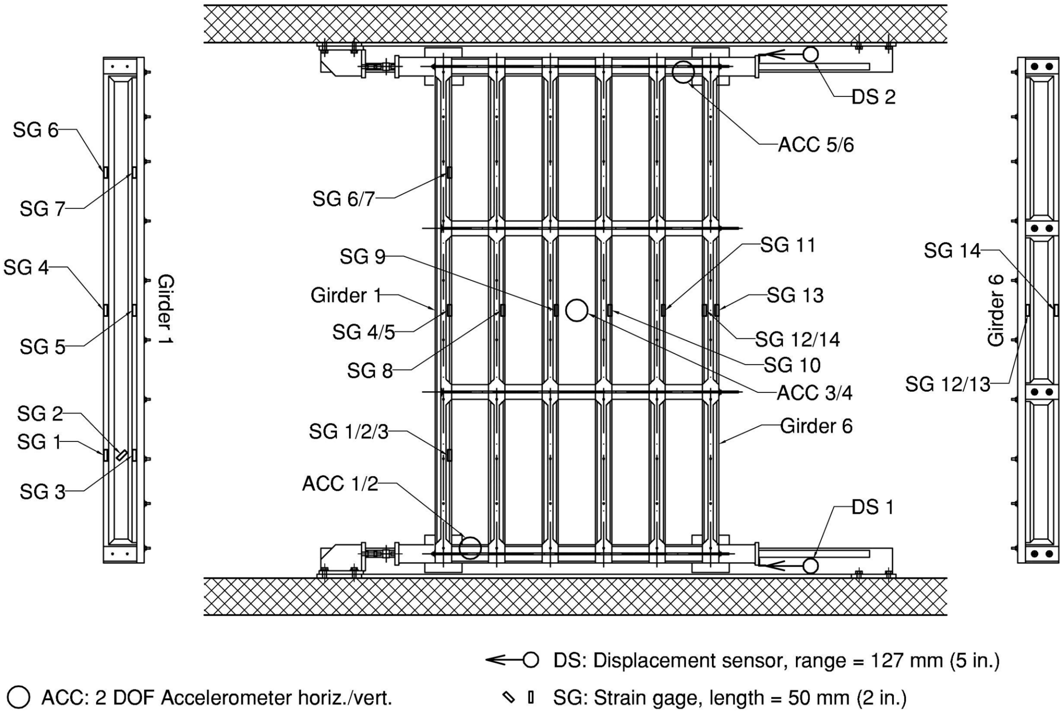

Figure 3.11. Instrumentation plan for strain gauges, displacement sensors and accelerometers; plan view (deck not shown for clarity). (Courtesy of Thomas Schumacher)

Acoustic Emission (AE) sensors were deployed for the dynamic setup. The goal was to evaluate whether the AE technique would be feasible for real-time monitoring of rocking of bridge superstructures. Acoustic Emissions are sometimes called stress waves and are released due to a sudden strain release within a solid body. The AE technique has been established as a means to monitor structural deterioration (e.g., material fracture) and has hence found applications in material science and structural health monitoring. For these experiments, four AE sensors were mounted at each corner of the specimen to the bent caps. A special watertight encasing was constructed to protect the sensors from the waves. AE sensors typically have a piezoelectric element that is in contact with the steel and transforms surface motions into a voltage that can be measured and stored. The sensors used for the present experiments were 150 kHz resonant and are commonly used for steel structures.

4.0 DATA ACQUISITION AND POST-PROCESSING

All data were recorded and stored using a National Instruments 64-channel PXI-based real-time data acquisition system. LabVIEW 8 was used to control the data acquisition process. Data were collected with a minimum sampling rate of 250 Hz. This rate was chosen after finding little variation in the data among test trials that were sampled at rates ranging from 250 to 1000 Hz.

4.1 FILTERING

To prevent aliasing, the data were pre-filtered using an Analog SCXI-1143 Butterworth low-pass filter with a cutoff frequency set to one quarter of the sampling rate. To determine appropriate post-processing filter settings, the natural frequencies of the test specimen and reaction frame were determined through an impact test. The fundamental natural frequencies of the test specimen were found to be 25 Hz in the vertical direction and 135 Hz in the horizontal direction. The natural frequency of the reaction frame in the vertical direction was found to be about 63 Hz. To decrease computation time and to filter out the response of the test frame, all data were further filtered with an 8th order Chebyshev Type I lowpass filter with a cutoff frequency of 50 Hz and then resampled at a rate of 125 Hz.

4.2 CALCULATION OF WAVE HEIGHTS

Incident and reflected wave spectra were determined using a linear least-squared method developed by Mansard and Funke (1980). Data from wave gauges (WG) 5, 7 and 8 were used for this process. The resolved incident and reflected time series corresponds to conditions at WG 5, located approximately 13 meters (42.7 ft.) offshore on the specimen. Transmitted wave heights were directly measured at WG 10, as wave reflection off the beach was calculated and found to be less than 10%. To preserve the integrity of the wave gauge measurements, trials where significant wave breaking was observed onshore of WG 5 were discarded.

For the regular wave trials, the duration of the trials ranged from approximately 60 to 200 seconds and was determined by observations of conditions in the Large Wave Flume (LWF). The goal of the regular wave trials was to determine forces under consistent and repeatable wave conditions. With this goal in mind, trials were conducted until conditions in the LWF became unstable and contrary to the nature of regular waves. Formation of cross-tank waves and the observation of wave-breaking over the horizontal bathymetry were indications of instability. When instability was observed, or when a sufficiently large sample of waves had impacted the test specimen, the trial was stopped. A photo of the tank conditions during a typical regular wave trial can be seen in Figure 4.1. The time series plots from the three wave gauges used to resolve the incident and reflected waves for regular wave trial 1325 can be seen in Figure 4.2 and resolved waves are shown in Figure 4.3. For this trial $H = 0.50$ m, $T = 2.5$ s, and $d^* = 0$.

These conditions closely model the actual conditions at the U.S. 90 Bridge over Biloxi Bay during Hurricane Katrina.

To obtain the most consistent and repeatable results for the regular wave trials, the wave heights and corresponding forces used in the analysis were taken from a window of time between the first wave striking the specimen and the observation of re-reflected waves in the incident wave data. The length of this window varied with wave celerity, and had an average of approximately 27 seconds. The number of waves and corresponding forces within this window ranged between 5 and 16 with an average of 8.3. Figure 4.4 shows the analysis window for Trial 1325. Wave heights for regular wave trials were calculated by taking the mean of the wave heights within this window. The standard deviation of the wave heights within the window was also calculated.

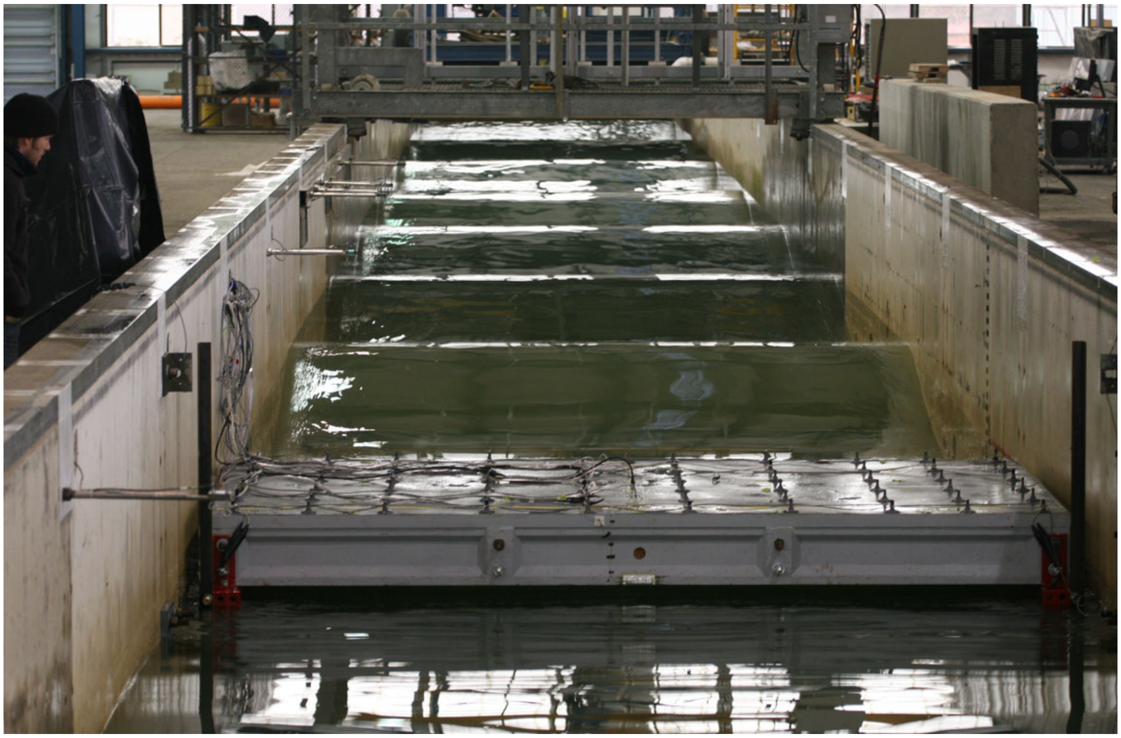

Figure 4.1. Photo of the bridge specimen during regular wave trial at d* = 0.

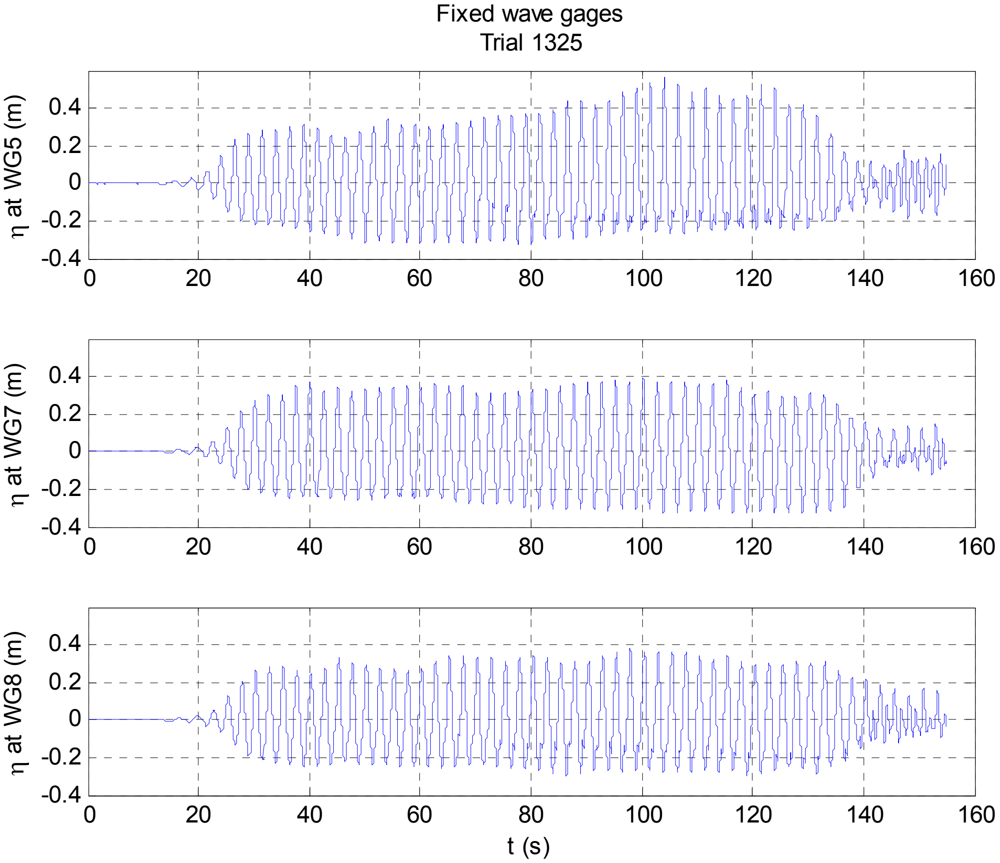

Figure 4.2. Wave gauge time series for WG 5, 7 and 8 used to resolve incident and reflected waves for regular wave trial 1325, H = 0.50 m, T = 2.5 s, d* = 0.

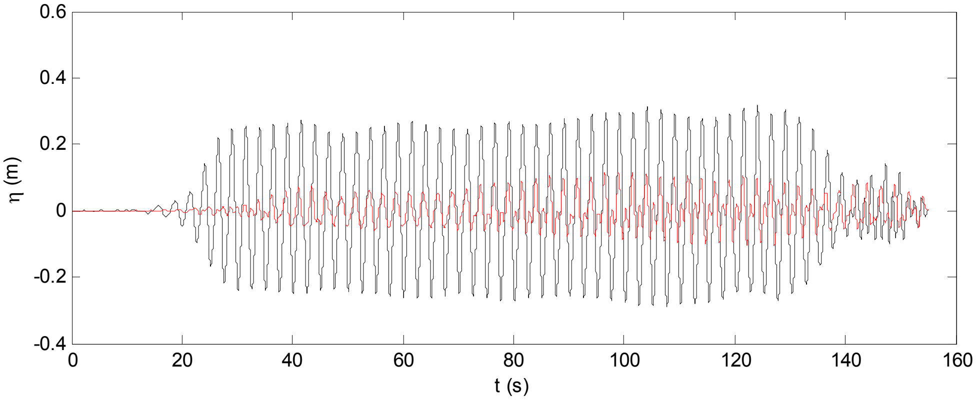

Figure 4.3. Incident and reflected time series for regular wave trial 1325.

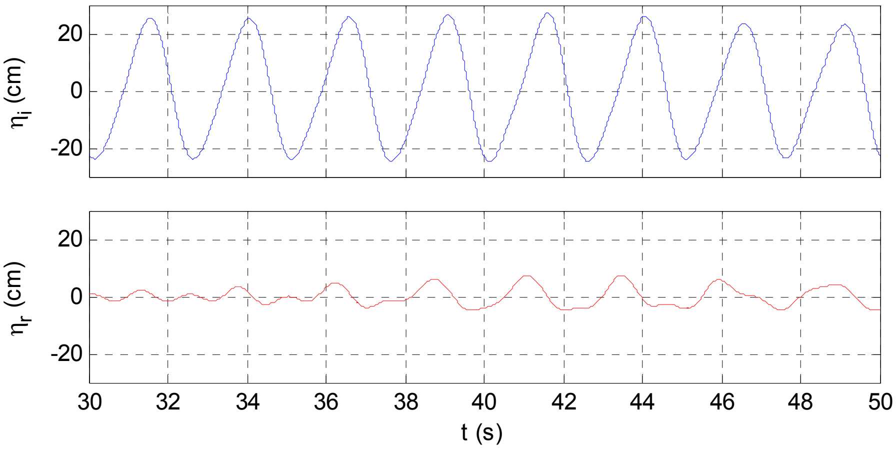

Figure 4.4. Resolved incident and reflected regular waves selected for analysis of regular wave trial 1325.

The duration of the random wave trials varied between 12 and 15 minutes, depending on the peak wave period. The duration of the trials was designed to allow the recording of at least 300 waves per trial. The time series plots from the three wave gauges used to resolve the incident and reflected waves for random wave trial 1315 can be seen in Figure 4.6. For this trial H_s = 0.55 m, T_p = 2.5 s, and d^* = 0. These conditions closely model the actual conditions at the U.S. 90 Bridge over Biloxi Bay during Hurricane Katrina. The frequency spectrum of the resolved waves and corresponding reflection coefficients can be seen in Figure 4.7. The time series of the resolved waves is plotted in Figure 4.8. The analysis window for the random wave trials spanned from the time the first wave struck the bridge until the last generated wave passed WG 10.

Figure 4.5. Photo of the bridge specimen during random wave trial at d* = 0.

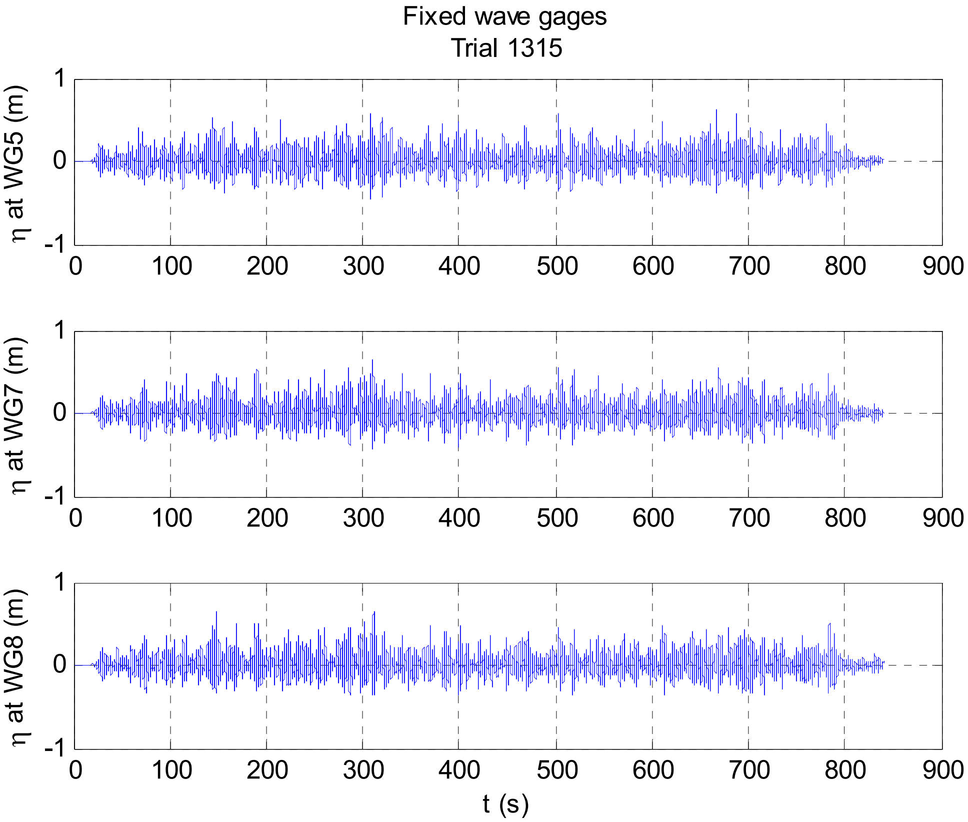

Figure 4.6. Time series of random waves measured at WG 5, 7 and 8, Trial 1315, Hs = 0.55 m, Tp = 2.5 s, d* = 0.

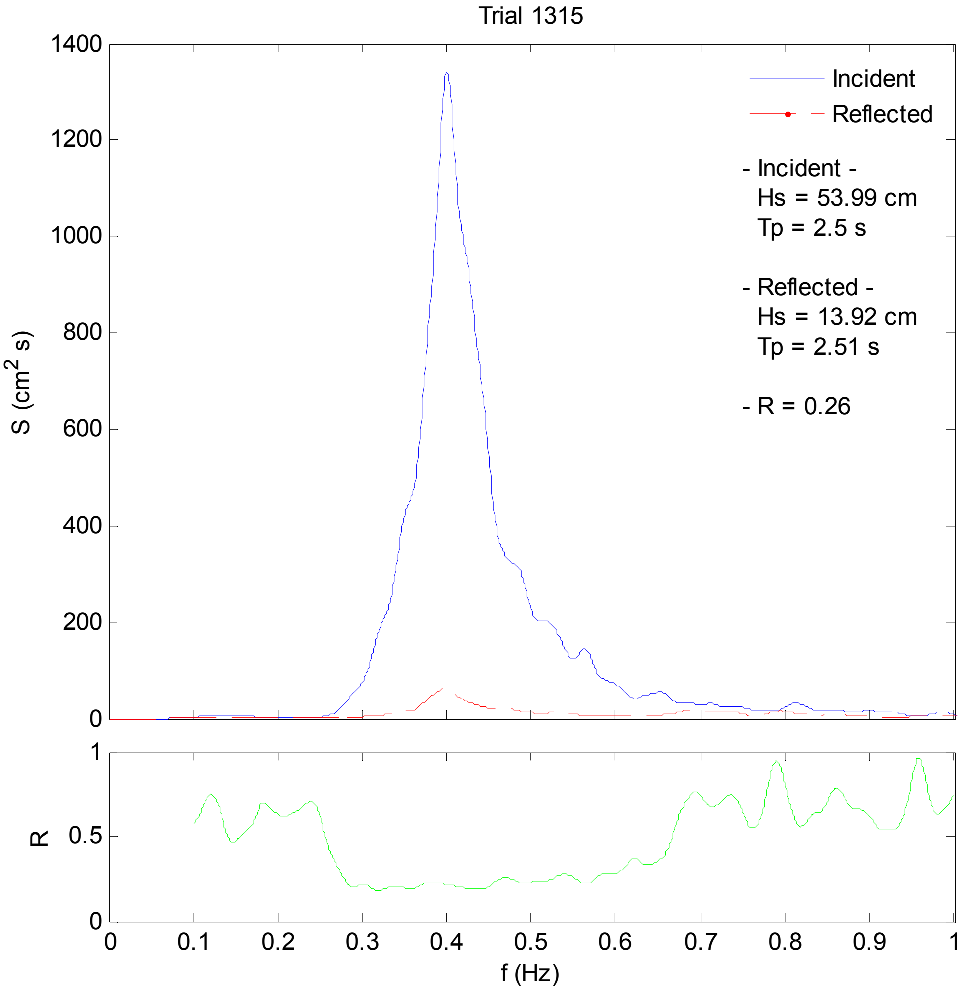

Figure 4.7. Frequency spectrum and corresponding reflection coefficient for random wave trial 1315.

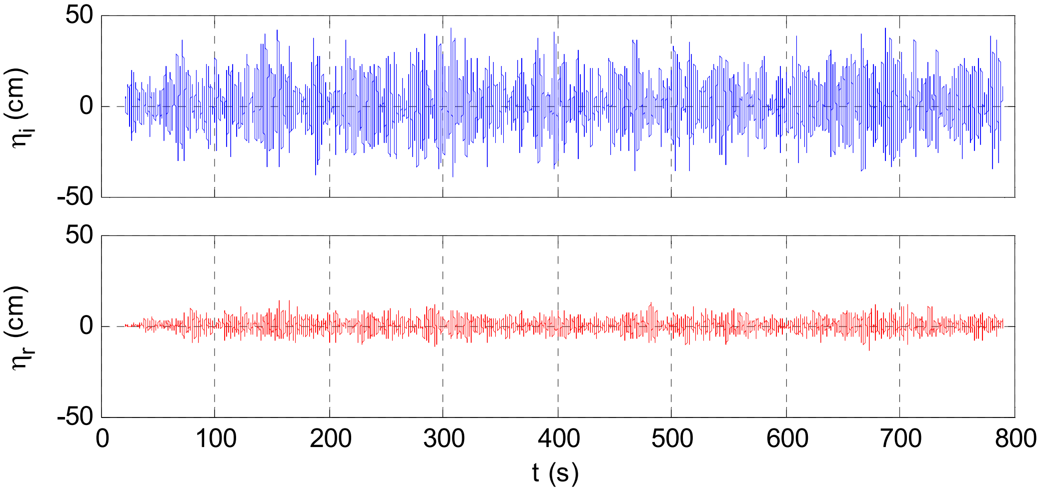

Figure 4.8. Resolved incident and reflected wave time series for random wave trial 1315.

4.3 CALCULATION OF FORCES

The forces were measured using six load cells (LC). The two load cells connecting the bent caps to the end anchorages were designated as LC1 and LC2, and the four load cells mounted beneath the bent caps were designated LC 3-6. See Figure 3.10 for exact locations. Data from LC1 and LC2 were combined to calculate total horizontal force. To calculate the total vertical force, data from all four vertical load cells were added together (LC3 + LC4 + LC5 + LC6). To calculate overturning moment, the vertical loads were separated into offshore loads (LC3 + LC4) and onshore loads (LC5 + LC6). The load cell data was zeroed out at the beginning of each trial and, as a result, buoyancy forces due to a changing of the SWL are eliminated from the load cell measurements.

A modified zero-crossing analysis was used to define individual force events. For regular waves the zero-crossings of the forces were determined by translating the time stamp of the incident wave zero-crossings, using linear wave celerity and the distance from WG 5 to the front face of the specimen. The translation time was refined using the cross-correlation lag between the incident wave gauge data and the load cell data. This refined translation time was also applied to the window defined for the wave height analysis, ensuring that the incident waves measured at WG 5 were the same waves that produced the forces used for the force analysis. The time series of the individual load cell measurements for regular wave trial 1325 is shown in Figure 4.9. Figure 4.10 and Figure 4.11 show the corresponding time series of computed total horizontal and vertical forces, respectively.

For random waves, definition of a force event necessitated a different approach. The force data were smoothed using a zero-phase moving average with an effective cutoff frequency of 12.5 Hz. A zero-crossing analysis of the smoothed data was performed and the resulting zero-crossings were then used to analyze the "unfiltered" force data. Cross-correlation lag between the incident wave and force data was used to determine the analysis window for the random wave trials. Figure 4.12 contains a plot of the individual load cell data for random wave trial 1315. Figure 4.13 shows an expanded view of a portion of the calculated total horizontal and vertical load cells with peak forces, for the same trial.

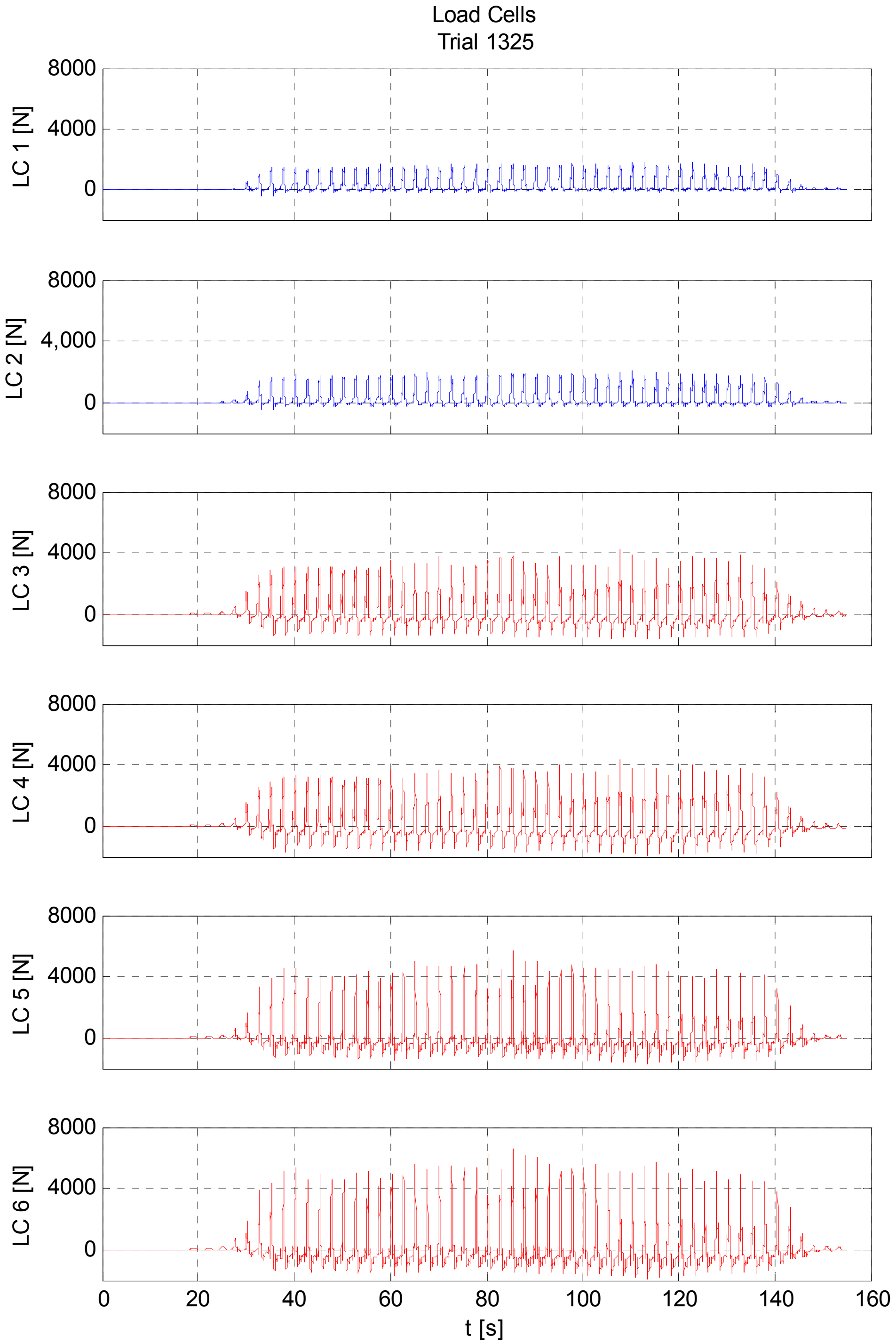

Figure 4.9. Load cell data from regular wave Trial 1325. LC 1 and 2 measure horizontal load, LC 3-6 measure vertical load.

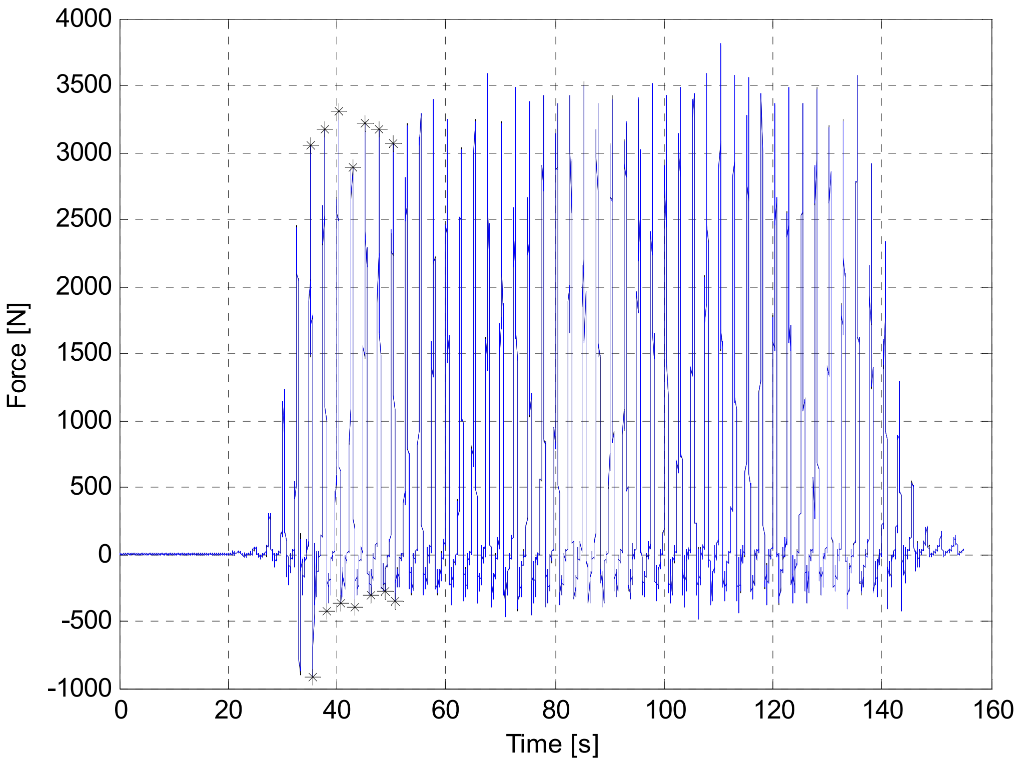

Figure 4.10. Time series of total horizontal force (LC1 + LC2) for regular wave trial 1325. Markers indicate data points used to compute mean positive and negative peak forces.

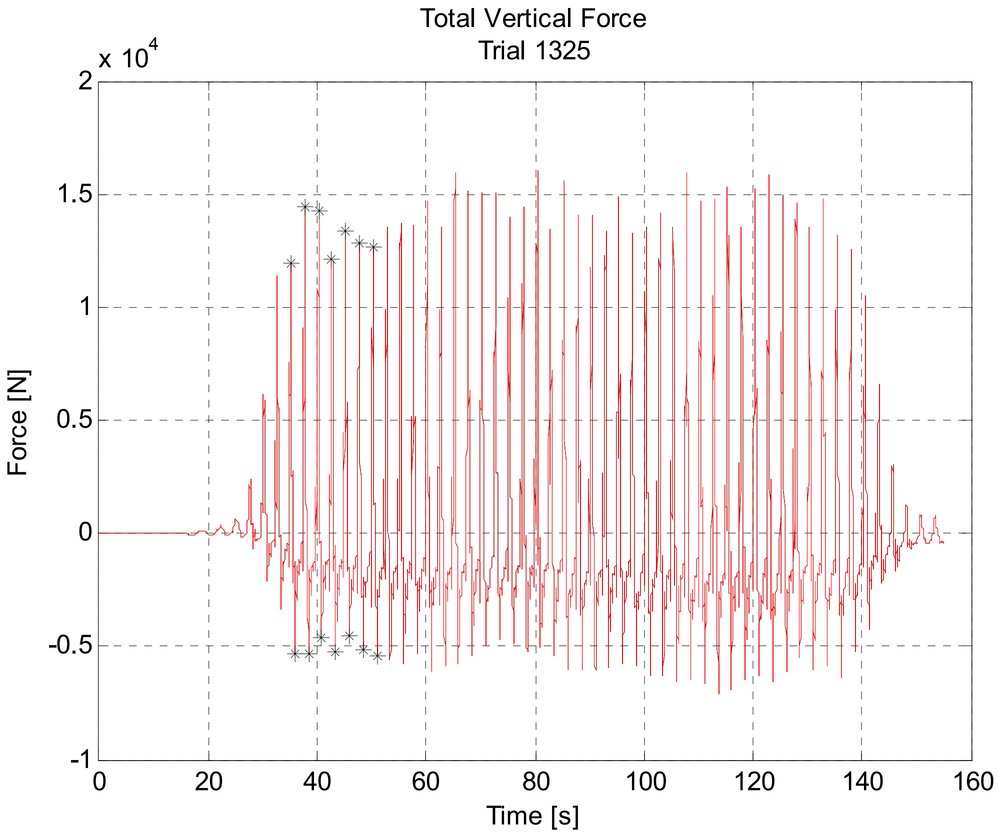

Figure 4.11. Time series of total vertical force (LC3 +LC4 +LC5 +LC6) for regular wave trial 1325. Markers indicate data used to compute mean positive and negative peak forces.

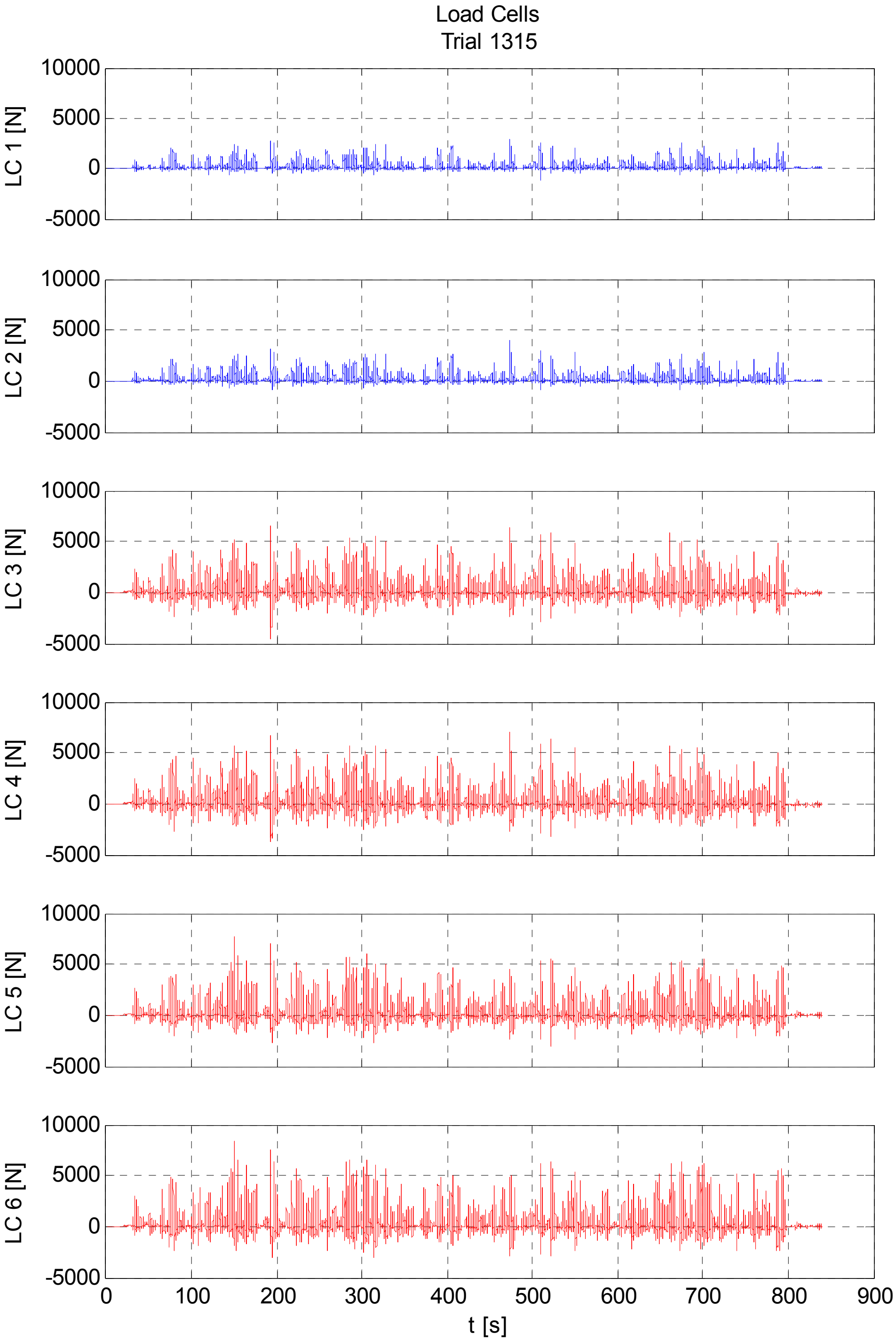

Figure 4.12. Measured load cell time series for random wave trial 1315. LC 1 and 2 measure horizontal forces. LC 3-6 measure vertical forces.

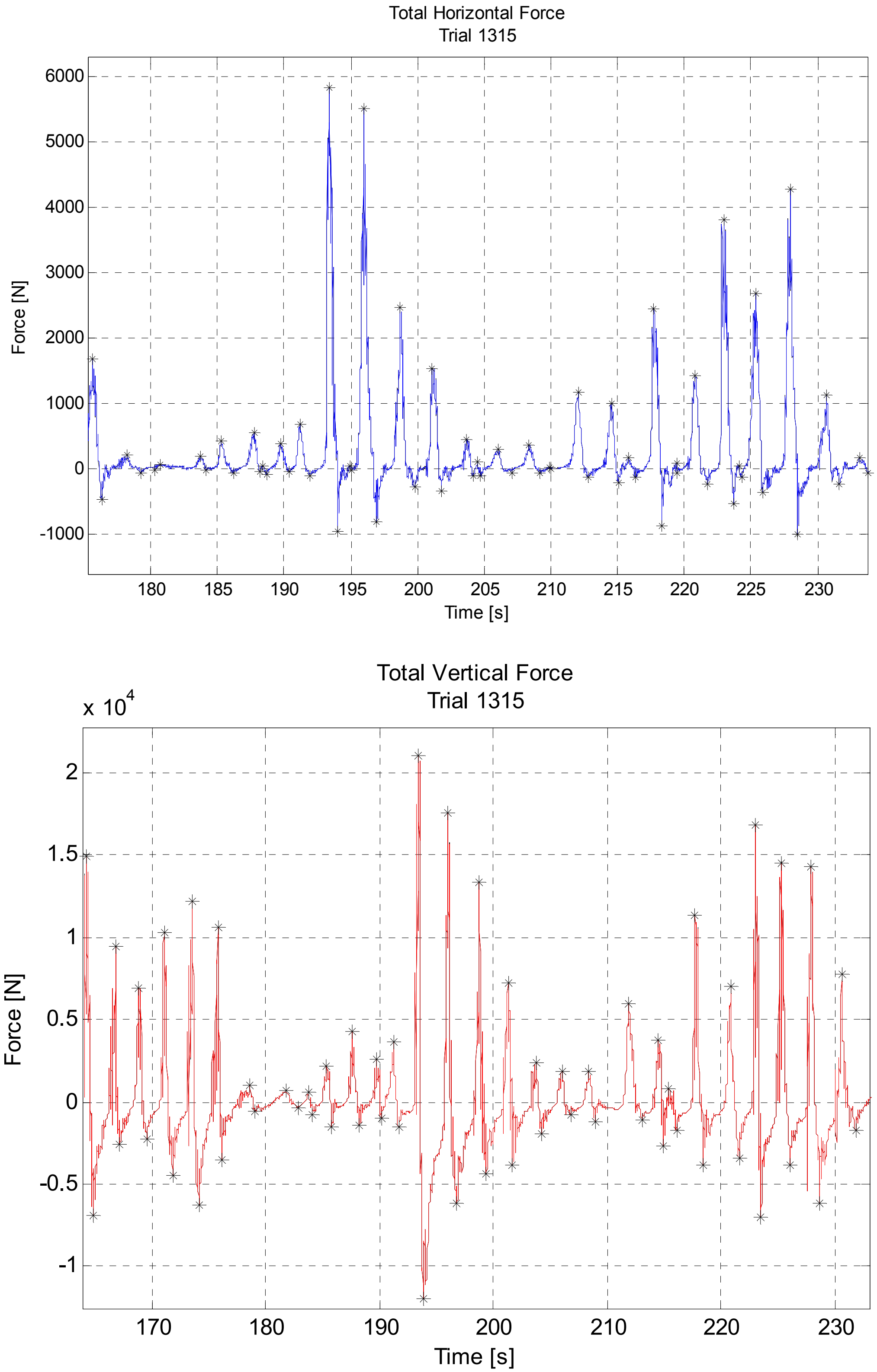

Figure 4.13. Expanded portion of horizontal (top) and vertical (bottom) times series for random wave trial 1315. Markers represent peak forces.

5.0 RESULTS AND OBSERVATIONS

Over the course of six months, between December 2007 and May 2008, over 450 trials were conducted. Of these trials, 428 contained data suitable for analysis. The distribution of these trials among the experimental setups and wave type are contained in Table 5.1. The results of the 214 trials conducted during Phase 1 (rigid setup) are the focus of this thesis and all results presented are from the Phase 1 trials.

Table 5.1. Summary of trials conducted, listed by experimental setup and wave type.

Phase	Horizontal support	Regular Wave Trials	Random Wave Trials
1	Rigid	144	70
2a	Dynamic, medium springs	50	29
2b	Dynamic, soft springs	66	34
3	Unconstrained	28	7
Total		**288**	**140**

5.1 QUALITATIVE ANALYSIS

The force data were analyzed qualitatively to investigate the failure mechanism as well as the significance of the initial impact relative to the quasi-steady pressures induced by the waves. Figure 5.1 shows a comparison of pressure and corresponding vertical load for regular wave trial 1325 ($H = 0.50$ m, $T = 2.5$ s, $d^* = 0$). The pressure data in the figure were taken at Pressure Gauge (PG) 5, which was located along the bottom surface of the bridge deck between two internal girders. The pressure data contains the classic leading impact spike that is approximately five times the magnitude of the following quasi-steady pressure. A review of the corresponding forces in the figure does not reveal a similar pattern. In contrast, the load cell data contains only the quasi-steady force. This was a recurring phenomenon throughout the experiments. While not all of the pressure measurements contained the dramatic impact spike shown in the previous example, the load cell data (horizontal and vertical) consistently exhibited only quasi-steady forces, regardless of the presence of a pressure-impact spike. One set of pressure gauges that did not exhibit the impact spike were those mounted to the front face of the offshore external girder (PG 1-4). Figure 5.2 contains a plot of the pressure readings from PG2, located in the offshore face of the web of the offshore external girder. The pressure events shown in this figure correspond to the pressures and forces shown in Figure 5.1.

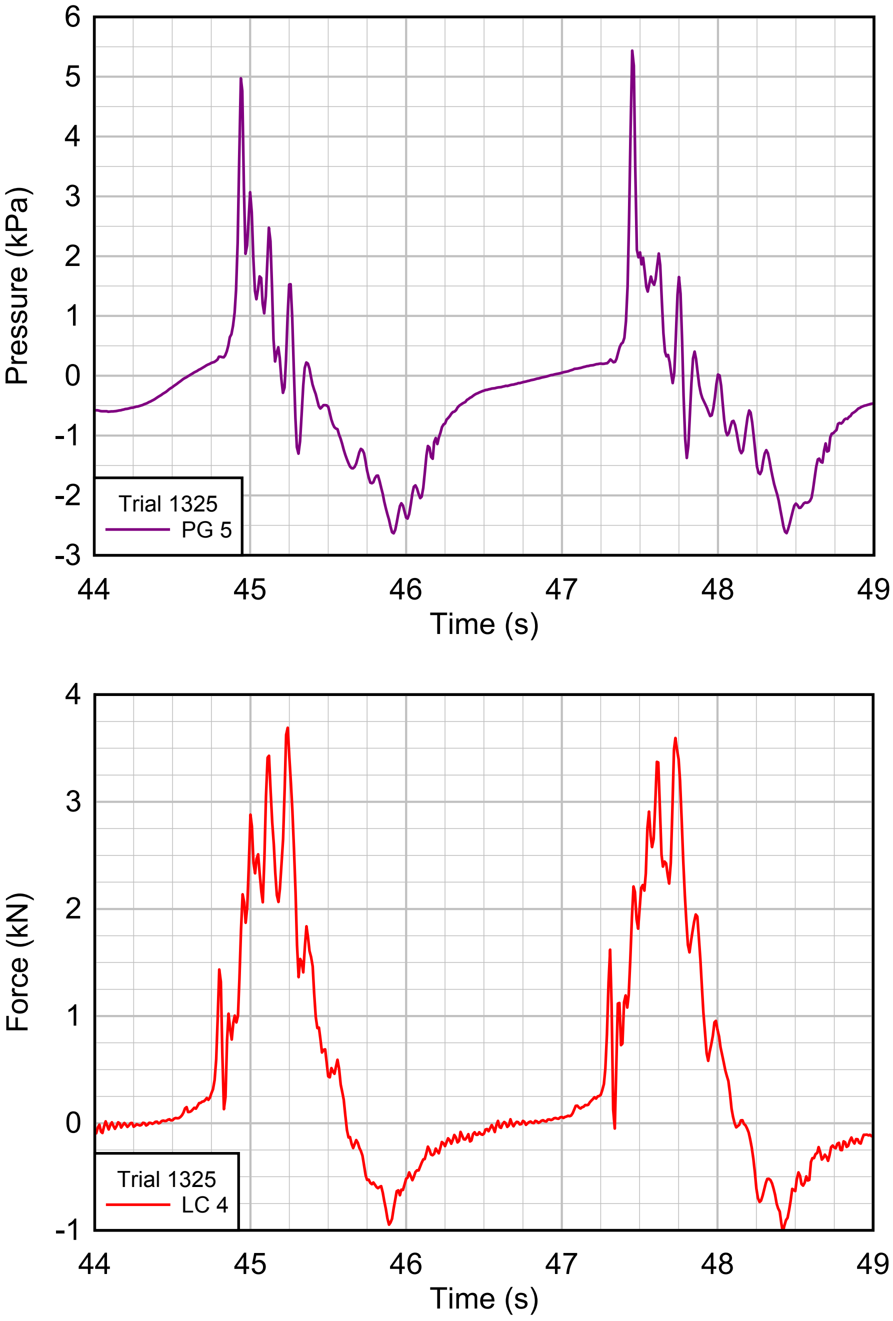

Figure 5.1. Pressure measurement taken beneath the deck and corresponding measurement of the nearest vertical load cell, regular wave trial 1325. See Figure 3.10 for instrument locations.

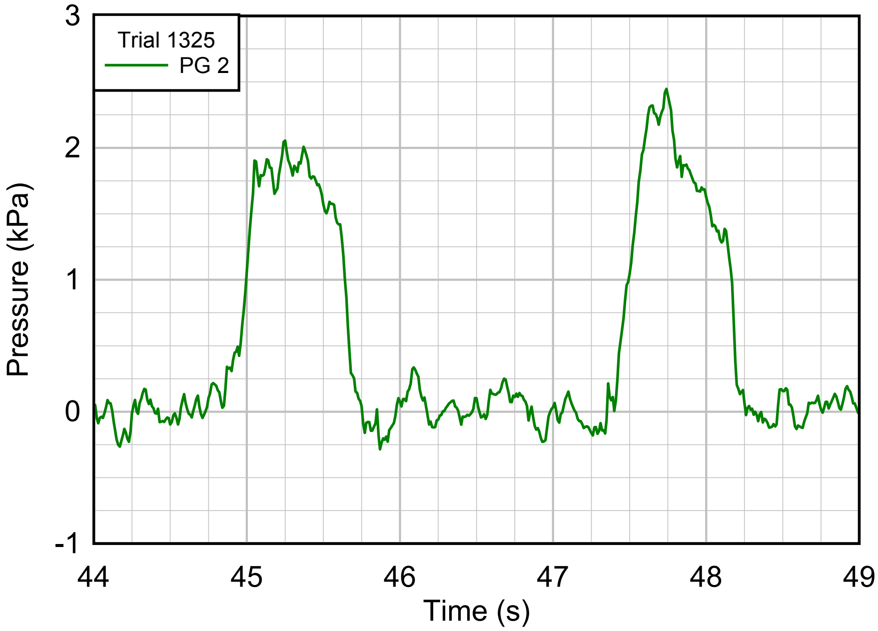

Figure 5.2. Pressure measurement at the center of the offshore face of the web on the offshore external girder, regular wave trial 1325.

Comparing the plots of the total horizontal and vertical forces shown in Figure 5.3, two differences stand out. The first is the magnitude of the peak forces. In this plot, the peak vertical forces are approximately four times as large as the corresponding horizontal forces. This was typical for all of the experiments, as vertical forces were found to be four to six times as large as the horizontal forces. The second is the presence of large spikes within the quasi-steady vertical force data that are not as prevalent in the horizontal data. Analysis of the vertical force data showed these spikes to occur at a frequency of 7-10 Hz, which corresponds to the frequency of passing waves striking the six girders of the bridge superstructure.

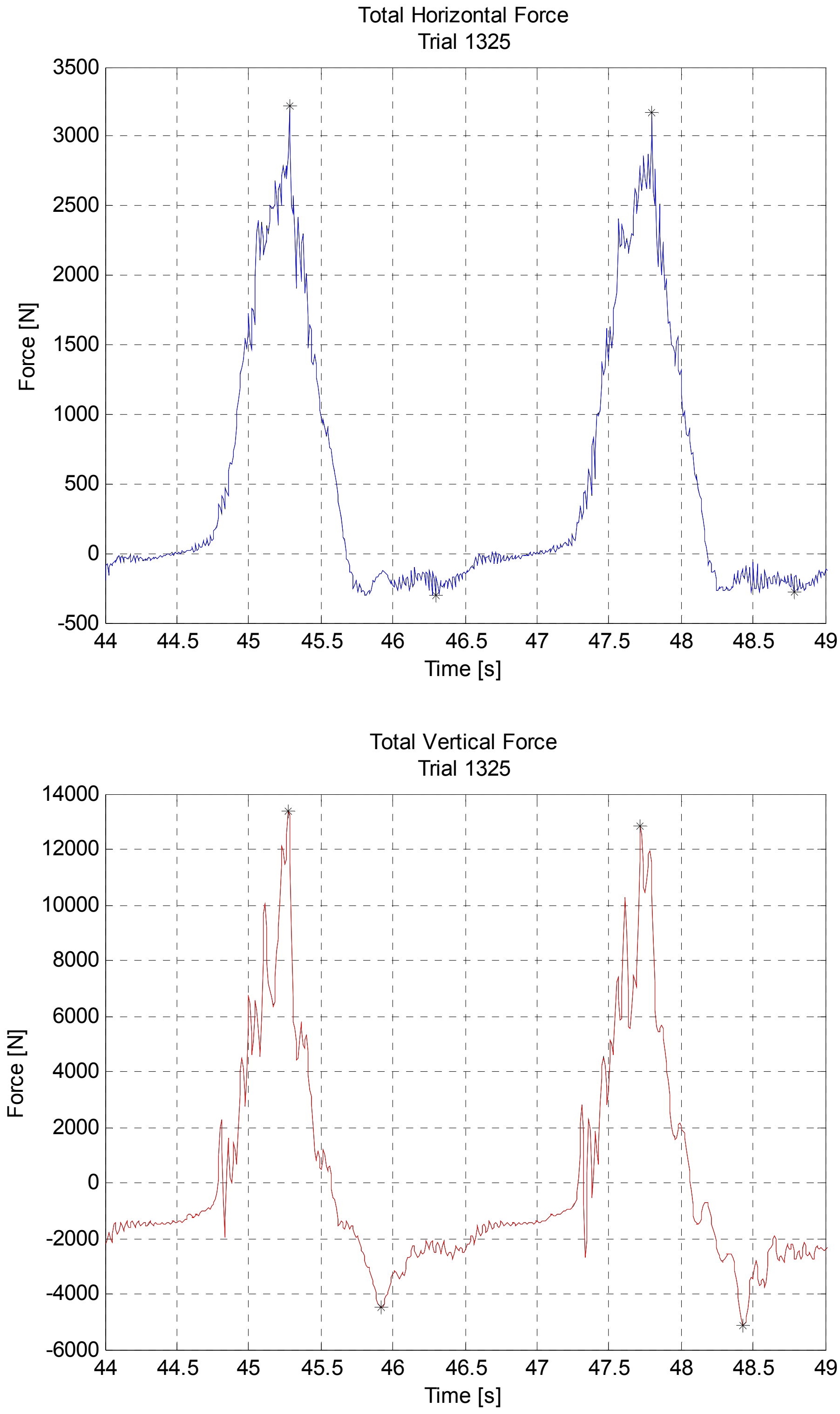

Figure 5.3. Comparison of total horizontal and vertical force events, regular wave trial 1325.

5.2 FORCE VS. WAVE HEIGHT: REGULAR WAVES

For the 144 regular wave trials conducted during Phase 1, mean wave heights and forces, along with their standard deviations, were calculated. These results were then analyzed in an attempt to find a relationship between the forces and commonly available parameters, such as wave height, wave period, water depth and bridge clearance. The analysis revealed that after wave height, the water level had the largest effect on the measured forces. Because the bridge elevation was constant while the water level was changed, water level for these experiments is a combination of water depth and bridge clearance. The forces also appeared to be influenced by wave period to a lesser degree.

As wave height was the primary factor, the forces were organized by water level and wave period and then plotted against wave height to illustrate their relationship. A curve was then fitted through the plotted points using a least-squares method. In an effort to simplify the relationship, the curve was limited to a 1st order (linear) or 2nd order polynomial, depending on the nature of the data. For water levels even with and above the elevation of the bridge, the curve was forces through the origin. For $d^* = -0.5$, the curve was forced through $H = 0.28$ meters, which is twice the bridge clearance at that water level. Similar logic was used to force the curve for trials conducted at $d^* = -1.0$ through $H = 0.56$ meters, but the data did not support this.

In general the data collected at $d^* = -1.0$ was less consistent and deemed less reliable. This is likely due to the relatively shallow water at this depth. This shallow water combined with the large waves needed to reach the bridge at this water level leads to nonlinear waves. The method used to resolve the incident and reflected waves relies on linear wave equations and yields less reliable results when nonlinear conditions are encountered. Data collected at $d^* = 0$ produced the most consistent results. Coincidentally, this level corresponds with critical conditions found at the failed bridges during Hurricanes Katrina and Ivan.

Figure 5.4 through Figure 5.9 show the relationship between wave height and force for the trials conducted at $d^* = 0$. For these plots the horizontal and vertical error bars on each marker represent the standard deviation of the collected wave heights and forces, respectively. The weight of the concrete test specimen is represented by the dotted line. A complete set of plots for all the water levels can be found in Appendix B.

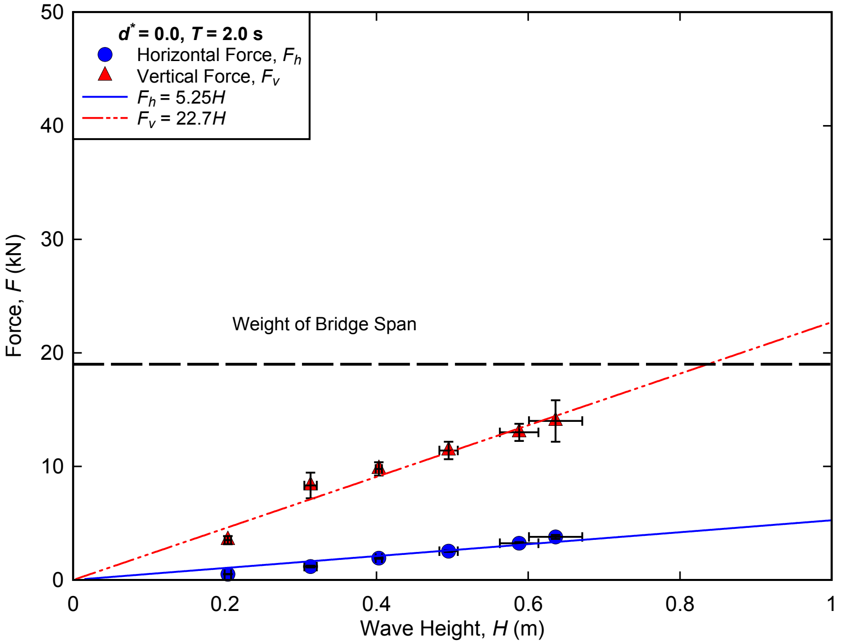

Figure 5.4. Measured forces for regular wave trials conducted at d* = 0.0, T = 2.0 s.

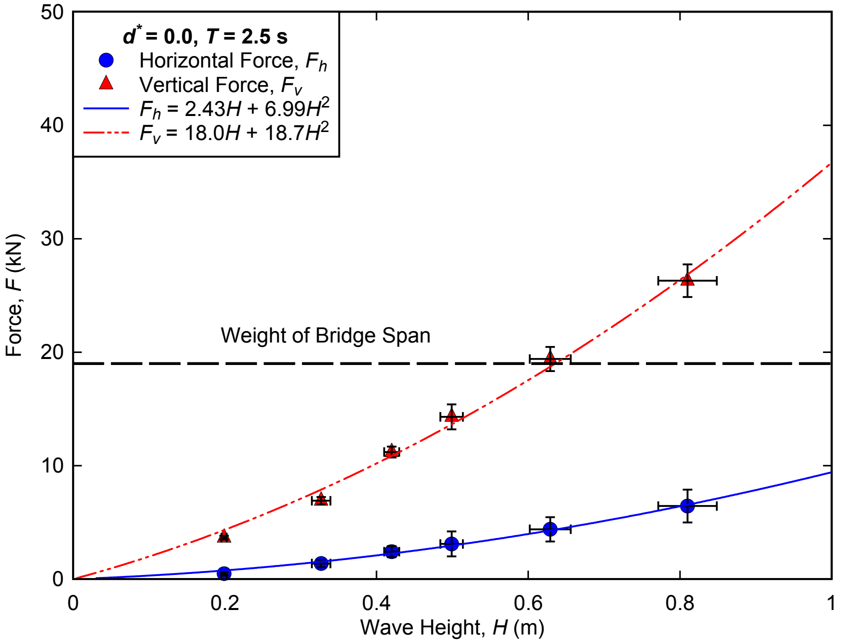

Figure 5.5. Measured forces for regular wave trials conducted at d* = 0.0, T = 2.5 s.

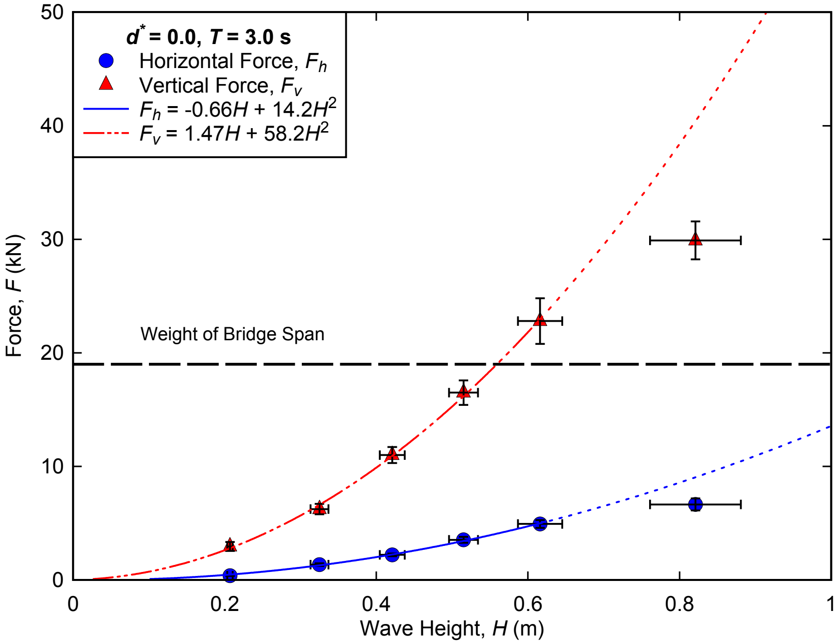

Figure 5.6. Measured forces for regular wave trials conducted at d* = 0.0, T = 3.0 s.

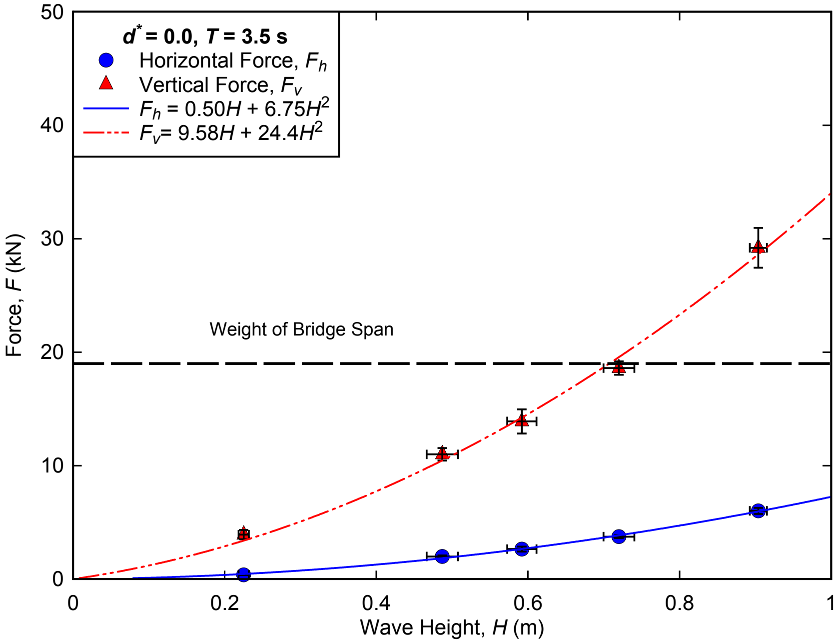

Figure 5.7. Measured forces for regular wave trials conducted at d* = 0.0, T = 3.5 s.

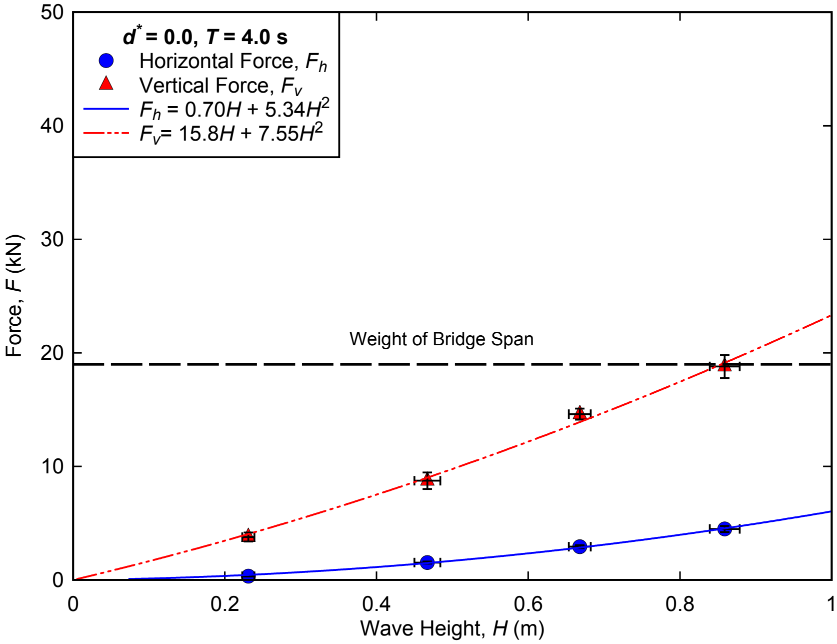

Figure 5.8. Measured forces for regular wave trials conducted at d* = 0.0, T = 4.0 s.

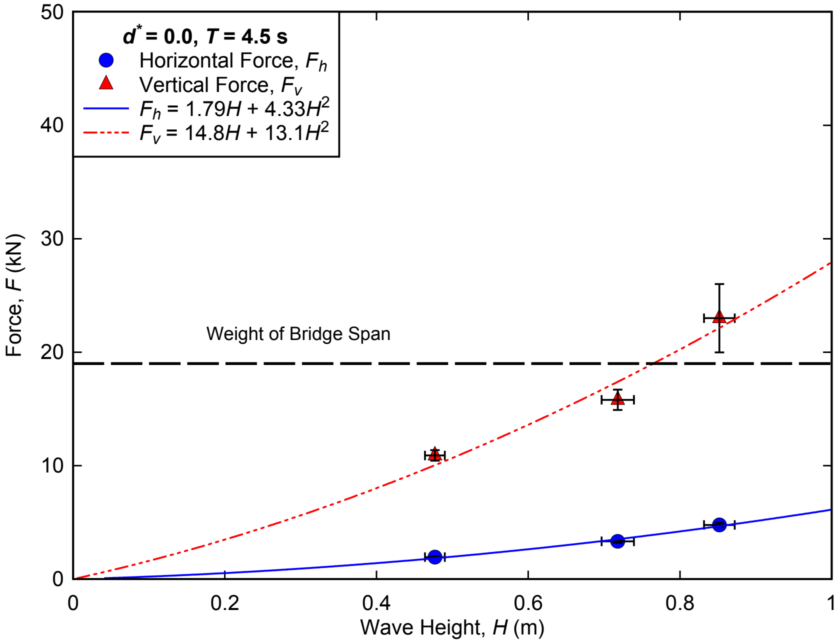

Figure 5.9. Measured forces for regular wave trials conducted at d* = 0.0, T = 4.5 s.

5.3 FORCE VS. WATER LEVEL: REGULAR WAVES

The effect of water level on the forces was analyzed by calculating the force generated by a common wave height for each water level and wave period tested. Because the wave heights varied for each trial, this force was calculated using the fitted curves and a wave height of 0.6 meters. Figure 5.10 shows the relationship between forces and water level for *T = 2.5 s*. For this wave period, the greatest forces are recorded at *d** = 0. For the remainder of the wave periods tested, water levels of *d** = 0 or +0.5 provided the largest forces. As might be expected, the lower water levels of *d** = -1.0 and -0.5 produced the lowest forces. One finding from the analysis was that forces tended to level off or even decrease as the bridge became submerged at the higher water levels. A complete set of plots can be found in Appendix C.

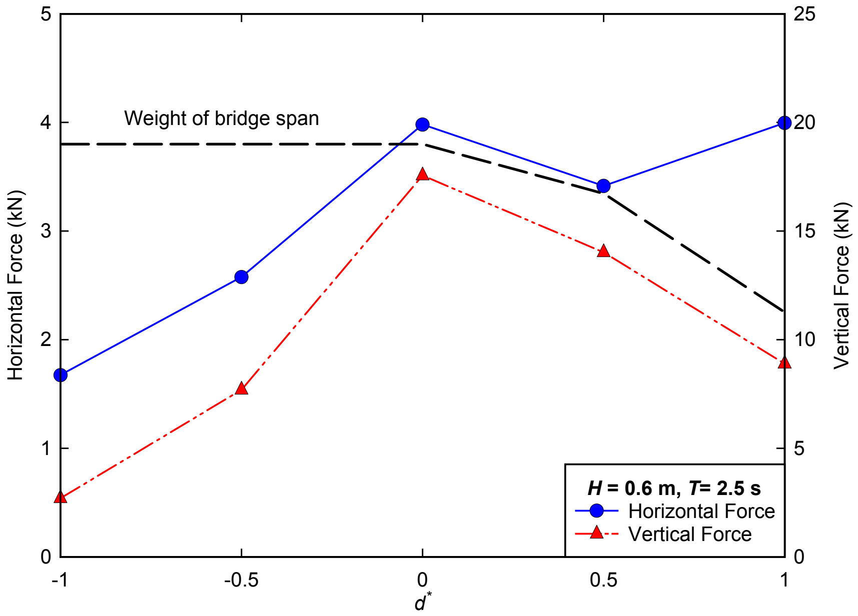

Figure 5.10. Calculated force vs. water level for T = 2.5 s. The weight of the bridge span (accounting for buoyancy) is represented by the dashed line and should be read using the vertical force scale.

The above analysis provides insight to the effect of water level on forces, but it does not tell the complete story. The forces presented represent the hydrodynamic force of the waves. The bridges also experience a hydrostatic force when the Mean Water Level (MWL) exceeds the low chord of the bridge girders. To measure the actual force exerted on the bent cap connections that were critical in the failure of the prototype bridges, the hydrodynamic force combined with the buoyancy force must first overcome the weight of the bridge. A more practical method of analyzing the effect of water level on forces may be to determine the critical water level. This critical water level may be defined as the level which requires the smallest wave to overcome the weight of the bridge when buoyancy is taken into account. For this analysis, the equations for the vertical force fitted curves were used to compute the wave heights that would produce a force equal to the net weight of the tested bridge specimen. In some cases this wave height was computed using extrapolated data. This indicates that these wave heights are unrealistic or even physically impossible due to depth-limited breaking. Figure 5.11 shows the analysis for *T* = 2.5 s. At this period, *d** = 0 is the critical depth, but the wave height required at *d** = +0.5 is virtually identical. One could argue that due to the increased water level, it is more likely that a larger wave could strike a bridge under realistic conditions. For each of the wave periods tested, either *d** = 0 or *d** = +0.5 proved to be the depth that gave the maximum horizontal and vertical force. A complete set of plots can be found in Appendix D.

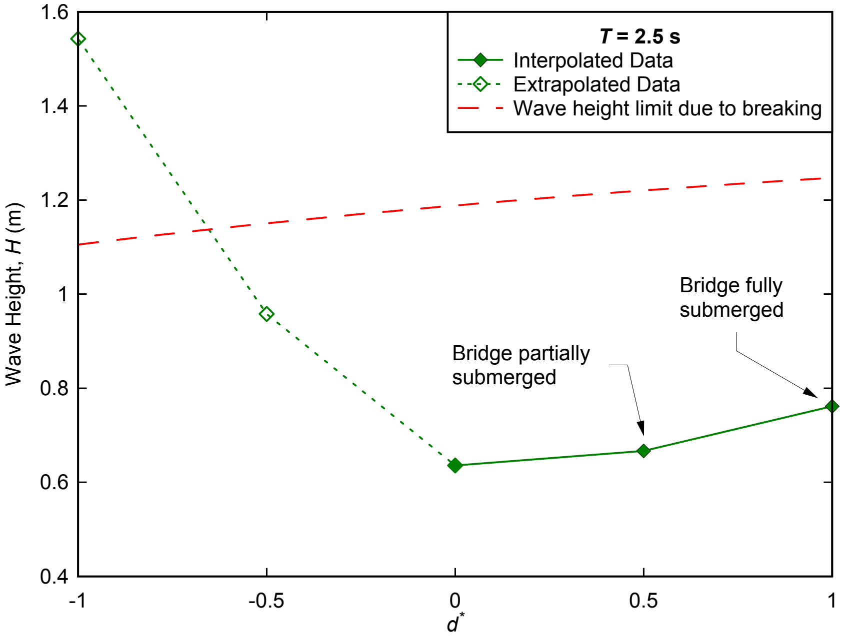

Figure 5.11. Minimum wave height to overcome weight of superstructure, T = 2.5s.

5.4 FORCE VS. WAVE PERIOD: REGULAR WAVES

The effect of wave period on the forces was analyzed by calculating the force generated by a common wave height for each wave period and water level tested. Because the wave heights varied for each trial, this force was calculated using the fitted curves. A wave height of 0.6 meters was chosen for the analysis. Figure 5.12 shows the relationship between forces and wave period for *d** = 0. At this water level, the period appears to affect the horizontal and vertical forces similarly. Both the maximum horizontal and vertical forces were found at *T* = 3.0 s and both show a decrease in magnitude at the longer periods. Although not directly related to regular wave periods, the estimated peak period (scaled) at the U.S. 90 Bridge over Biloxi Bay during Hurricane Katrina is given as a reference to conditions during extreme events found in the shallow estuaries and bays where coastal bridges are typically located. The critical wave period varied depending on the water level, and horizontal and vertical forces at a given water level were often affected differently by a change in the period. A complete set of plots can be found in Appendix E.

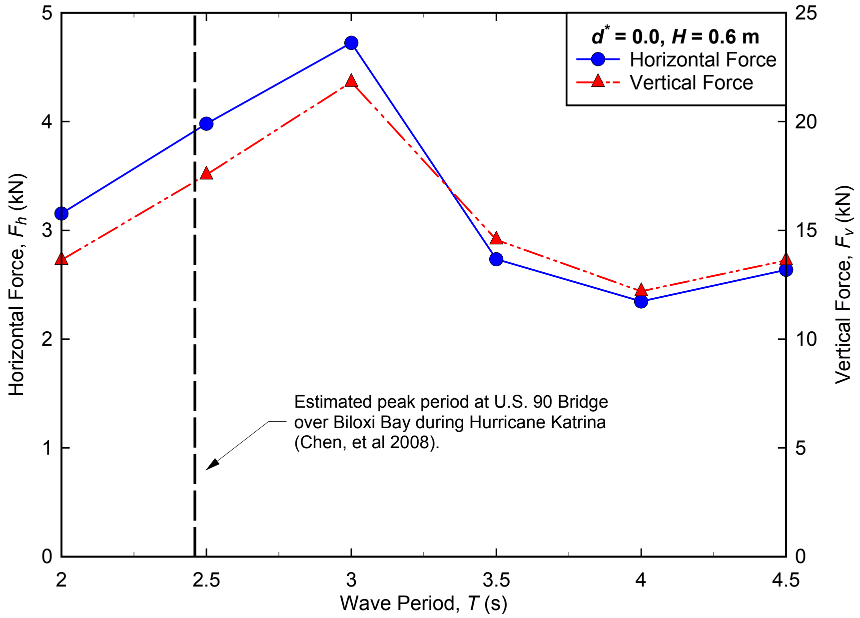

Figure 5.12. Effect of wave period on forces for regular waves, d* = 0.0.

5.5 FORCE VS. WAVE HEIGHT: RANDOM WAVES

Similar to the analysis conducted on the regular wave trials, the relationship between forces and wave heights was examined for the random wave trials. For these trials, significant wave height, H_s, was compared to the average of the highest one-third of the measured forces, $F_{1/3}$. For trials conducted at $d^* = -1.0$ and -0.5, the sample used to calculate $F_{1/3}$ may be significantly smaller compared to the others, as only the highest waves for trials at these depths struck the bridge superstructure. Unlike the regular wave trials, wave period did not have a profound effect on the relationship between wave height and force. Except for the wave height, only water level appeared to be a factor. This may be an attribute of the smoothing inherent in random wave data and statistically derived parameters. A curve was fitted to the horizontal and vertical data, except for trials at $d^* = -1.0$, where the range of the data was not sufficient to provide a reliable curve. For $d^* = -0.5$, the curve was forced through 0.17, 0 (H_s, $F_{1/3}$) as $H_s = 0.17$ meters was calculated as the minimum condition that would produce a wave large enough to strike the bridge superstructure, assuming a Rayleigh distribution of wave heights and a sample size of 300 waves. For all other water levels, the curve was forced through the origin. This wave height-force relationship for $d^* = 0$ is presented in Figure 5.13.

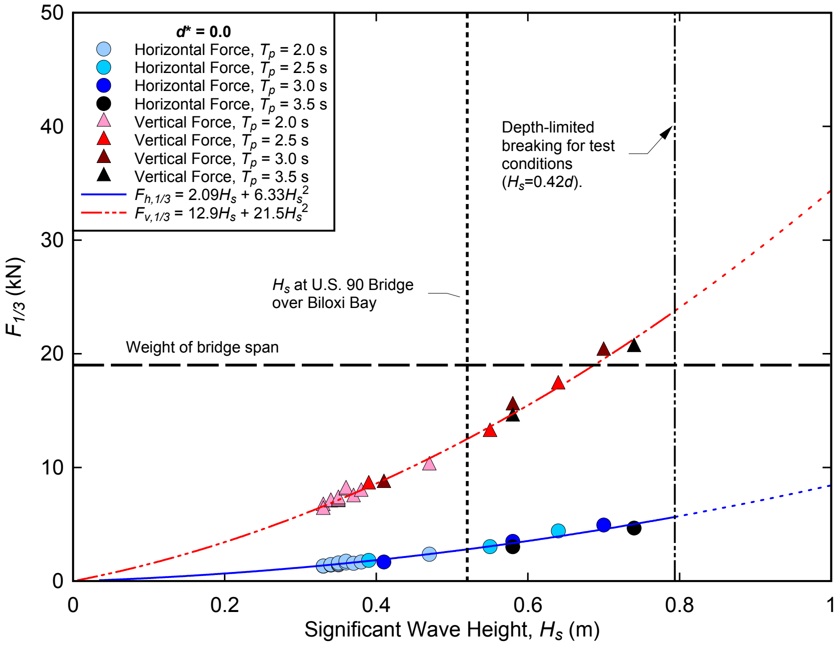

Figure 5.13. Force vs. wave height for random wave trials, d* = 0.0. Hs (scaled) for the U.S. 90 Bridge over Biloxi Bay during Hurricane Katrina, as estimated by Chen et al., (in press) is plotted along with the weight of the bridge superstructure used in the experiment (accounting for buoyancy).

With the exception of the independence to wave period, the relationship between wave and forces for the random wave trials was very similar in nature to that of the regular wave trials. In general, both appeared to follow 2nd order polynomial relationships and in both cases vertical forces were much larger than horizontal forces. A complete set of plots can be found in Appendix F. Due to the limitations of the linear method used to resolve wave height as well as the small sample size of forces collected, force data for the random wave trials conducted at *d** = -1.0 are not considered reliable and are presented for completeness.

6.0 MODELING OF FORCE USING WAVE MOMENTUM FLUX

6.1 MOMENTUM FLUX PARAMETER

The previous chapters have shown that when grouped by water level and wave period, forces can be accurately estimated using simple empirical equations. This method is not practical, however, as the experiment generated 60 different equations to calculate horizontal and vertical forces for the range of conditions tested. A more practical approach is to develop an analytical model based on fluid mechanics and wave theory. Hughes (2004) introduced the wave momentum flux parameter as a tool to "characterize flow kinematics in nonbreaking waves at a given depth." The idea behind this parameter was that it could provide a link between empirical data and physical processes in the nearshore environment.

The relevance of wave momentum flux to wave forces on coastal structures was noted by Longuet-Higgins and Steward (1964):

> *Surface waves possess momentum which is directed parallel to the direction of propagation and is proportional to the square of the wave amplitude. Now if a wave train is reflected from an obstacle, its momentum must be reversed. Conservation of momentum then requires that there be a force exerted on the obstacle, equal to the rate of change of wave momentum. This force is a manifestation of the radiation stress.*

The instantaneous flux of horizontal momentum, m_f, across a unit area of a vertical plane oriented parallel to the wave crest is given by

$$m_f(x, z, t) = p_d + \rho u^2 \tag{6-1}$$

where p_d is the hydrodynamic pressure and u is the horizontal particle velocity. This instantaneous momentum flux can be integrated over the depth of the water column resulting in the expression

$$M_F(x, t) = \int_{-h}^{\eta(x)} (p_d + \rho u^2)\, dz \tag{6-2}$$

where η is the water surface elevation and h is the water depth. This depth-integrated momentum flux has units of force per unit width and reaches a maximum value when $\eta(x)$ equals the wave amplitude, a. Substituting the linear wave equations for pressure and velocity, and then integrating from $z = -h$ to $z = a$, the maximum depth-integrated horizontal wave momentum flux for extended linear theory can expressed as

$$(M_F)_{max} = \frac{\rho g a}{k}\,\frac{\sinh[k(h+a)]}{\cosh kh} + \frac{\rho g a^2}{2} \times \left[\frac{\sinh\,[2k(h+a)] + 2k(h+a)}{\sinh 2kh}\right] \tag{6-3}$$

where k = wave number = $2\pi/L$.

Hughes introduces a nondimensional parameter called the "wave momentum flux parameter," obtained by dividing the depth-integrated momentum flux by ($\rho g h^2$). The extended linear theory version of this parameter is given as

$$\left(\frac{M_F}{\rho g h^2}\right)_{max} = \frac{1}{2}\left(\frac{H}{h}\right)\frac{\sinh[k(h+H/2)]}{kh\cosh(kh)} + \frac{1}{8}\left(\frac{H}{h}\right)^2 \times \left[\frac{\sinh[2k(h+H/2)] + 2k(h+H/2)}{\sinh 2kh}\right] \tag{6-4}$$

where H = wave height = 2a for linear waves.

Hughes also developed an empirical approximation of the wave momentum flux parameter of finite amplitude waves based on a Fourier wave numerical model. This approximation was shown to better estimate the wave momentum flux for nonlinear conditions when compared to the linear and extended linear equations. Referred to as the "nonlinear wave momentum flux parameter," the empirical approximation is given as

$$\left(\frac{M_F}{\rho g h^2}\right)_{max} = A_0\left(\frac{h}{gT^2}\right)^{-A_1} \tag{6-5}$$

where

$$A_0 = 0.6392\left(\frac{H}{h}\right)^{2.0286} \tag{6-6}$$

$$A_1 = 0.1804\left(\frac{H}{h}\right)^{-0.391} \tag{6-7}$$

To determine if the measured wave forces on the test specimen could be related to wave momentum flux, a wave momentum flux parameter was calculated for each regular and random wave trial.

For the regular wave trials, both a linear and nonlinear wave momentum flux parameter was calculated, using the mean wave height, water depth, and calculated linear wavelength for each trial. Figure 6.1 and Figure 6.2 show horizontal force plotted versus linear and nonlinear momentum flux, respectively. Figure 6.3 and Figure 6.4 show vertical force plotted versus linear and nonlinear momentum flux, respectively. In all four plots, a general relationship can be seen, as force and momentum flux appear to be directly proportional. When each water level is examined individually, this relationship becomes clearer and could be quantified with an empirical coefficient, if desired. Data from the trials conducted at $d^* = -1.0$ contains the most scatter. This is likely a function of the previously mentioned limitations in the calculation of incident wave height for nonlinear conditions. There is not a discernable difference between the linear and nonlinear plots.

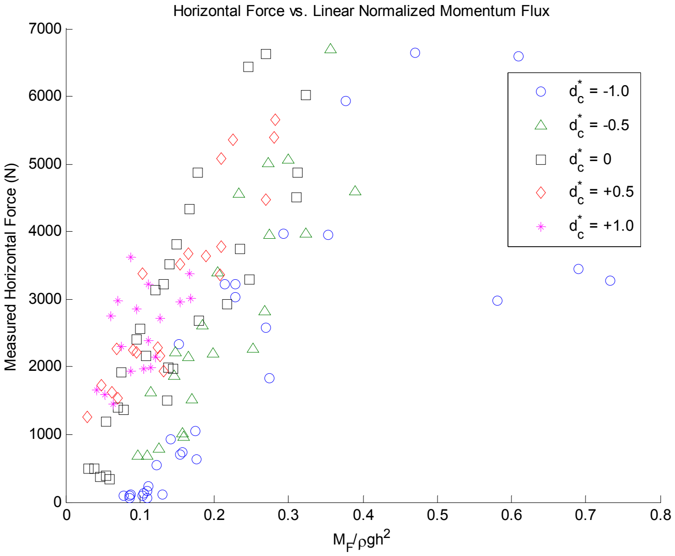

Figure 6.1. Measured horizontal force vs. linear wave momentum flux parameter for regular wave trials.

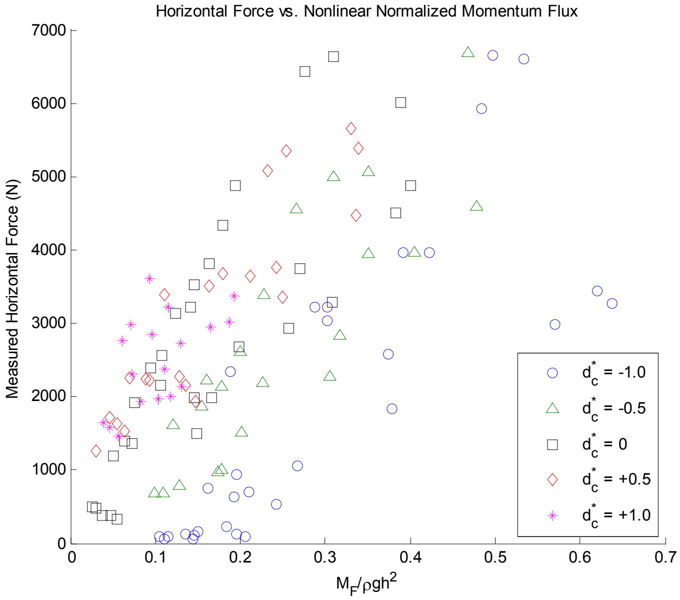

Figure 6.2. Measured horizontal force vs. nonlinear wave momentum flux parameter for regular wave trials.

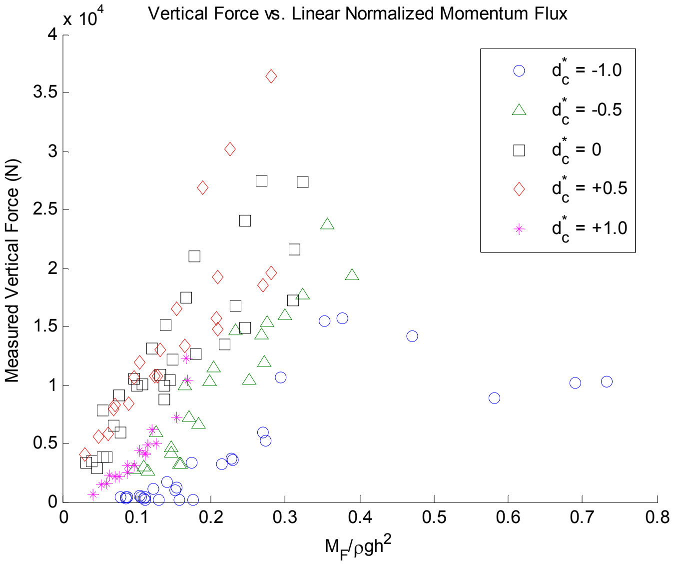

Figure 6.3. Measured vertical force vs. linear wave momentum flux parameter for regular wave trials.

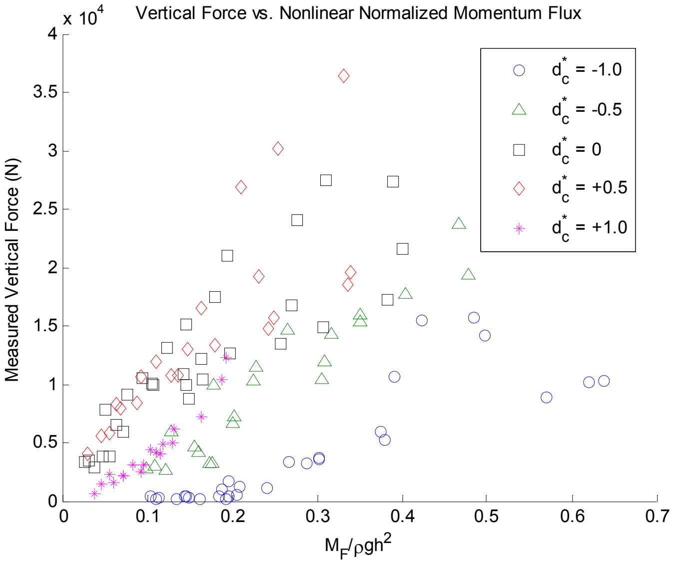

Figure 6.4. Measured vertical force vs. nonlinear wave momentum flux parameter for regular wave trials.

For the random wave trials, the nonlinear wave momentum flux parameter was calculated using significant wave height, H_s, for the wave height. The momentum flux was then compared with the average of the highest one-third of the forces, $F_{1/3}$. Figure 6.5 shows the comparison of horizontal forces and Figure 6.6 shows the vertical force relationship. Similar to the regular wave trials, the relationship for both the horizontal and vertical random wave forces appears to be directly proportional to wave momentum flux. When compared to the horizontal force relationship, the relationship between vertical force and momentum flux has significantly less scatter.

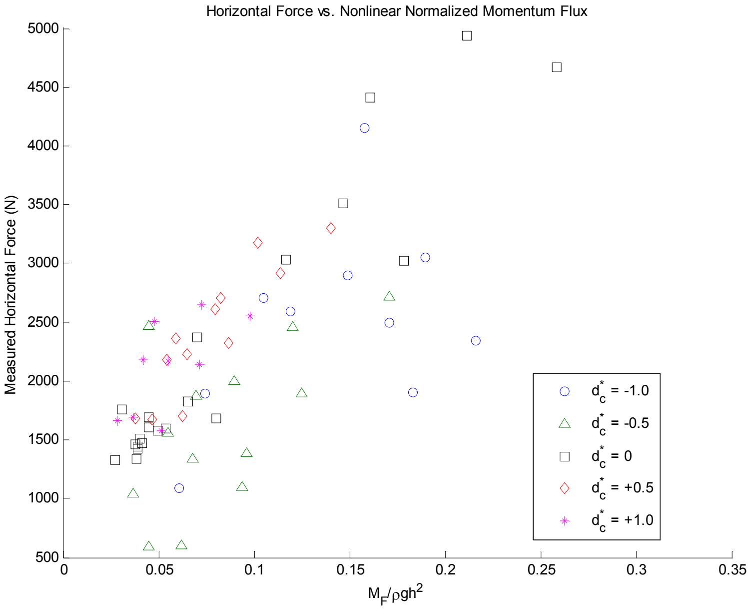

Figure 6.5. Measured Fh,1/3 vs. nonlinear wave momentum flux parameter for random wave trials.

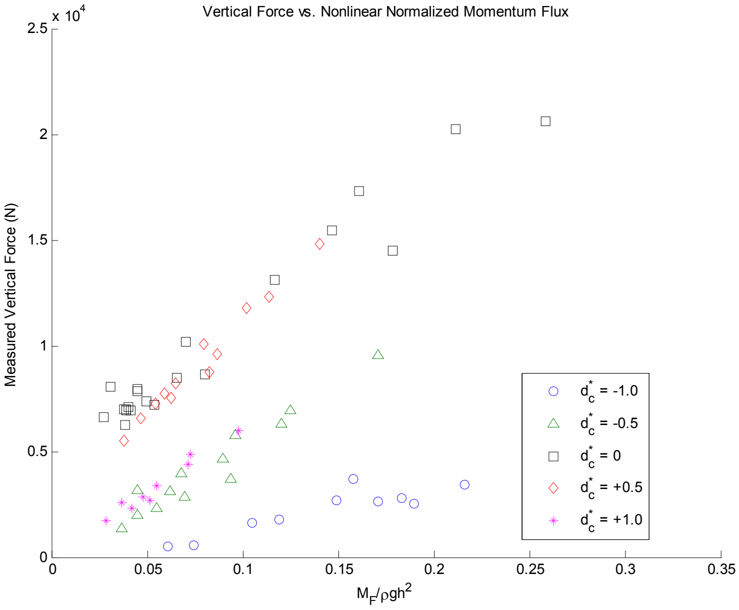

Figure 6.6. Measured Fv,1/3 vs. nonlinear wave momentum flux parameter for random wave trials.

6.2 CALCULATION OF FORCES USING MOMENTUM FLUX

After observing the relationship between the measured forces and the wave momentum flux parameter, the next logical step was to attempt to model these forces using momentum flux. Previously, the depth integrated horizontal momentum flux had been calculated using Equation (6.2). To model the horizontal forces, this equation was modified to provide a more direct relationship to the bridge setup. Instead of integrating momentum flux over the entire water column, the momentum flux was integrated only over the elevation of the bridge deck. This approach yielded a parameter known as the wetted surface horizontal momentum flux,

$$M_{FH}(x,t) = \int_{z_b-h}^{z_b+h_b-h} (p_d + \rho u^2)\,dz \qquad (6\text{-}8)$$

where z_b is the elevation of the low chord of the bridge (1.89 m) and h_b is the height of the bridge deck (0.28 m). Maximum horizontal momentum flux was assumed to occur when the wave crest reached the offshore face of the bridge deck. Pressure and velocity were calculated at this location using extended linear wave theory and the measured wave amplitude from the trials. For trials conducted at $d^* = 0$, the momentum flux was integrated from z = 0 to z = 0.28 meters. To calculate the maximum horizontal force, the maximum wetted surface horizontal momentum flux was multiplied by the length of the bridge span, *S* (i.e., the width of the wave flume). The resulting horizontal force equation is

$$F_H = (M_{FH})_{max} \times S \qquad (6\text{-}9)$$

To model the vertical force, the concept of horizontal momentum flux was transformed to vertical momentum flux. The theory behind this transformation is to calculate the instantaneous flux of momentum across the horizontal plane projected by the bridge. The first step in this transformation was to calculate the vertical momentum flux, mv, given by

$$m_v(x,z,t) = p_d + \rho w|w| \qquad (6\text{-}10)$$

where *w* is the vertical particle velocity. Maximum vertical momentum flux was assumed to occur when the wave crest was located at a point between the offshore face and the center of the bridge. Once the wave crest passes the midpoint of the bridge width, more than half of the bridge would be subjected to the negative (downward) velocities associated with the trailing edge of the wave crest. This location was determined using an iterative process for each trial. To calculate the vertical momentum flux across the bridge, the momentum flux was integrated along the width of the bridge, in the x-direction, and then depth-averaged along the elevation of the bridge deck. For cases where the wave crest does not exceed the top of the deck, the momentum flux is depth-averaged over the wetted elevation of the bridge. The resulting wetted surface vertical momentum flux is given by

$$M_{FV}(x,z) = \frac{1}{h_b}\int_{z_b-h}^{z_b+h_b-h}\int_{W/2-\delta}^{W/2+\delta} (p_d + \rho w|w|)\,dx\,dz \qquad (6\text{-}11)$$

where W is the width of the bridge and δ is a constant, representing the location of the wave crest, relative to the center of the bridge. The notation above is valid when x = 0 occurs at the center of the bridge.

To obtain the vertical force, the maximum value generated by Equation (6.11) is multiplied by the bridge span length, *S*. The resulting vertical force equation is

$$F_v = (M_{fv})_{max} \times S \qquad (6\text{-}12)$$

Figure 6.7 shows the comparison of measured versus calculated horizontal forces for the regular wave trials using the method described above. The model shows good agreement with the measured forces, with the exception of data from trials conducted at $d^* = -1.0$, where the model tends to under-predict the forces. This is likely due to the linear method used to resolve the incident and reflected waves, which produces smaller than actual waves when conditions become severely nonlinear.

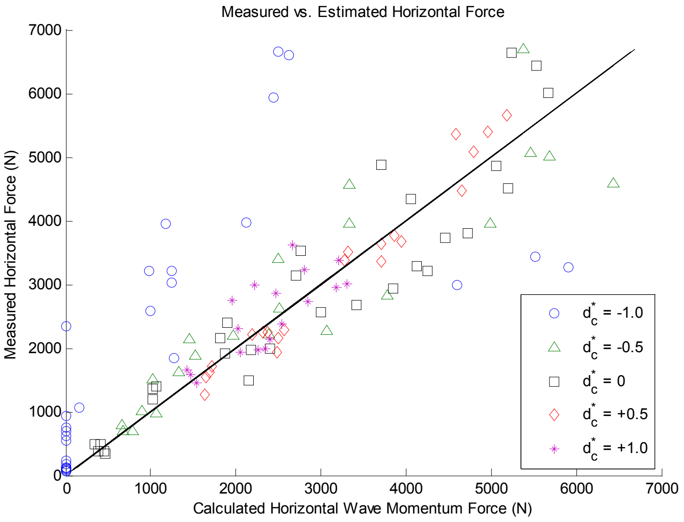

Figure 6.7. Observed vs. predicted horizontal force for regular wave trials.

Predicted and measured horizontal forces for the random wave trials are shown in Figure 6.8. H_s and T_p were used to calculate the horizontal momentum flux for these trials and the calculated values were compared to $F_{1/3}$. For the trials where the still water level (SWL) was even with or above the low chord of the bridge, the agreement is excellent. For the trials at d^*=-1.0 and -0.5 the model under-predicts the forces. The previously discussed issues with the nonlinear wave measurements may affect these calculations, but a greater factor may be the method used to calculate the forces. For trials at $d^* = -1.0$ and -0.5, the sample size used to calculate H_s is far larger than that used to calculate $F_{1/3}$, as only a fraction of the waves are striking the bridge at these water levels. The result is a wave height that is proportionately smaller than the calculated $F_{1/3}$. The smaller wave height will yield a smaller modeled force.

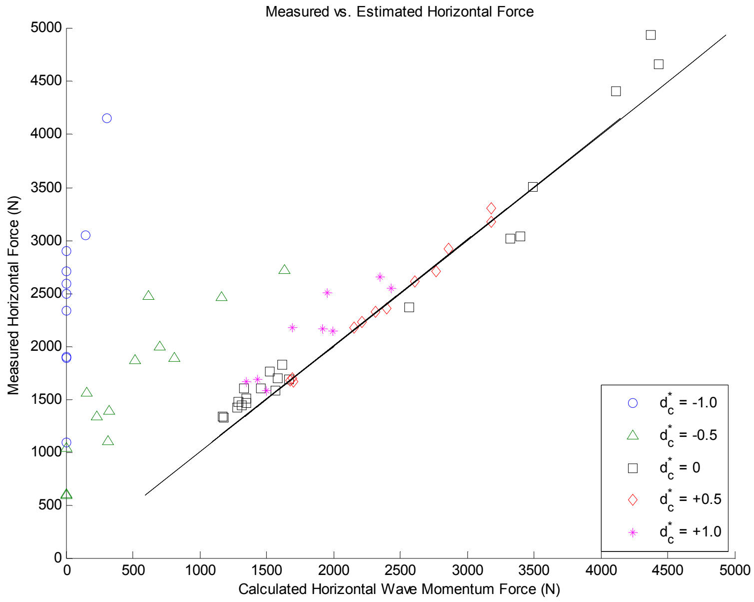

Figure 6.8. Measured vs. calculated horizontal force, Fh,1/3 for random wave trials.

Figure 6.9 and Figure 6.10 show the comparison of the measured and calculated vertical forces for the regular and random wave trials, respectively. In both of these plots, the model over-predicts the vertical forces. As with the horizontal forces, the model performs best at $d^* = 0$ and +0.5 and performs poorly at $d^* = -1.0$.

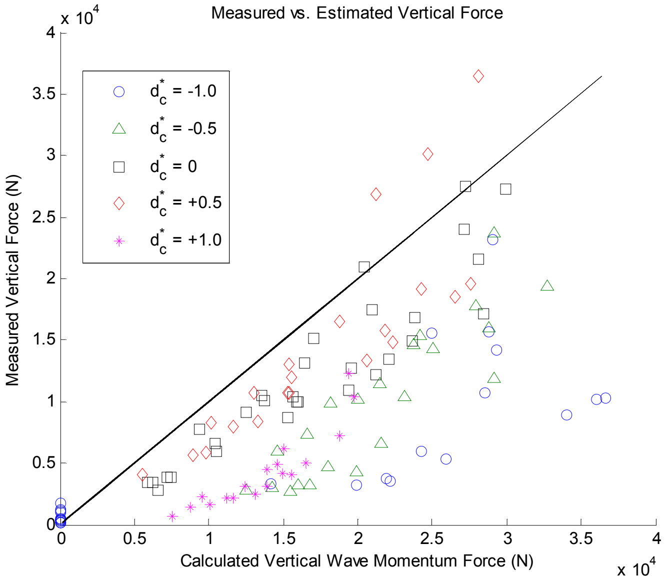

Figure 6.9. Measured vertical force vs. calculated vertical force for regular wave trials.

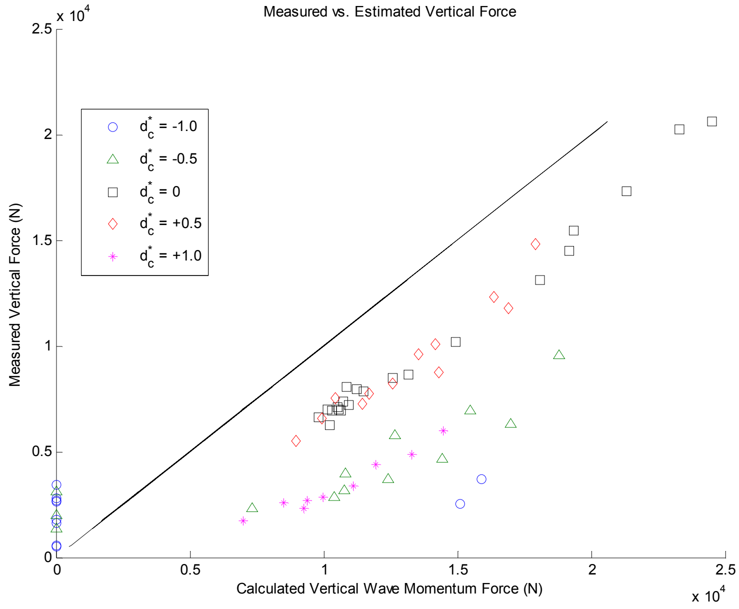

Figure 6.10. Measured vs. calculated vertical force, Fv,1/3, for random wave trials.

7.0 COMPARISON OF MEASURED FORCES TO AASHTO GUIDELINES

Recently developed AASHTO guidelines for wave forces on coastal bridges were compared to the measured forces from the regular wave trials (*AASHTO, 2008*). Because the equations in the guidelines require prototype scale inputs, the bridge specimen geometry, water depths, and wave conditions were scaled to prototype using Froude scaling. Wave lengths were calculated assuming linear dispersion. The guideline coefficients for AASHTO Type III girders were used and the maximum Trapped Air Factor (TAF) was calculated assuming a diaphragm height of two-thirds times the girder height. The resulting forces were then reduced to model scale and plotted with the measured forces, as shown in Figure 7.1, Figure 7.2 and Figure 7.3. These figures are representative of the entire range of trials. A complete set of comparison plots can be found in Appendix G.

The AASHTO guidelines compare reasonably well with the measured horizontal forces. The only exception was that at $d^* = -1.0$, the guidelines tend to under-predict the forces. This is not a significant shortfall, as the forces at this water level are likely too small to cause damage.

The guidelines calculate both a quasi-steady vertical force and a slamming vertical force which is to be added to the quasi-steady force to produce a total force. The quasi-steady vertical force is presented as range of values, based on the minimum and maximum TAF calculated by the guidelines. The total force presented in the figures below is based on the maximum quasi-steady force. In general, the measured vertical forces compared most favorably to the quasi-steady forces, while the total force calculation over-predicted the vertical force. This is consistent with the observations presented in Chapter 5, which found no impact spike or slamming force in the load cell data. The vertical forces are slightly under-predicted at the lower water levels, as seen in Figure 7.1. The guidelines did a good job of predicting the quasi-steady forces for the full range of conditions tested at $d^* = 0$ (see Figure 7.2).

Significant deviations from the measured vertical forces occurred at $d^* = +0.5$ and $+1.0$. At these water levels, the quasi-steady forces predicted by the guidelines grossly overstate the vertical forces experienced, as seen in Figure 7.3. The guidelines acknowledge that the equations are conservative for cases where the bridge becomes partially or completely submerged, stating that the hydraulic model experiments used to develop the code showed a slight decrease in forces when these conditions occur.

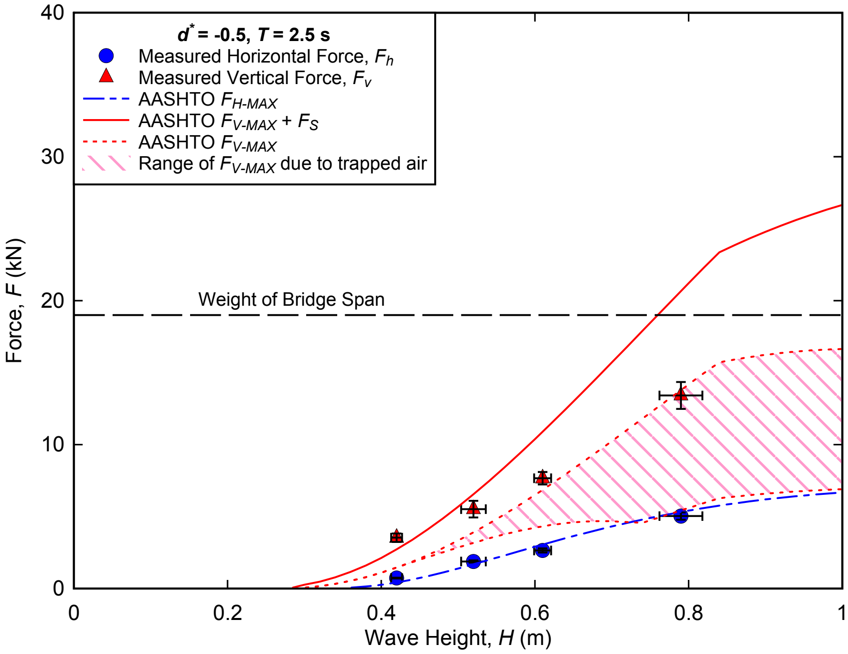

Figure 7.1. Comparison of AASHTO guidelines with measured forces, d* = -0.5, T = 2.5 s.

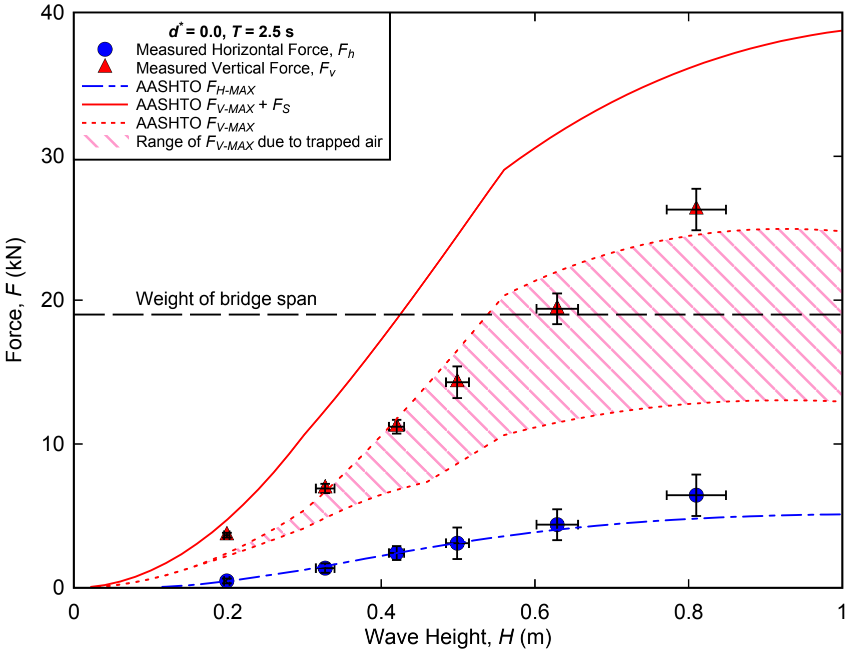

Figure 7.2. Comparison of AASHTO guidelines with measured forces, d* = 0, T = 2.5 s.

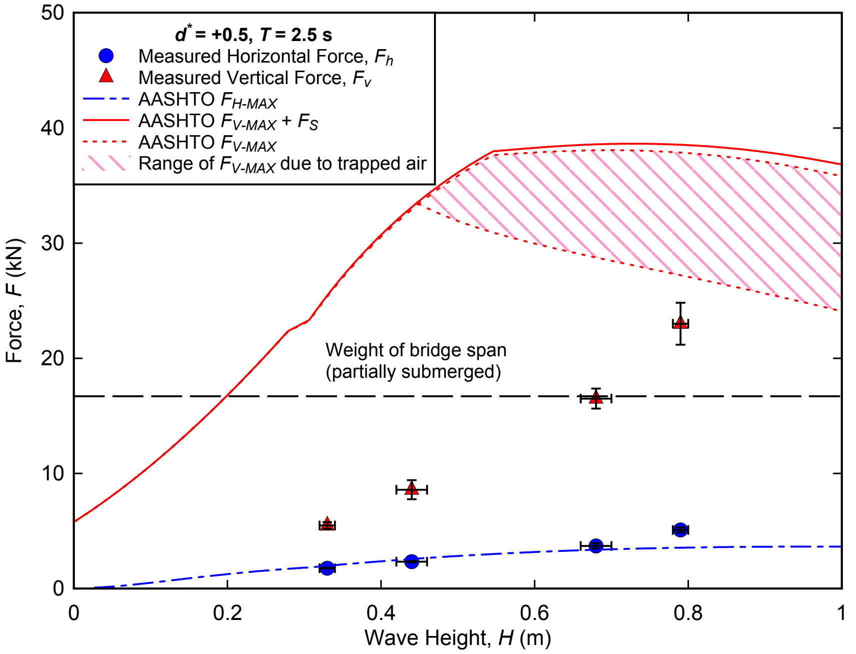

Figure 7.3. Comparison of AASHTO guidelines with measured forces, d* = +0.5, T = 2.5 s.

8.0 ANALYSIS OF FORCE DISTRIBUTIONS FOR RANDOM WAVE TRIALS

When designing coastal structures, the design conditions must be determined to estimate the maximum forces which the structure must survive. The primary elements of these conditions are normally wave height, wave period, water level, current and wind. The values for these elements can be determined through extreme event analysis. Given a return period and a sample of historic environmental data, design storm conditions can be calculated. These storm conditions can then be entered into numerical wave generation and storm surge models to determine wave conditions at the structure. The typical output of these models consists of significant wave height, H_s, peak period, T_p, wave direction at peak period, and storm surge elevation. The Rayleigh distribution can be used to approximate the distribution of wave heights.

Once the design conditions are determined, a logical next step is to calculate the design forces. One method for this is to calculate a theoretical maximum wave height and then apply a model such as the AASHTO guidelines or the wave momentum flux method discussed in the previous chapters. A second method is to determine the distribution of forces resulting from the design conditions and calculate the design force based on a probability of exceedance. This second method allows the designer to assess the risk and make an educated decision on the level of design for a given structure. This method also has the advantage of directly calculating the exceedance probability of the forces rather than calculating the exceedance probability of a wave height and then converting that wave height to a force. The latter requires the designer to make the assumption that the probability distributions of the waves and forces can be correlated using the force calculation model of choice.

While there is a large amount of data to support the calculation of realistic wave height distributions, there is very little data available to calculate distributions of wave forces. This chapter presents a preliminary investigation into the calculation of probability distributions of wave forces on coastal bridges and their correlation to wave conditions at the bridge.
Using Goda's method for statistical analysis of extreme waves (*Goda, 2000*), the horizontal and vertical forces measured during the random wave trials were compared to three distribution functions commonly used for extreme event analysis. These distributions, along with their cumulative distribution functions, *F(x)*, are:

Fisher-Tippett type I (FT-I) or Gumbel distribution:

$$F(x) = \exp\left[-\exp\left(-\frac{x-B}{A}\right)\right] \quad : \quad -\infty < x < \infty \tag{8-1}$$

Fisher-Tippett type II (FT-II) or Frechét distribution:

$$F(x) = \exp\left[-\left(1 + \frac{x - B}{kA}\right)^{-k}\right] \quad ; \quad B - kA \leq x < \infty \tag{8-2}$$

Weibull distribution:

$$F(x) = 1 - \exp\left[-\left(\frac{x - B}{A}\right)^{k}\right] \quad ; \quad B \leq x < \infty \tag{8-3}$$

where A is the scale parameter, B is the location parameter, and k is the shape parameter. This k should not be confused with the k that is commonly used to denote wave number. It should be noted that a Weibull distribution with $k = 2$ behaves similarly to a lognormal distribution.

The discrete horizontal and vertical peak forces for each random wave trial were normalized by the average of the highest one-third of the respective forces, $F_{1/3}$ in an attempt to reduce the effect of varying wave conditions on the force distributions. The normalized forces were then placed in descending order and an unbiased probability was calculated for each using Goda's unbiased position plotting formula, given by

$$\hat{F}_{(m)} = 1 - \frac{m - \alpha}{N_T + \beta} \quad , \quad m = 1, 2, \ldots, N \tag{8-4}$$

where α and β are empirical coefficients developed by Goda, N is the number of forces in the sample and N_T is the total number of forces. For this analysis, a peak over-threshold method was chosen to provide the best fit near the tail of the distribution where the extreme events occur. Through trial and error, a threshold of 1.0 ($F / F_{1/3}$) was chosen to provide the optimum balance between sample size and the fit of the distribution tail. Early in the development of this method, it was realized that the number of forces measured in a trial varied greatly depending on the water level. For trials where the SWL was beneath the low chord of the bridge ($d^* = -1.0$ and -0.5) the sample size for the forces was very small, as only the highest waves struck the bridge. Conversely, at $d^* = 0$ and above, the sample size was roughly equal to the number of waves, which was approximately 300. To provide uniformity among the trials, the number of waves measured for each trial was used for N_T. This also allows the probability to be directly related to the number of waves, which is a parameter that can be easily determined for a given design condition and storm duration.

Once the measured force probabilities were calculated, they were compared to the probability functions in Equations (8.1), (8.2), and (8.3). A least-squares method was used to determine how well each candidate distribution fit. Because this method can evaluate two parameters and the FT-II and Weibull distribution functions contain three parameters (A, B, and k), four different values of k were evaluated for both functions. The resulting probability functions evaluated are listed in Table 8.1. For each of these nine probability functions, a best estimate of A and B were calculated along with a correlation coefficient, R. The candidate distribution with the highest correlation to the measured forces was selected as the best-fit distribution for that trial.

Table 8.1. The distribution functions used in the force distribution analysis.

Distribution Name	**k**
Fisher – Tippett type I (FT – I)	N/A
Fisher – Tippett type II (FT – II),	$k = \begin{cases} 2.5 \\ 3.33 \\ 5.0 \\ 10.0 \end{cases}$
Weibull,	$k = \begin{cases} 0.75 \\ 1.0 \\ 1.4 \\ 2.0 \end{cases}$

This process was repeated for all of the random wave trials, for horizontal and vertical forces. Overall, the best-fit distributions exhibited good correlation to the trial data, with an average *R*-value of 0.97 for both the horizontal and vertical forces. The correlations are highest for $d^* = +1.0$, followed in order by $d^* = +0.5$, 0, and -0.5. Due to the small sample size of forces for trials at $d^* = -1.0$, no credible distribution could be determined. There was no dominant best-fit distribution, but the Weibull distribution (k=2) was selected for 51% of the trials for horizontal forces and 56% of the trials for vertical forces. Table 8.2 contains a summary of the best-fit analysis for trials conducted at $d^* = 0$. Summaries of the other water levels can be found in Appendix H.

The best-fit probability distribution and the force data were then plotted at exceedance probabilities as shown in Figure 8.1. These plots can be used in conjunction with the $F_{1/3}$ vs. H_s plots presented in Chapter 5 to calculate design forces, by following these steps:

1. Calculate design water level and wave condition for the bridge.
2. Select the exceedance probability chart for the water level and wave conditions that are closest to the design conditions.
3. Determine the acceptable risk for the bridge and select the corresponding normalized force from the chart.
4. Using the $F_{1/3}$ vs. H_s plot that corresponds with the water level on the probability exceedance chart, find the value for $F_{1/3}$ for the design H_s.
5. Multiply the normalized force from the probability exceedance plot by $F_{1/3}$ to calculate the design force.

Table 8.2. Summary of probability distribution analysis for random wave trials, *d** = 0.

			Horizontal Forces					Vertical Forces				
Trial	Hs	Tp	N	Distribution	A	B	R	N	Distribution	A	B	R
1301	0.37	1.8	26	Weibull k= 2.0	0.963	-0.324	0.981	28	Weibull k= 2.0	0.501	0.362	0.972
1302	0.35	2.1	45	FT-II k= 10.0	0.220	0.588	0.971	41	FT-II k= 10.0	0.152	0.742	0.985
1303	0.33	2.1	42	Weibull k= 1.4	0.763	-0.239	0.994	45	Weibull k= 2.0	0.974	-0.353	0.972
1304	0.38	1.9	45	Weibull k= 1.4	0.620	0.001	0.994	44	Weibull k= 2.0	0.588	0.223	0.972
1305	0.33	1.9	25	Weibull k= 2.0	1.943	-1.832	0.981	27	FT-I	0.235	0.593	0.965
1306	0.35	1.9	40	FT-II k= 3.33	0.125	0.765	0.994	42	Weibull k= 2.0	0.993	-0.366	0.972
1307	0.34	2.0	39	Weibull k= 2.0	1.578	-1.297	0.981	44	Weibull k= 2.0	0.837	-0.127	0.972
1308	0.36	1.9	15	Weibull k= 1.0	0.543	-0.119	0.990	13	Weibull k= 2.0	0.827	-0.074	0.972
1309	0.35	2.0	43	Weibull k= 2.0	1.292	-0.817	0.981	42	Weibull k= 2.0	0.744	0.002	0.972
1310	0.36	2.1	43	Weibull k= 2.0	0.801	-0.037	0.981	41	Weibull k= 2.0	0.824	-0.152	0.972
1311	0.34	1.9	31	Weibull k= 1.4	1.269	-1.267	0.994	42	Weibull k= 2.0	0.855	-0.110	0.972
1312	0.35	2.1	24	FT-II k= 2.5	0.128	0.633	0.983	31	Weibull k= 1.4	0.568	0.074	0.939
1314	0.47	2.1	51	Weibull k= 2.0	0.945	-0.258	0.981	40	Weibull k= 1.4	0.388	0.375	0.939
1315	0.55	2.5	49	Weibull k= 2.0	0.994	-0.320	0.981	50	Weibull k= 2.0	0.563	0.271	0.972
1316	0.39	2.4	46	Weibull k= 2.0	1.279	-0.839	0.981	46	Weibull k= 2.0	0.903	-0.270	0.972
1317	0.41	2.9	47	Weibull k= 0.75	0.255	0.326	0.946	39	FT-II k= 5.0	0.177	0.568	0.975
1318	0.58	2.9	40	Weibull k= 2.0	1.033	-0.450	0.981	42	Weibull k= 1.4	0.416	0.337	0.939
1319	0.64	2.5	24	Weibull k= 2.0	0.620	0.201	0.981	24	Weibull k= 2.0	0.413	0.481	0.972
1320	0.70	2.9	47	Weibull k= 2.0	0.729	0.018	0.981	44	Weibull k= 2.0	0.636	0.143	0.972
1321	0.74	3.6	45	Weibull k= 2.0	0.845	-0.167	0.981	44	Weibull k= 2.0	0.686	0.066	0.972
1323	0.58	3.5	40	Weibull k= 2.0	1.311	-0.847	0.981	39	Weibull k= 2.0	0.922	-0.293	0.972

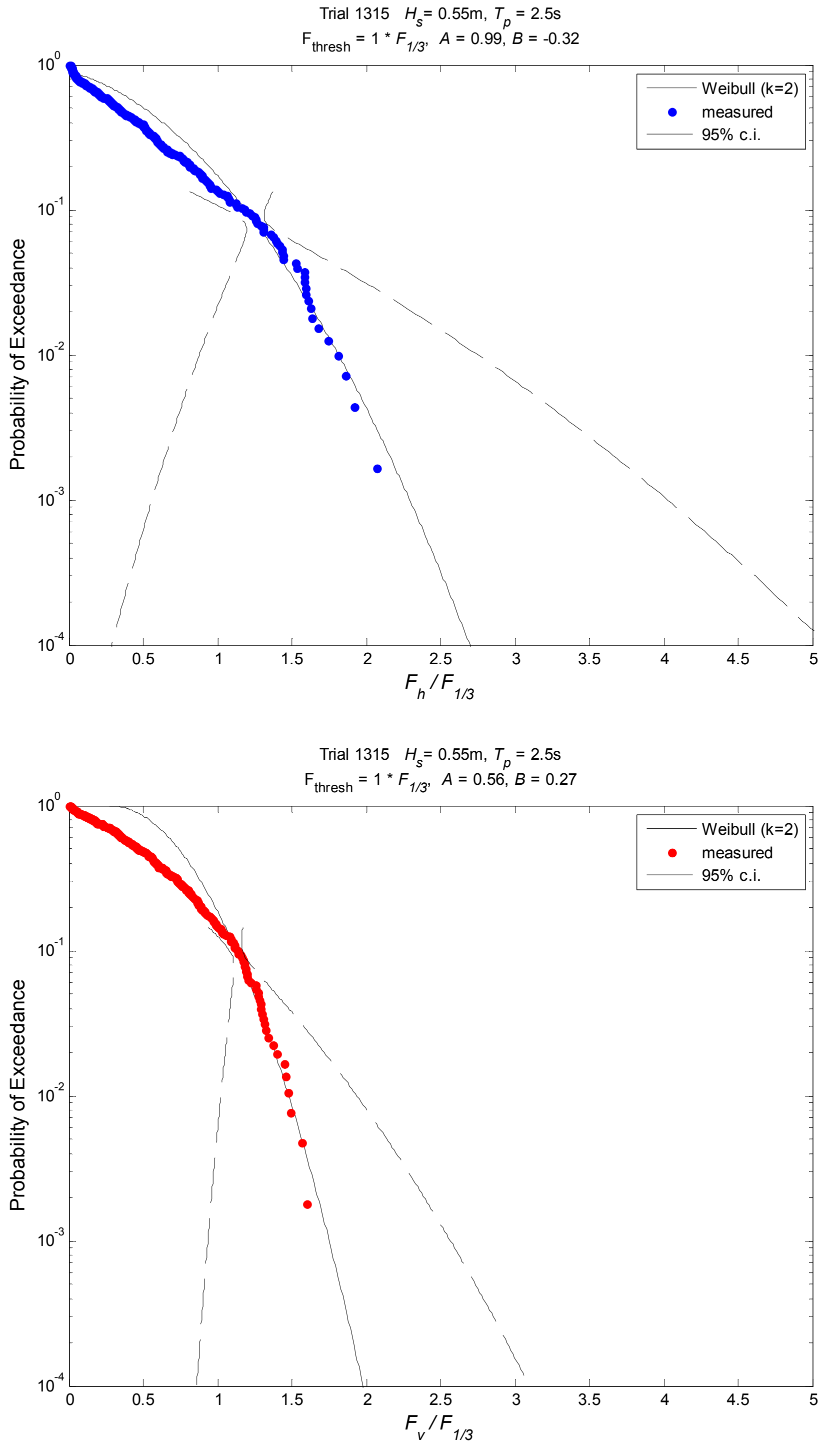

Figure 8.1. Exceedance probabilities for normalized horizontal (top) and vertical (bottom) forces for random wave trial 1315 (d* = 0, Hs = 0.55 m, Tp = 2.5s).

The test conditions used to develop the exceedance probability plots in Figure 8.1 correspond to the peak conditions at the U.S. 90 Bridge over Biloxi Bay during Hurricane Katrina. Using these plots to illustrate the process described above, the 1% design case (1 out of every 100 waves would exceed the design force) yields a normalized vertical force of 1.5. From the plot in Figure 8.2, a value of 15 kN is obtained for a hypothetical design condition of $H_s = 0.55$ m. The calculated vertical design force would then be 15 kN x 1.5 = 22.5 kN.

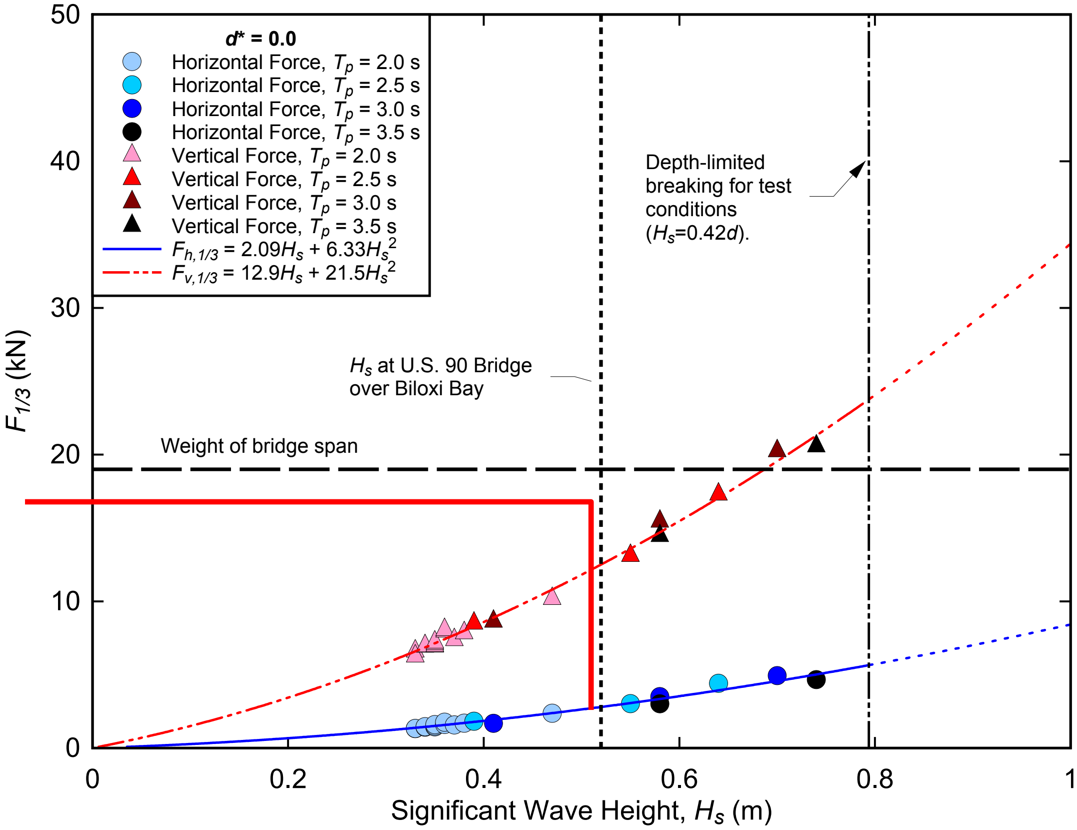

Figure 8.2. Force vs. Wave Height plot used to calculate F,1/3, based on design Hs of 0.55m for d* = 0.

This method does have its drawbacks, as two probability exceedance charts are created for each trial. For these experiments, 110 such plots were created, making their use cumbersome and confusing. To reduce the number of charts, the trials were grouped by water level and analyzed together. Using the same method described above, probabilities of measured forces were calculated for each individual trial, but instead of selecting the best fit distribution based on a single trial, the distribution as well as the scale, location and shape parameters were selected based on the best fit of all of the trials for a given water level. As with the previous method, a peak over-threshold technique was employed, using a threshold of 1.0 $(F / F_{1/3})$. The resulting plots contained significantly more scatter. The horizontal and vertical force probability exceedance plots for $d^* = 0$ are shown in Figure 8.3. Plots for all of the water levels can be seen in Appendix H. While these plots do provide some promise for the development of universal force distributions, the current method would require a safety factor of two or more. For some of the plots, the scatter appears to be related to the scale parameter and could be reduced if a more effective method of normalizing the forces could be found.

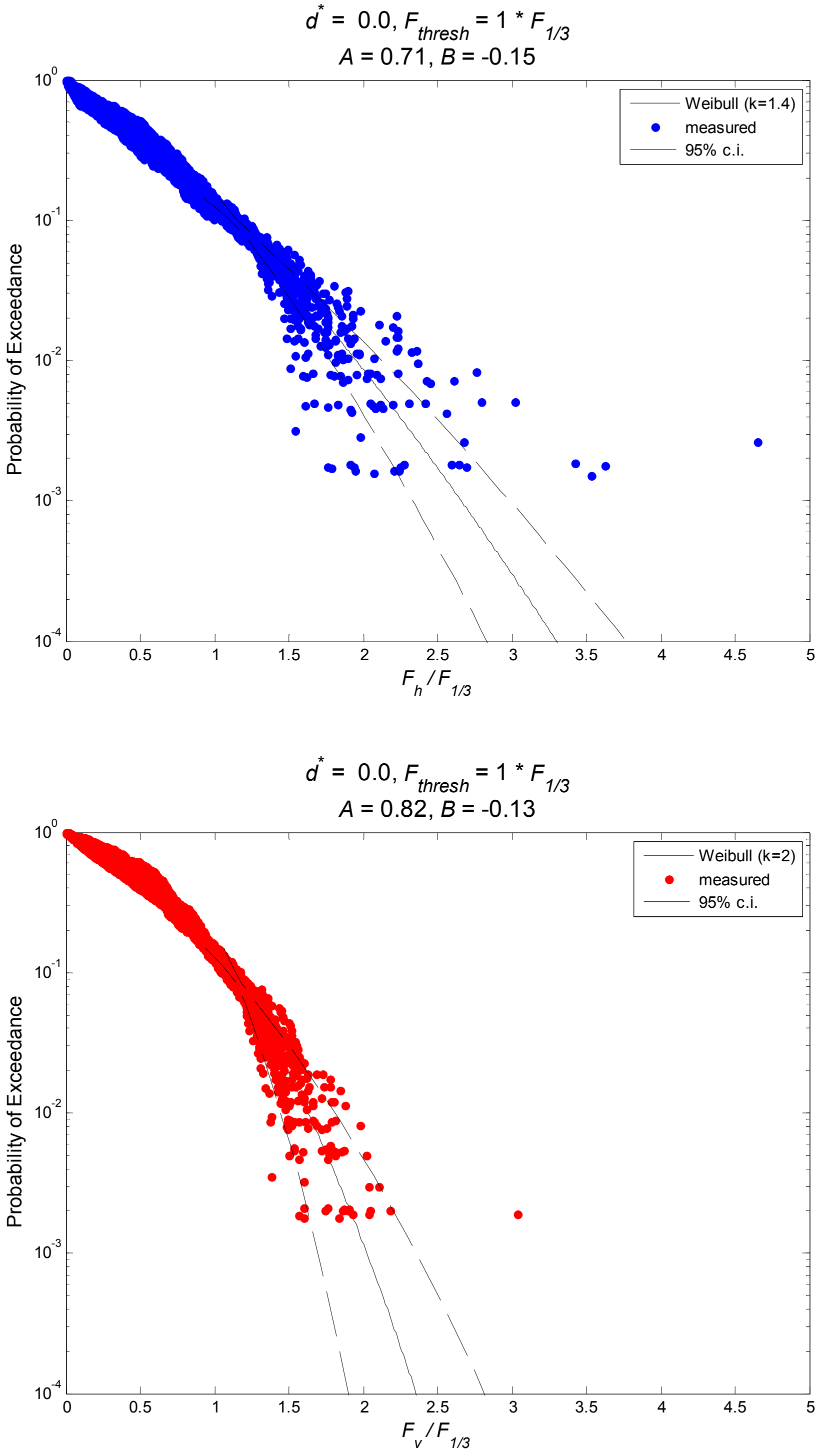

Figure 8.3. Exceedance probability for normalized horizontal forces (top) and vertical forces (bottom), d* = 0.0

9.0 DISCUSSION AND CONCLUSIONS

9.1 SIGNIFICANCE OF IMPACT PRESSURE AND SLAMMING FORCE

Past research has shown that pressures due to wave impact followed a common pattern of an initial, short-duration, high-amplitude impact pressure followed by longer-duration quasi-static pressure (*McConnell et al., 2004; Cuomo et al., 2007; Bullock et al., 2001*). Integrating these pressures over the surface of the structure yields a slamming force followed by a quasi-steady force. The load cell data collected in this experiment does not exhibit the slamming force suggested by previous research. The impact spike **was** witnessed in pressure gauge data collected between the girders (Figure 5.1), but was not seen in the external girders (Figure 5.2). One possible explanation for the lack of a pressure spike in the external girder pressures is that the air is allowed to vent at the external girders, while the air is trapped between the internal girders. It is the compression of the trapped air which leads to the sharp increase in pressure. This theory is consistent with the findings of Cuomo *et al*. (2007) as well as those of AASHTO (2008).

The lack of an impact spike in the force data is of more interest. This cannot be attributed to the relatively slow sampling rate of 125 Hz, as the impact spike was observed in the pressure data. The load cells were capable of measuring the slamming force, but this force did not appear in the data. The lack of a slamming force is likely due to the mass of the structure and the experimental setup. The fundamental goal of this research was to investigate the forces behind the bridge failures along the Gulf Coast. The bridge model and the experimental setup were designed with this goal in mind. Investigation of these failures found that the bridge superstructures were removed from their supports through a combination of vertical and horizontal forces. The load cells were positioned as to measure the reaction force on the bent cap connections. When a wave strikes the bridge, an impact pressure may be generated, but this pressure does not manifest itself as reaction forces at the bent cap. The large mass of the bridge superstructure dissipates this impact. There may be localized forces and resulting damage such as concrete spalling or cracking, but these forces are not the cause of the failures witnessed during Hurricanes Ivan and Katrina. For many of the failed bridges, the superstructures were pushed one deck width or more by the waves, supporting the conclusion that quasi-steady forces are the root cause of the failures.

9.2 RELATIONSHIP BETWEEN WAVES AND FORCES

As expected, wave height was the largest determinant of forces. The relationship between wave height and force appears to be a function of H^2. This relationship and the observation that the vertical forces are significantly larger than the horizontal forces indicate that dynamic pressure is a major factor.

The relationship between force and water level is more complex as the water level for these experiments was a combination of water depth and bridge clearance, making it difficult to separate the effects of each. One of the effects of bridge clearance is intuitive as smaller clearances will allow a larger portion of the wave to strike the bridge. The observation that forces decreased as the bridge became submerged suggests that the forces are influenced by particle velocity and acceleration. This influence was also observed at lower water levels, where steeper waves produced larger forces compared to less steep waves of similar height.

The complex relationship between wave period and force also supports the conclusion that particle velocity and acceleration are factors behind the forces. According to linear wave theory, if wave height and water depth are held constant, an increase in period (and wave length) will lead to larger velocities but smaller accelerations. Conversely, shorter (and steeper) waves have smaller velocities but larger accelerations. An analysis of the force vs. period plots in Appendix E leads to the conclusion that the relative influences of velocity and acceleration varies with water level.

Complicating the effect of water level is the buoyancy force that exists at the higher water levels. As previously noted, smaller forces were often associated with the submerged cases, but these figures can be misleading as the measured forces do not account for buoyancy. When analyzing the critical design condition, the total vertical force on the bridge must be evaluated. In some cases, the highest forces were observed at $d^* = 0$, but the force produced by the same wave at $d^* = +0.5$ combined with the buoyancy produces a higher total vertical force. If the design conditions dictate that the bridge will become partially or completely submerged, all water levels must be evaluated to determine the design force.

The relationship between the waves and forces for the random wave trials was similar to that of the regular wave trials. The influence of wave period on the forces was diminished by the frequency spectrum of the waves, but the effect of wave height and water level remained strong.

9.3 APPLICABILITY OF MOMENTUM FLUX

The plots relating momentum flux to the measured forces seem to support the conclusion that forces are influenced by a combination of dynamic pressure, particle velocity and acceleration. The correlation between momentum flux and forces suggest that momentum flux can be used to calculate the forces. The horizontal forces correlate better compared to vertical forces. This may be a function of the surface over which these forces are applied. The horizontal forces are applied to the relatively flat face of the bridge deck and its supporting girders, allowing a more linear interaction between wave and structure. Conversely the vertical forces are applied over a much more complex surface. The vertical force is further complicated by the compression of air between the girders.

The model developed to calculate the forces using momentum flux demonstrates the complexities associated with the vertical forces. The model performed well for the horizontal forces. The only limitation appeared to be the accuracy of the wave height measurements. The model did not perform as well for the vertical forces. For almost every trial, the model over-predicted the force. This indicates that the exchange of momentum between the waves and the bridge is much more efficient for horizontal forces than vertical forces. If there are unseen losses in this process that are not modeled by the analytical equations of momentum flux, then these losses can be accounted for with an empirical coefficient representing the efficiency of the momentum exchange. This coefficient could be easily calculated for each water depth as there appeared to be a direct relationship between the model and the forces.

This method could also apply to the random wave conditions. For the horizontal forces, the model performed very well except for the trials at $d^* = -0.5$ (trials at $d^* = -1.0$ were not considered in the evaluation of the model). Based on the performance of the model at the other water levels, the discrepancies for the $d^* = -0.5$ may be related to the method used to calculate the force. For the vertical forces, the model again over-predicated the forces, but the calculated and measured forces exhibited good correlation. Like the regular wave trials, an empirical correction factor could be easily calculated for each water depth.

9.4 COMPARISON OF AASHTO GUIDELINES

For the cases where the still water level was at or below the low chord of the bridge, the horizontal and vertical quasi-steady forces predicted by the AASHTO guidelines compared reasonably well to the measured forces. The total vertical force (which included a slamming force) predicted by the guidelines was larger than the measured vertical force for almost every trial. As previously discussed, the measured forces did not exhibit a slamming force. Designers should use their judgment when deciding whether or not to include this slamming force in the design load, as the quasi-steady force alone may be sufficient for applications.

The guidelines appear to over-predict the forces once the bridge becomes partially submerged. At $d^* = +0.5$ and $+1.0$, the measured forces leveled out or even decreased compared to the lower water levels. The guidelines state that the wave flume experiments used to develop the model also showed a decrease in forces once the bridge became submerged and the equations are conservative at these levels (*AASHTO, 2008*). The data from this experiment indicates that the guidelines are very conservative at these levels. Designers should use caution when using these guidelines if the design condition results in partial or complete submergence of the bridge.

9.5 PROBABILITY-BASED ANALYSIS OF RANDOM WAVE FORCES

The probability-based analysis demonstrated that a distribution of forces induced by random waves on a complex structure such as a bridge can be approximated using commonly used probability distribution functions. The analysis examined nine variations of three different functions and found that the function that best fit the measured forces varied from trial to trial. In general, the Weibull distribution ($k = 2$) performed the best and was the most accurate predictor of force distributions for over half of the trials tested. The correlation between data in a single trial and the best-fit distribution was very strong, but no correlation between trial conditions and the best-fit distribution function could be found. In an attempt to find a common distribution for all of the trials conducted at a given water level, the resulting distribution contained significantly more scatter than the individual trials.

9.6 RECOMMENDED FUTURE WORK

This thesis represents a first step in the analysis of the data collected during these experiments. The analysis primarily involved the evaluation of wave gauge and load cell data using linear methods. The possibilities for additional work are virtually unlimited.

The relationship between pressure and force should be investigated further. So far, the analysis of the pressure has been limited to a qualitative evaluation. The specimen was fitted with 13 pressure gauges at locations designed to provide a comprehensive view of the pressure distributions along the surface of the specimen. Defining the pressure distribution is a key step in finding an analytical method to model the forces. In addition, analysis of the pressure gauges located between the girders may lead to a better understanding of scale effects due to the elastic compression of air in models.

The relationship between forces, wave conditions and water level can be refined. Nonlinear methods of resolving incident and reflected waves will produce a more accurate wave crest elevation, which is an important parameter in existing models (*AASHTO, 2008; Cuomo et al., 2007; Douglass et al., 2006; McConnell et al., 2004*).

The application of momentum flux is a promising avenue towards an analytical model. The effect of using nonlinear equations to calculate velocity and pressure should be investigated. Theory holds that applying nonlinear equations to the nonlinear conditions tested should produce more accurate results. In lieu of an analytical model, an empirical model based on physical processes can help engineers determine design loads. A simple model relating momentum flux to forces through a coefficient based on water level may be possible.

The development of a probability-based model for calculating forces can help both designers and owners make decisions regarding design levels. The analysis conducted in this thesis has shown that modeling probability distributions is possible and can provide accurate estimates of extreme events. The next step in this process is the development of a probability-based model that relates the distribution to specific wave conditions and water levels. Reducing the scatter in the measured data is vital to developing an accurate model. One way to reduce the scatter is to find an innovative method of normalizing the measured forces.

One of the primary goals of the experiment was to investigate the effect of substructure flexibility on the measured forces. The data set contains 173 trials of regular and random waves on the dynamic setup. This data has yet to be analyzed in depth and could provide valuable insight into the design of future bridges.

The experiments described in this thesis are the largest wave-on-bridges experiments conducted to date and have proven the value of large-scale modeling of complex wave-structure interactions in nearshore conditions. While there is much work still to be done, the analysis performed has provided valuable insight into the wave forces on coastal highway bridges.

BIBLIOGRAPHY

AASHTO. (2008). *Final Draft: Guide Specifications for Bridges Vunerable to Coastal Storms (BVCS-1).* Washington, DC: American Association of State Highway and Transportation Officials.

Bea, R. G., Xu, T., Stear, J., & Ramos, R. (1999). Wave Forces on Decks of Offshore Platforms. *Journal of Waterway, Port, Coastal, and Ocean Engineering , 125* (3), 136-144.

Bullock, G. N., Crawford, A. R., Hewson, P. J., Walkden, M. J., & Bird, P. A. (2001). The influence of air and scale on wave impact pressures. *Coastal Engineering , 42*, 291-312.

Chen, Q., Wang, L., & Haihong, Z. (in press). Hydrodynamic investigation of coastal bridge collapse during Hurricane Katrina. *Journal of Hydraulic Engineering* .

Cuomo, G., Tirindelli, M., & Allsop, W. (2007). Wave-in-deck loads on exposed jetties. *Coastal Engineering , 54*, 657-679.

Douglass, S. L., Chen, Q., Olsen, J. M., & Edge, B. L. (2006). *Wave Forces on Bridge Decks.* Washington, DC: U.S. Department of Transportation Federal Highway Administration.

Douglass, S. L., Hughes, S. A., Rogers, S., & Chen, Q. (2004). *The Impact of Hurricane Ivan on the Coastal Raods of Florida and Alabama: A Preliminary Report.* Coastal Transportation Engineering Research and Education Center. Mobile, AL: University of South Alabama.

Florida DOT. (2008, October 01). *Design Build Contracts Status as of: 09/30/2008.* Retrieved October 14, 2008, from Florida Department of Transportation: http://www.dot.state.fl.us/construction/DesignBuild/DBGeneral/DesignBuildReport.pdf

Goda, Y. (2000). *Random Seas and Design of Maritime Structures* . Singapore: World Scientific.

Graumann, A., Houston, T., Lawrimore, J., Lecinson, D., Lott, N., McCown, S., et al. (2005). *Hurricane Katrina A Climatological Perspective.* National Climatic Data Center. Asheville, NC: NOAA.

Hughes, S. A. (1993). *Physical Models and Laboratory Techniques in Coastal Engineering.* Singapore: World Scientific Publishing.

Hughes, S. A. (2004). Wave momentum flux parameter: a descriptor for nearshore waves. *Coastal Engineering , 51*, 1067-1084.

Kaplan, K., Murray, J. J., & Yu, W. C. (1995). Throretical Analysis of Wave Impact Forces on Platform Deck Structures. *Proceedings of the 14th International Conference on Offshore Mechanics and Arctic Engineering. 1A*, pp. 189-198. Copenhagen, Denmark: ASME.

Kaplan, P. (1992). Wave impact forces on offshore structures: re-examination and new interpretations. *24th Offshore Technology Conference* (pp. 79-98). Houston: Offshore Technology Conference.

Longuet-Higgins, M. S., & Stewart, R. W. (1964). Radiation streses in water waves: a physical discussion, with applications. *Deep-Sea Research , Vol. 11*, 529-561.

Mansard, E. P., & Funke, E. R. (1980). The Measurement of Incident and Reflected Spectra Using a Least Squares Method. *Proc. 17th Int. Conf. Coastal Eng.* (pp. 155-172). Sydney: ASCE.

McConnell, K., Allsop, W., & Cruickshank, I. (2004). *Pier, jetties and related structures exposed to waves: Guidelines for hydraulic loadings.* London: Thomas Telford Publishing.

NIST. (2006). *Performance of Physical Structures in Hurricane Katrina and Hurricane Rita: A Reconnaissance Report.* Gaithersburg, MD: National Institute of Standards and Technology.

OEA, Inc. (2005). *Hurricane Impact Analysis and Development of Design Criteria for the I-10 Bridges Over Escambia Bay.* Gainesville, FL: Ocean Engineering Associates, Inc.

Padgett, J., DesRoches, R., Nielson, B., Yashinsky, M., Kwon, O.-S., Burgette, N., et al. (2008). Bridge Damage and Repair Costs from Hurricane Katrina. *Journal of Bridge Engineering* , 6-14.

Robertson, I. N., Riggs, H. R., Yim, S. C., & Young, Y. L. (2007). Lessons from Hurricane Katrina Storm Surge on Bridges and Buildings. *Journal of Waterway, Port, Coastal, and Ocean Engineering , 133* (6), 463-483.

Shih, R. W., & Anastasiou, K. (1992). Wave Induced Uplift Pressures Acting on a Horizontal Platform. *ICE Proceedings, Water Maritime and Energy , 96* (1), 19-33.

APPENDIX A:

MATRIX OF REGULAR AND RANDOM WAVE CONDITIONS

Measured wave height and period for regular and random wave trials along with the corresponding prototype values. Conditions for regular wave trials are mean wave height, *H*, and mean wave period, *T*. Conditions for random wave trials are H_s and T_p. "U.S. 90 Bridge" represents H_s and T_p for conditions at the U.S. 90 Bridge over Biloxi Bay, MS, at the peak of Hurricane Katrina as estimated by Chen *et al*. (in press).

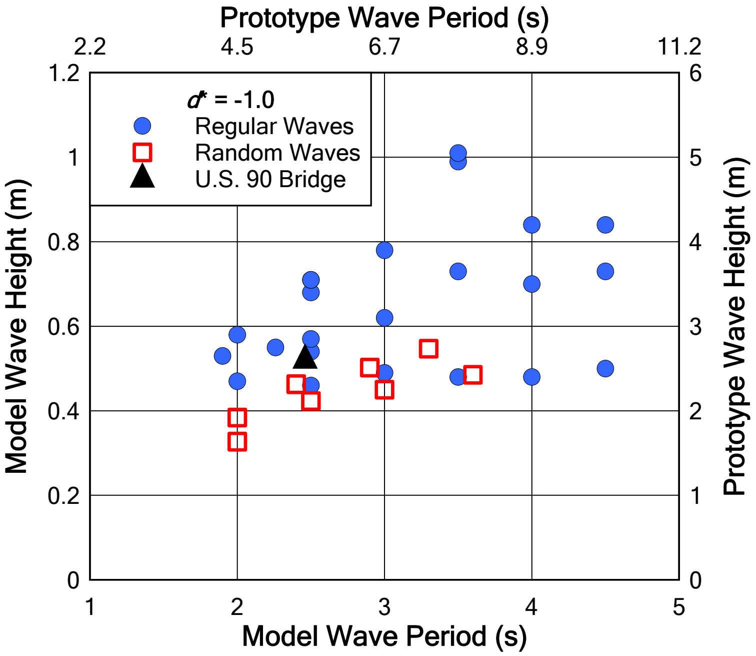

Figure A.1. Measured wave conditions for trials conducted at d* = -1.0.

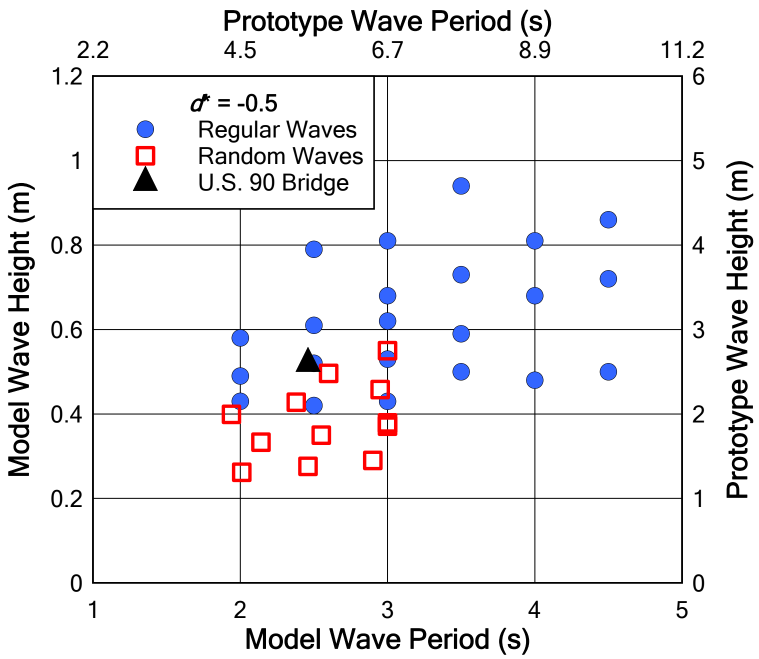

Figure A.2. Measured wave conditions for trials conducted at d* = -0.5.

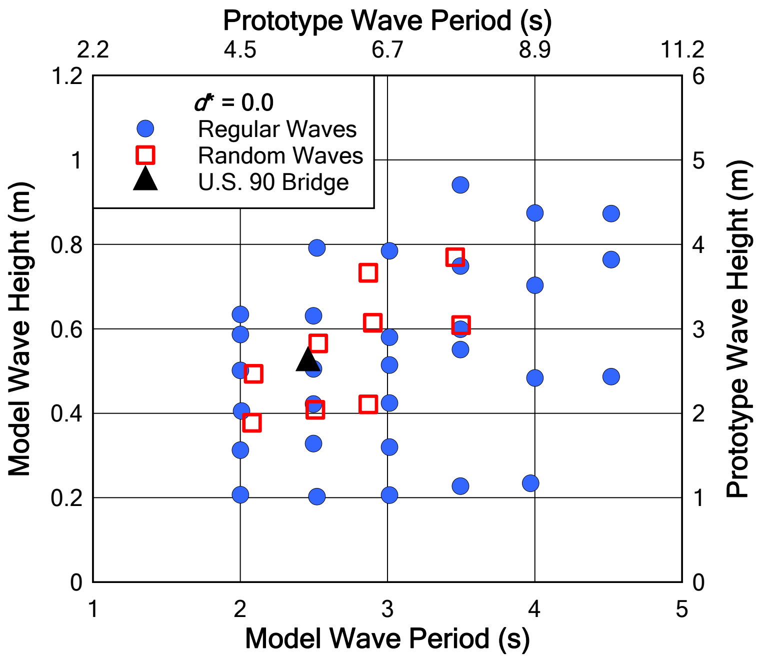

Figure A.3. Measured wave conditions for trials conducted at d* = 0.0.

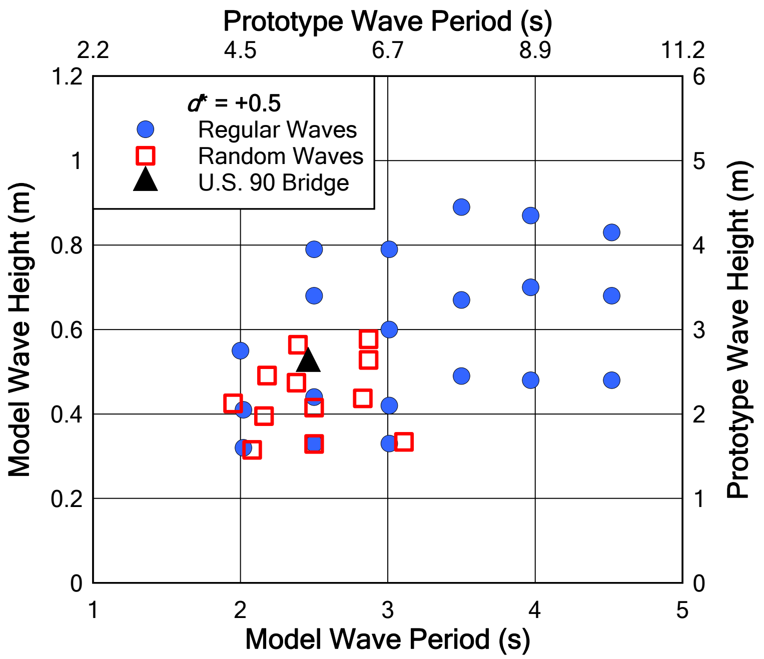

Figure A.4. Measured wave conditions for trials conducted at d* = +0.5.

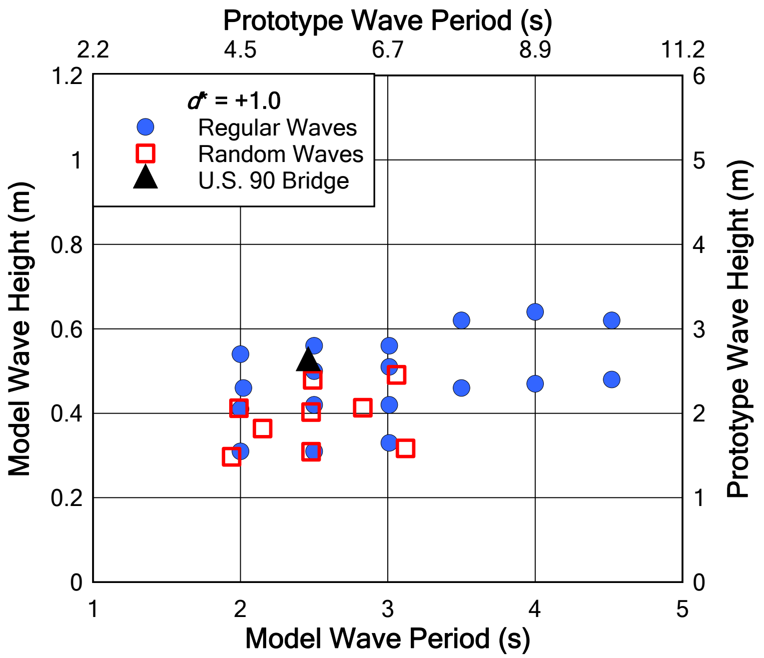

Figure A.5. Measured wave conditions for trials conducted at d* = +1.0.

APPENDIX B:

FORCE VS. WAVE HEIGHT FOR REGULAR WAVES

Plots of total measured horizontal (F_h) and vertical (F_v) forces vs. incident wave height, and their respective best-fit curves. Values for the regular wave trials are the mean of a series of consecutive waves and their corresponding forces in a single trial. The horizontal and vertical error bars on each marker represent the standard deviation of the collected wave heights and forces, respectively. The weight of the concrete test specimen is represented by the dotted line and reflects the effect of buoyancy at d^* = +0.5 and +1.0.

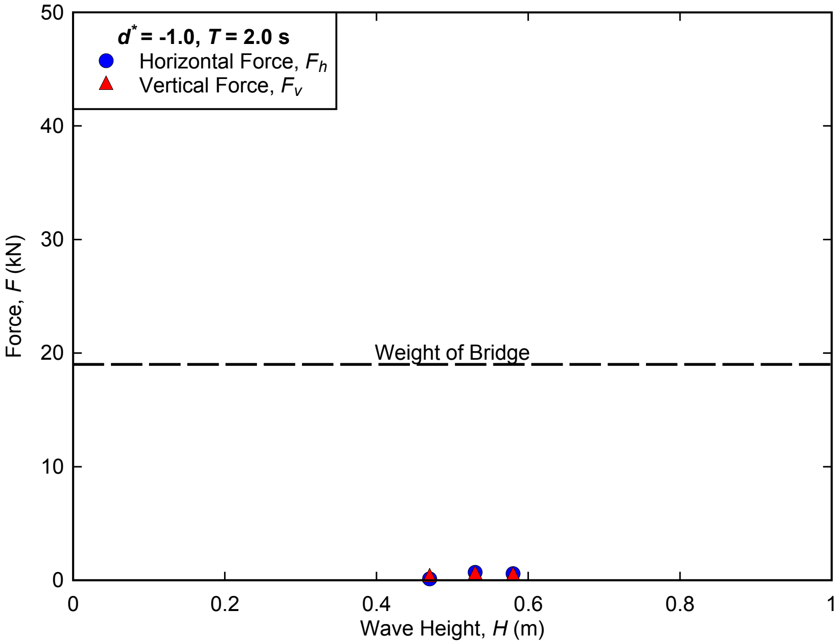

Figure B.6. Measured forces for regular wave trials conducted at d* = -1.0, T = 2.0 s.

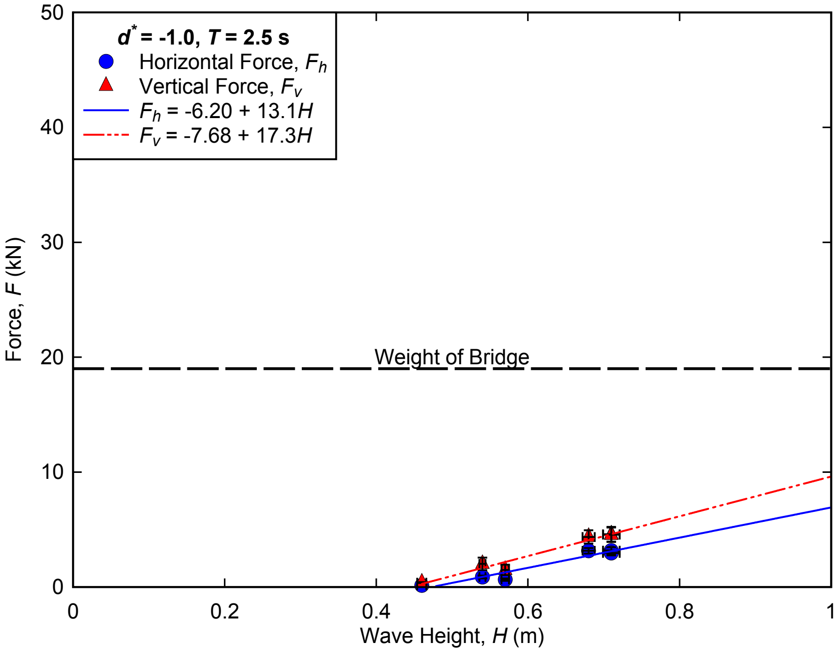

Figure B.7. Measured forces for regular wave trials conducted at d* = -1.0, T = 2.5 s.

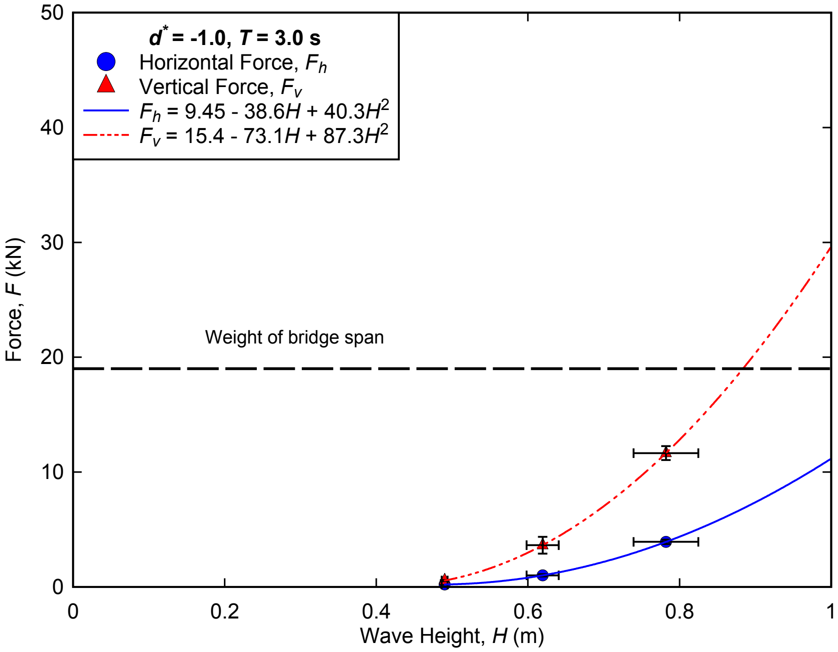

Figure B.8. Measured forces for regular wave trials conducted at d* = -1.0, T = 3.0 s.

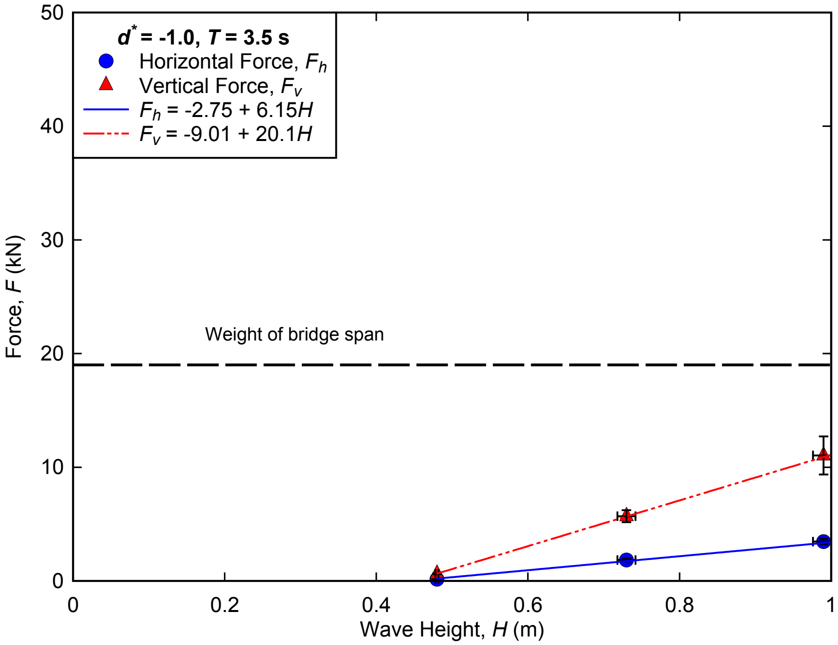

Figure B.9. Measured forces for regular wave trials conducted at d* = -1.0, T = 3.5 s.

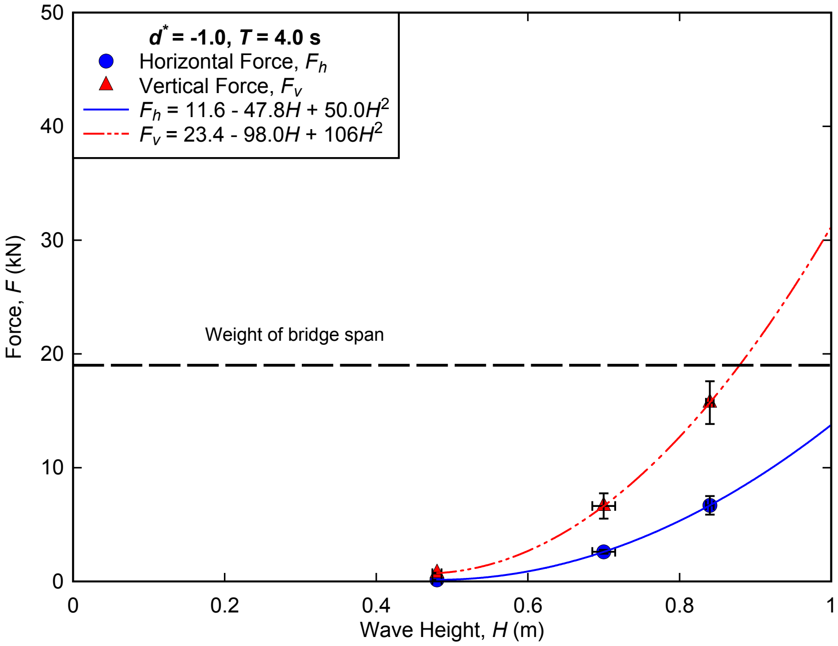

Figure B.10. Measured forces for regular wave trials conducted at d* = -1.0, T = 4.0 s.

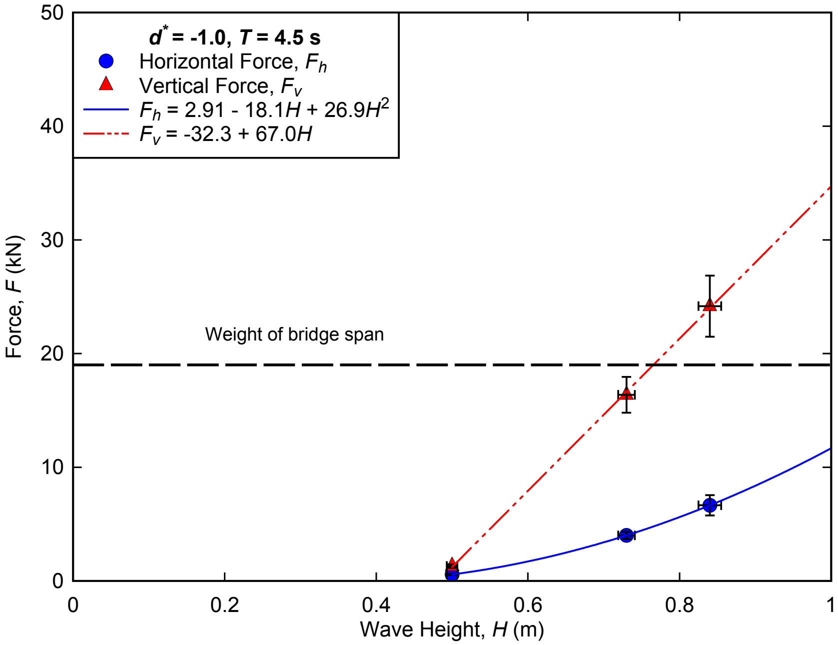

Figure B.11. Measured forces for regular wave trials conducted at d* = -1.0, T = 4.5 s.

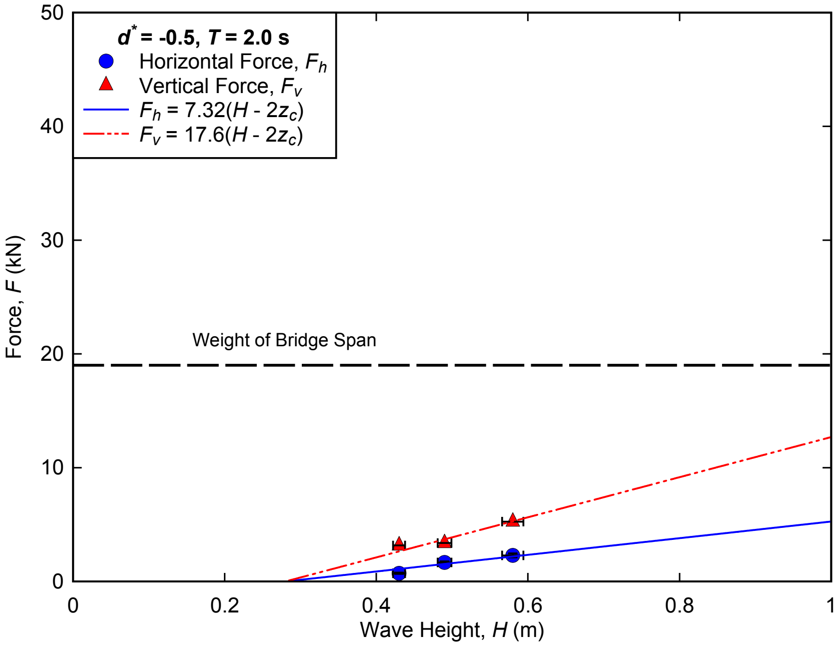

Figure B.12. Measured forces for regular wave trials conducted at d* = -0.5, T = 2.0 s.

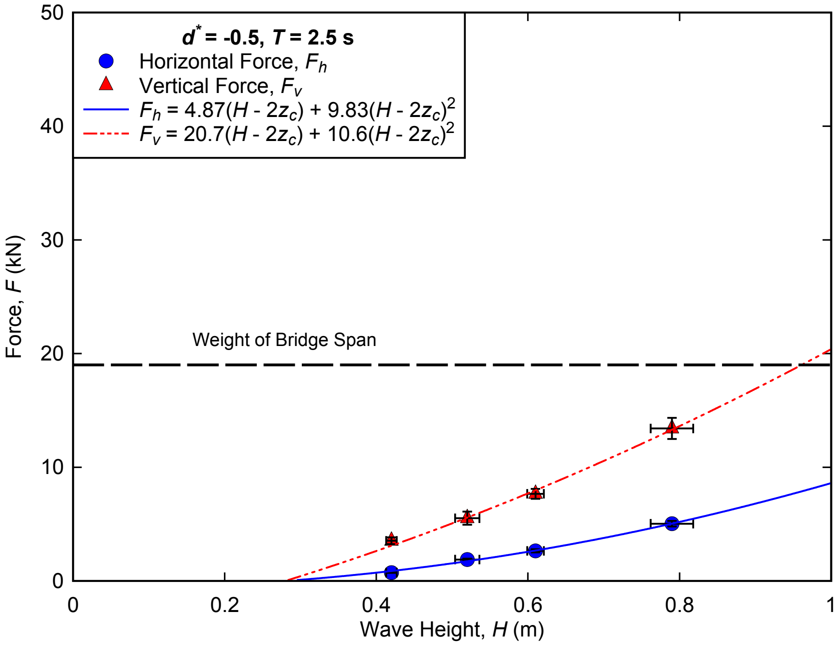

Figure B.13. Measured forces for regular wave trials conducted at d* = -0.5, T = 2.5 s.

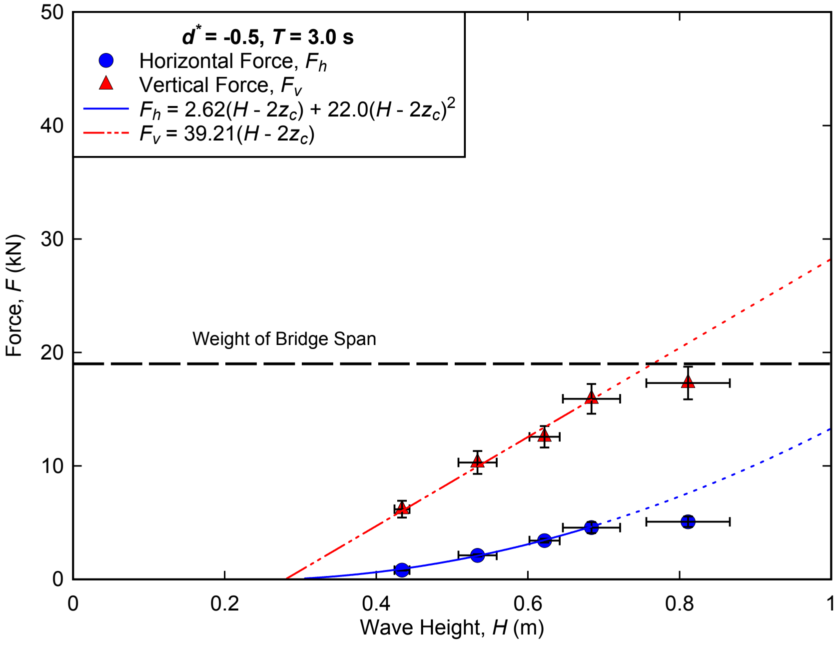

Figure B.14. Measured forces for regular wave trials conducted at d* = -0.5, T = 3.0 s.

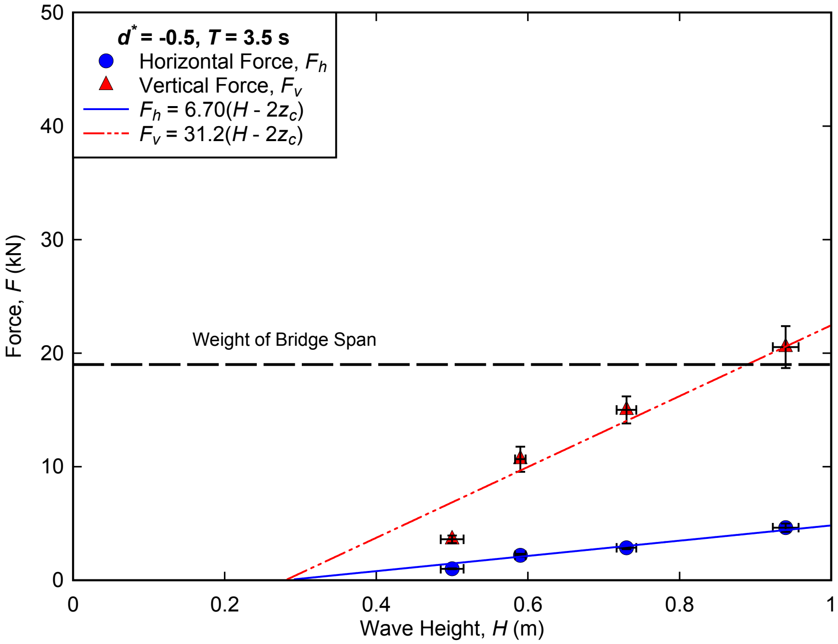

Figure B.15. Measured forces for regular wave trials conducted at d* = -0.5, T = 3.5s.

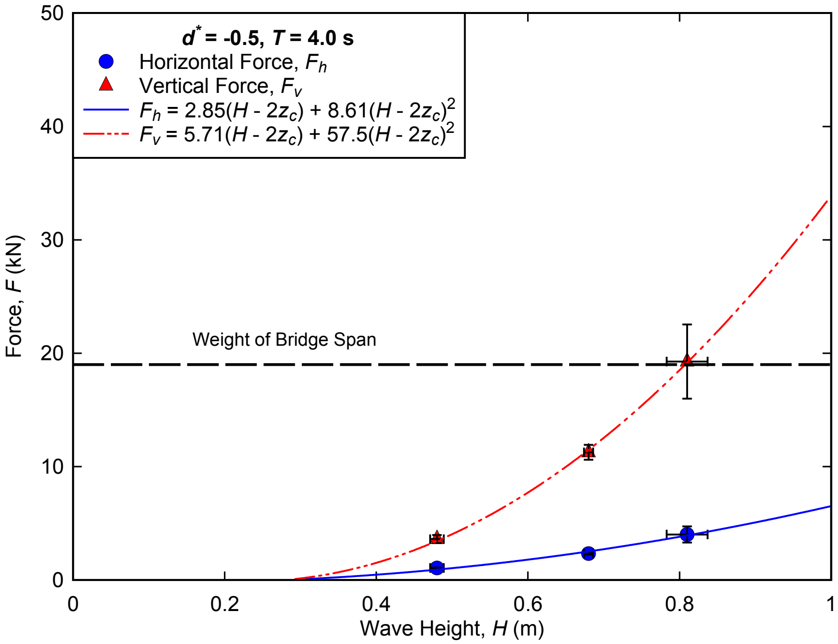

Figure B.16. Measured forces for regular wave trials conducted at d* = -0.5, T = 4.0s.

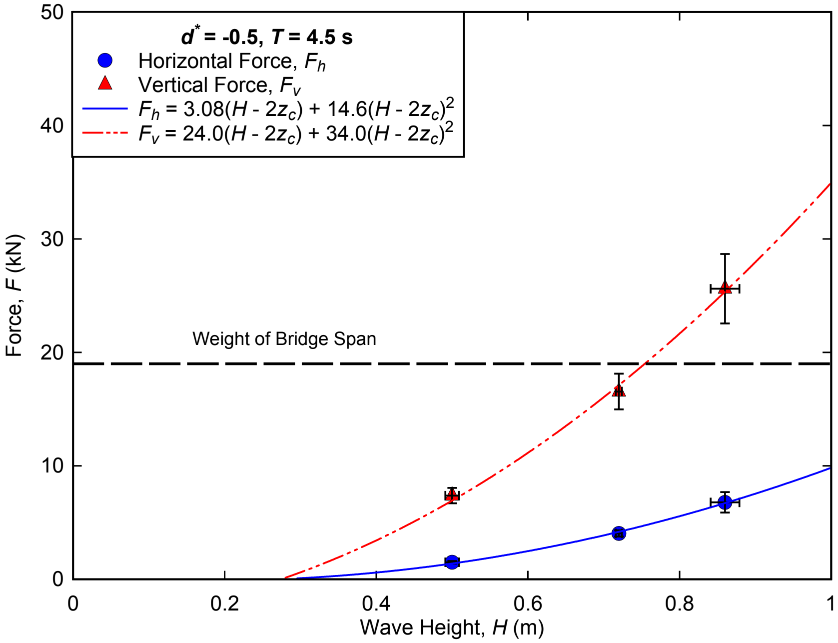

Figure B.17. Measured forces for regular wave trials conducted at d* = -0.5, T = 4.5s.

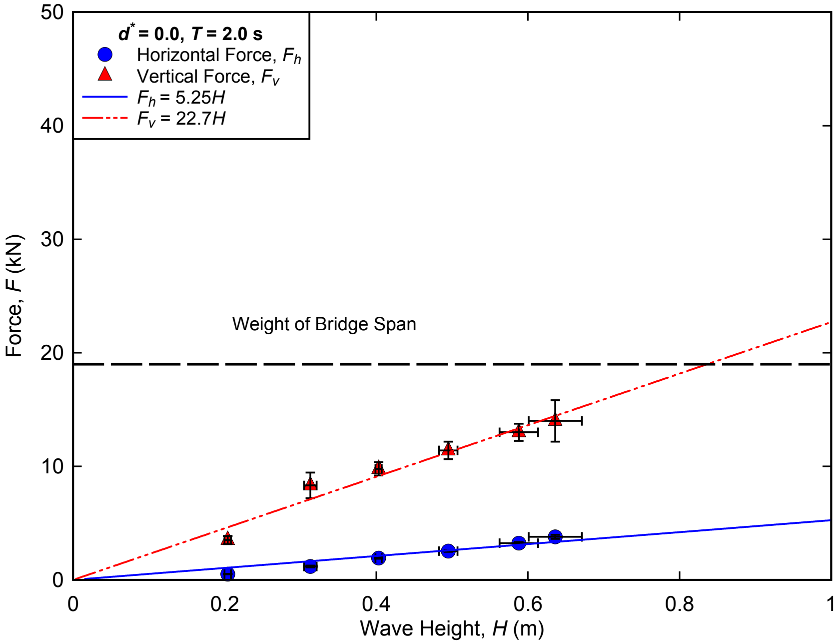

Figure B.18. Measured forces for regular wave trials conducted at d* = 0.0, T = 2.0 s.

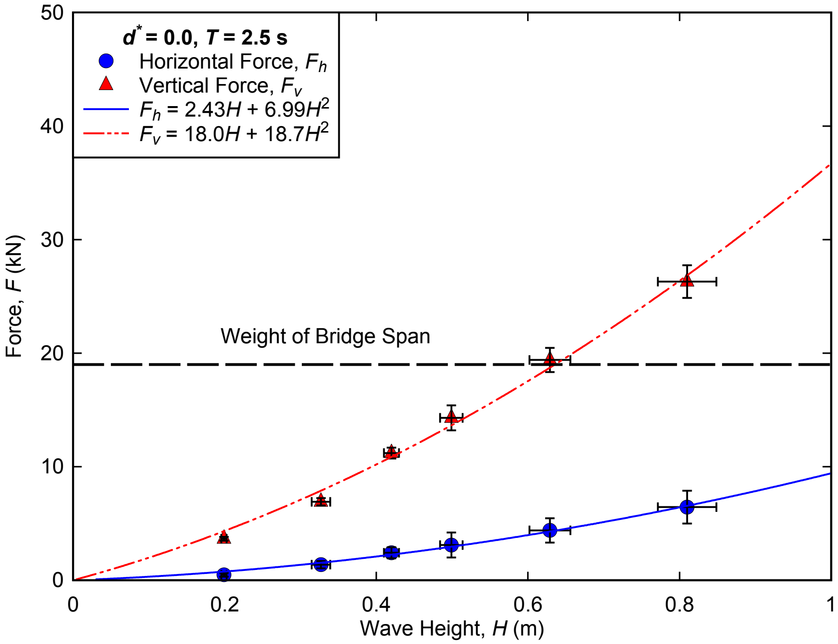

Figure B.19. Measured forces for regular wave trials conducted at d* = 0.0, T = 2.5 s.

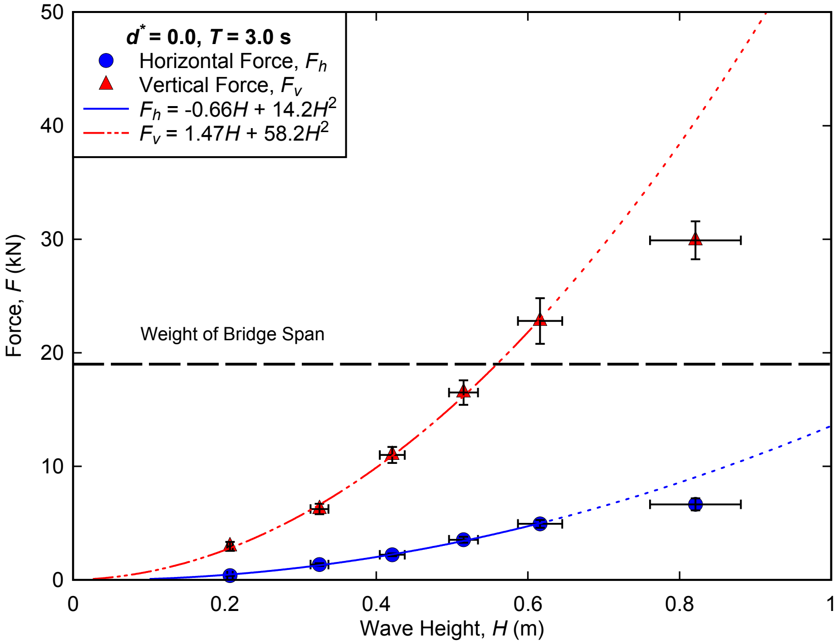

Figure B.20. Measured forces for regular wave trials conducted at d* = 0.0, T = 3.0 s.

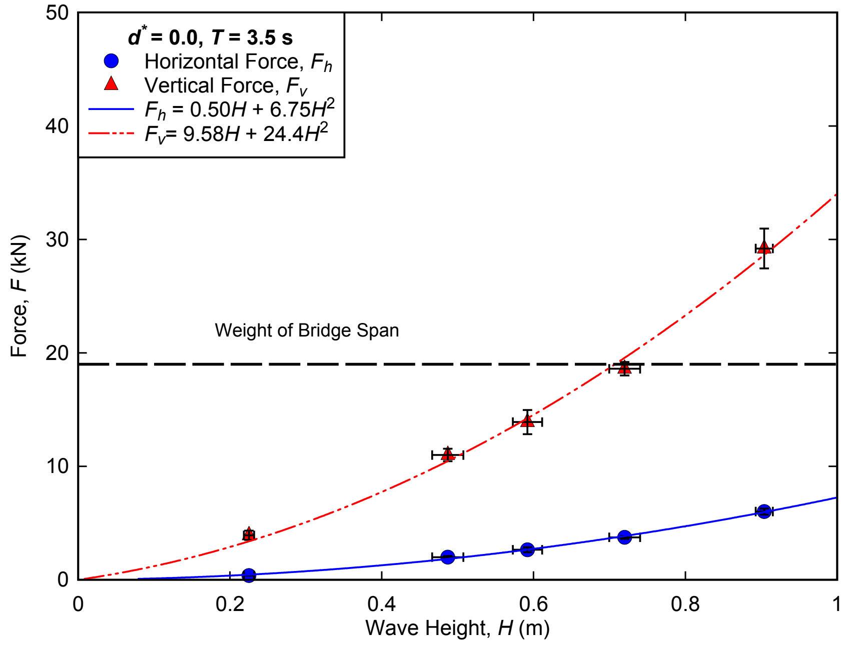

Figure B.21. Measured forces for regular wave trials conducted at d* = 0.0, T = 3.5 s.

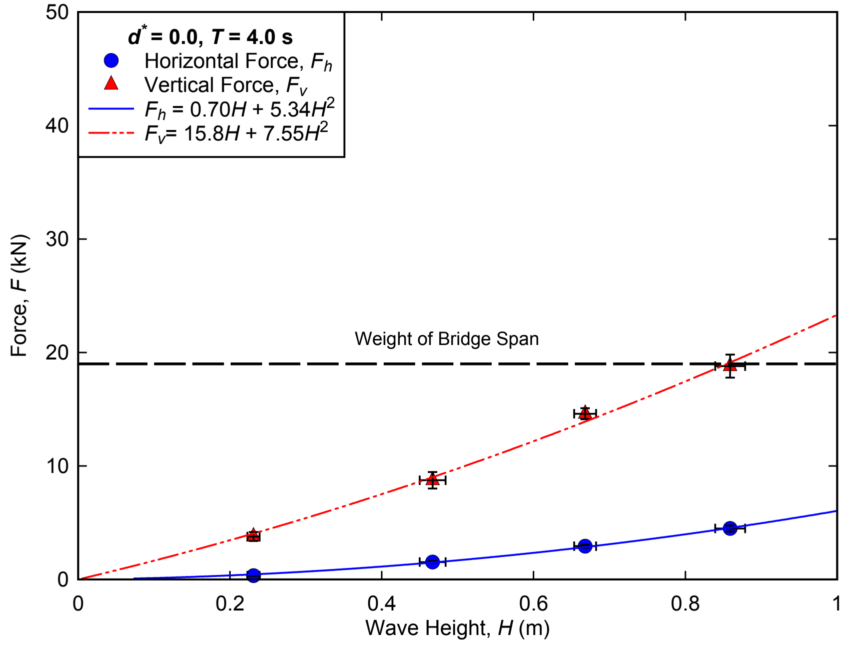

Figure B.22. Measured forces for regular wave trials conducted at d* = 0.0, T = 4.0 s.

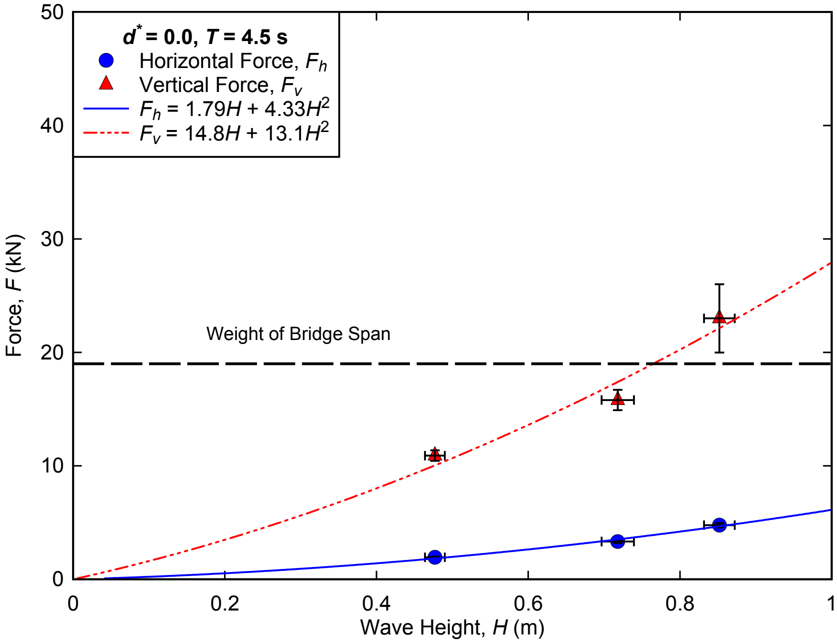

Figure B.23. Measured forces for regular wave trials conducted at d* = 0.0, T = 4.5 s.

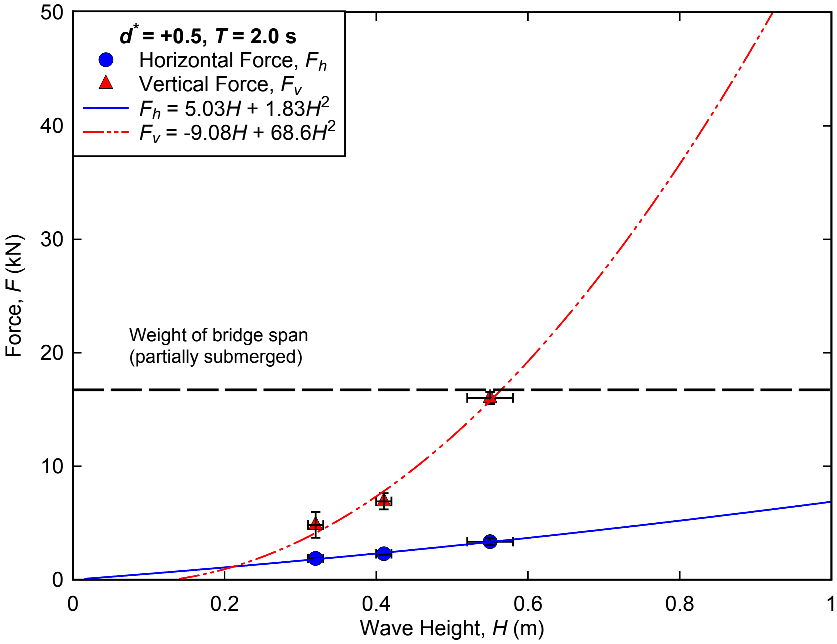

Figure B.24. Measured forces for regular wave trials conducted at d* = +0.5, T = 2.0s.

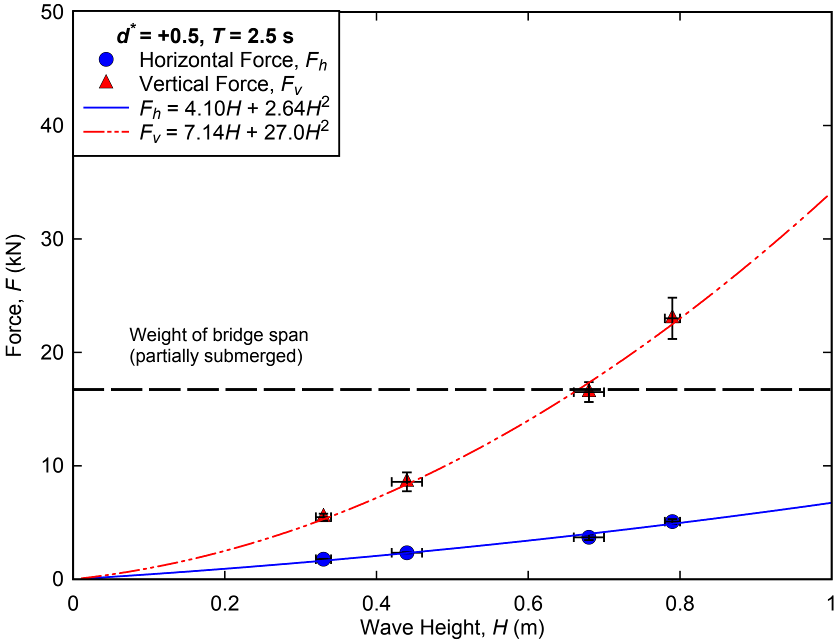

Figure B.25. Measured forces for regular wave trials conducted at d* = +0.5, T = 2.5s.

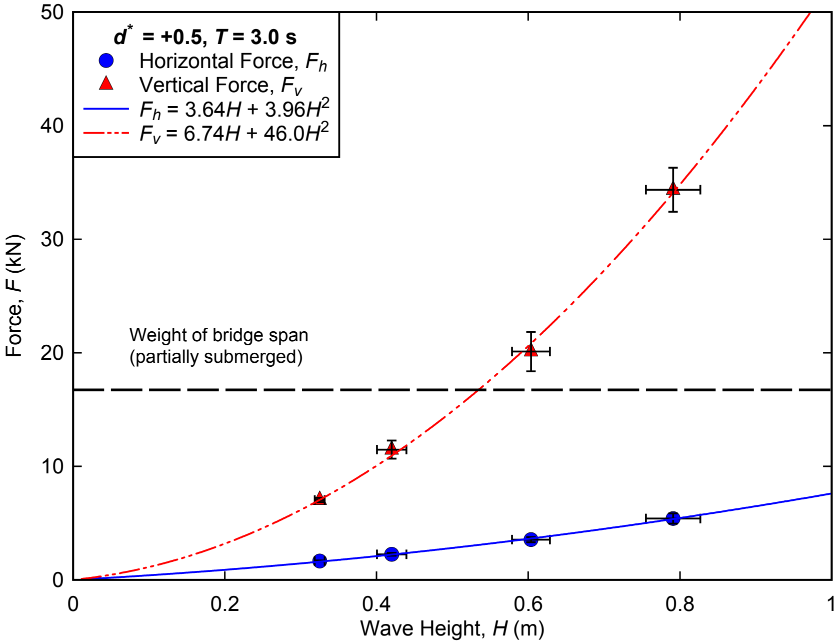

Figure B.26. Measured forces for regular wave trials conducted at d* = +0.5, T = 3.0s.

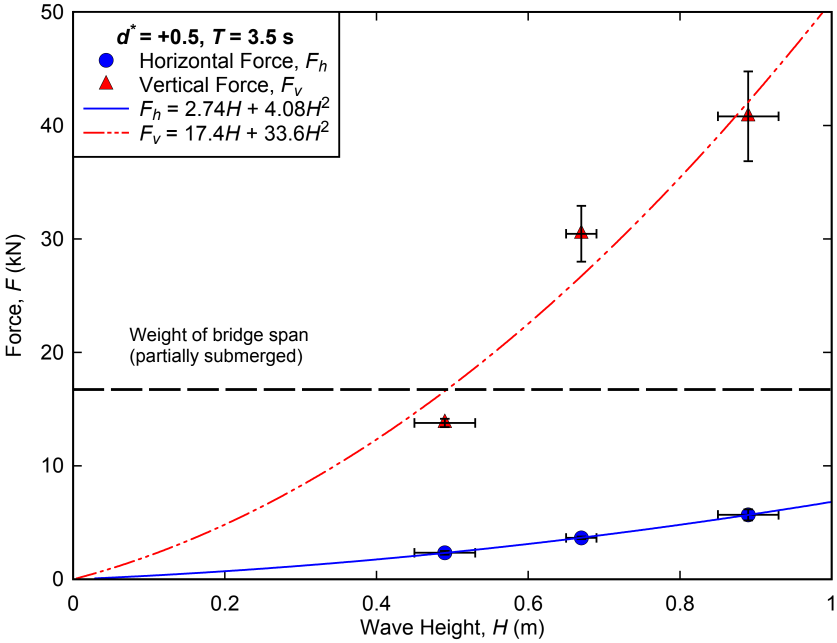

Figure B.27. Measured forces for regular wave trials conducted at d* = +0.5, T = 3.5s.

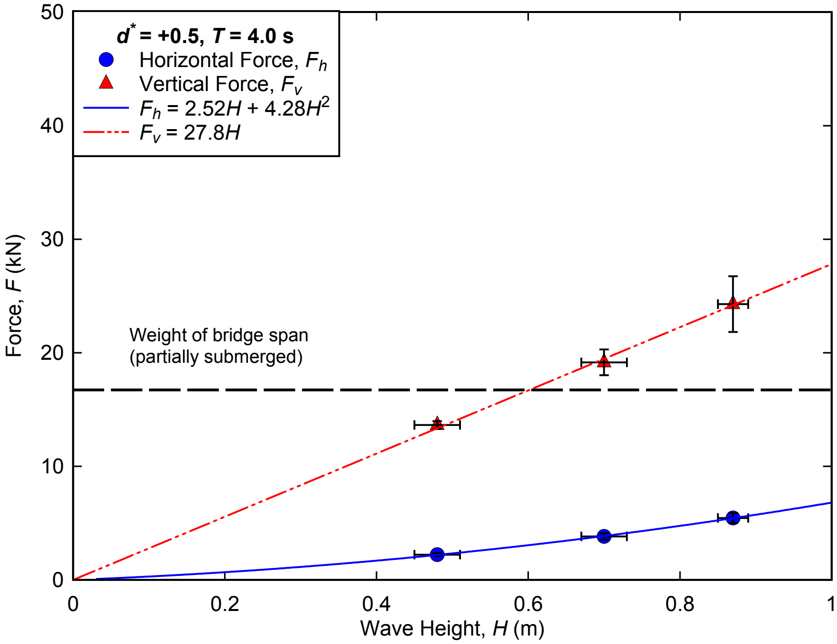

Figure B.28. Measured forces for regular wave trials conducted at d* = +0.5, T = 4.0s.

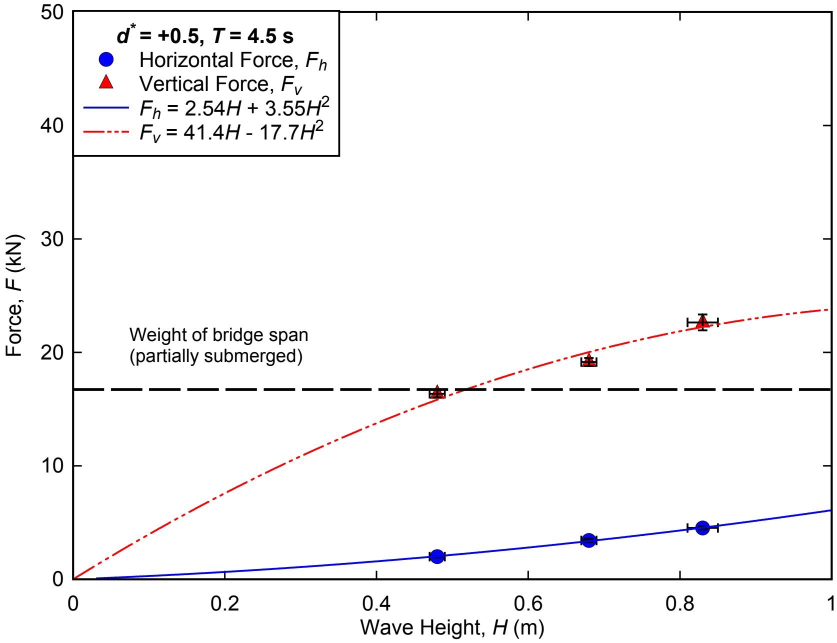

Figure B.29. Measured forces for regular wave trials conducted at d* = +0.5, T = 4.5s.

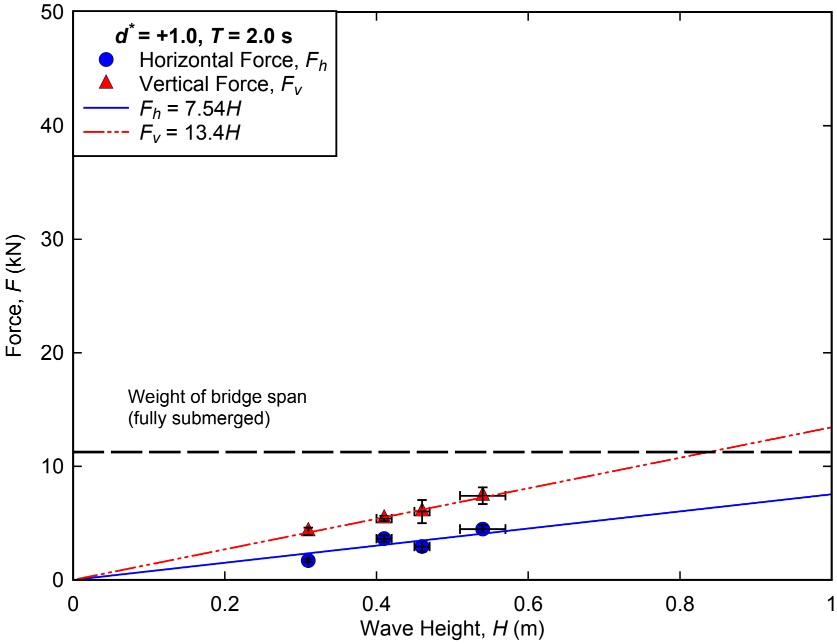

Figure B.30. Measured forces for regular wave trials conducted at d* = +1.0, T = 2.0s.

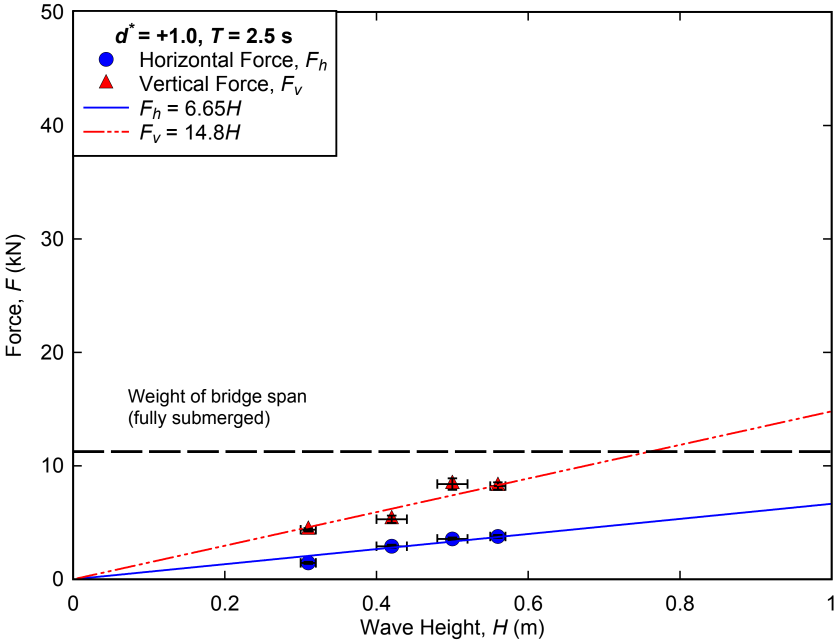

Figure B.31. Measured forces for regular wave trials conducted at d* = +1.0, T = 2.5s.

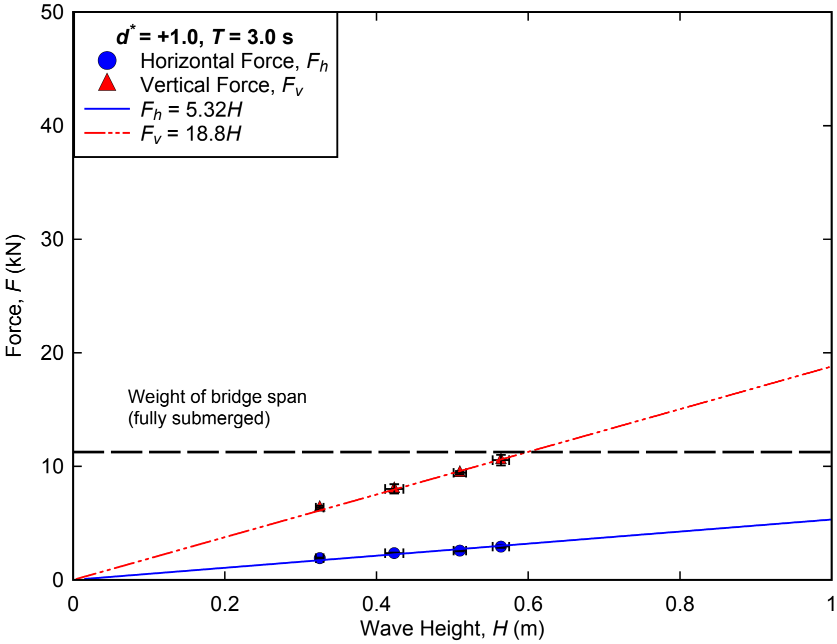

Figure B.32. Measured forces for regular wave trials conducted at d* = +1.0, T = 3.0s.

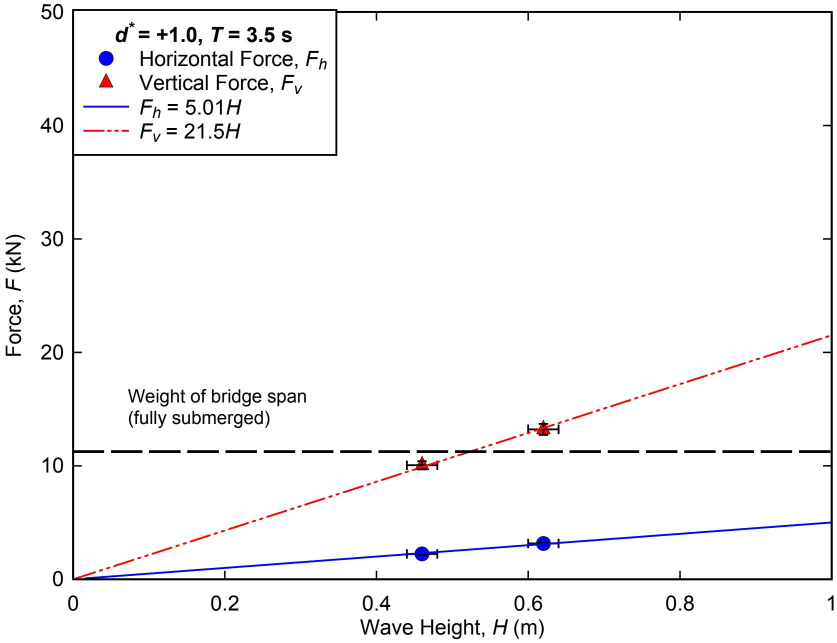

Figure B.33. Measured forces for regular wave trials conducted at d* = +1.0, T = 3.5s.

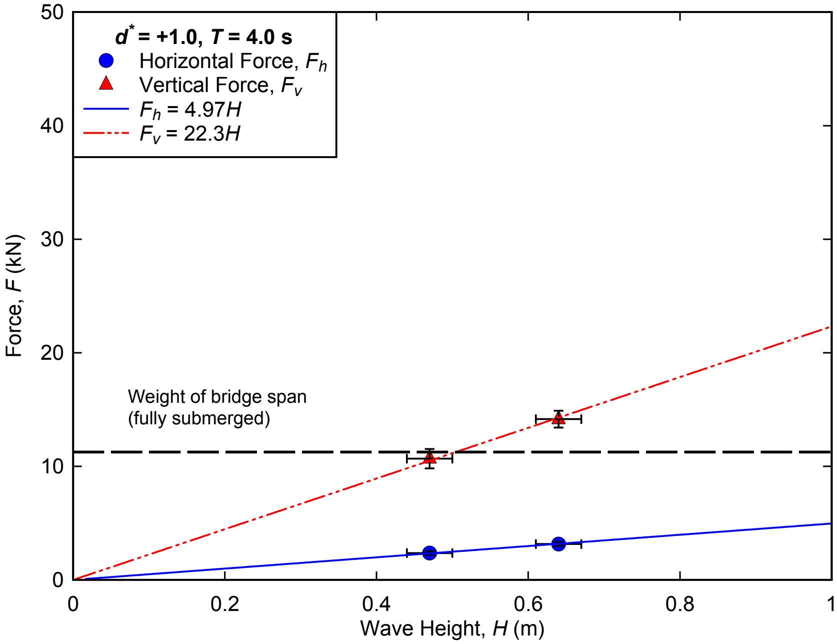

Figure B.34. Measured forces for regular wave trials conducted at d* = +1.0, T = 4.0s.

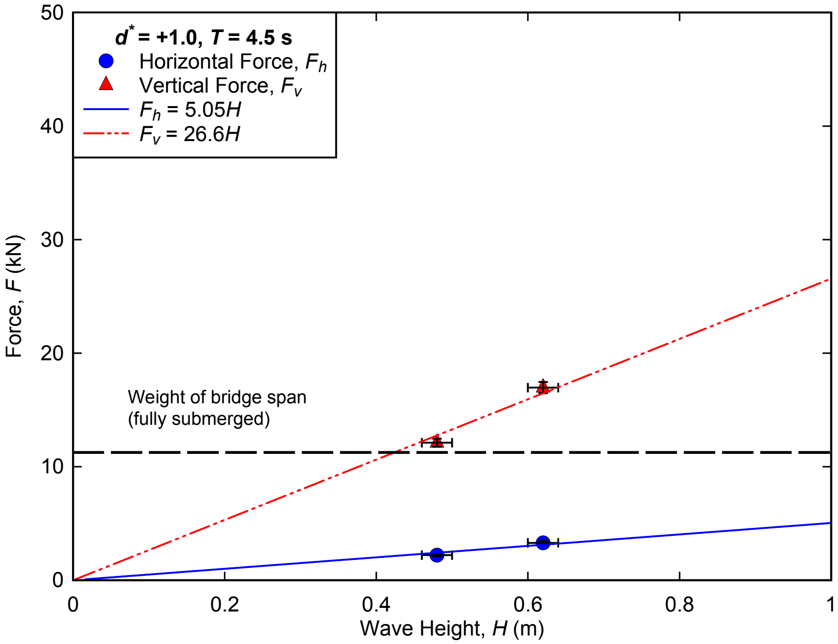

Figure B.35. Measured forces for regular wave trials conducted at d* = +1.0, T = 4.5s.

APPENDIX C:

EFFECT OF WATER LEVEL ON FORCES FOR REGULAR WAVES

Using the best-fit curves from the measured data, horizontal and vertical forces are calculated for a regular wave height, $H = 0.6$ m at each value of d^*. The weight of the bridge span (accounting for buoyancy) is represented by the dashed line and should be read using the vertical force scale.

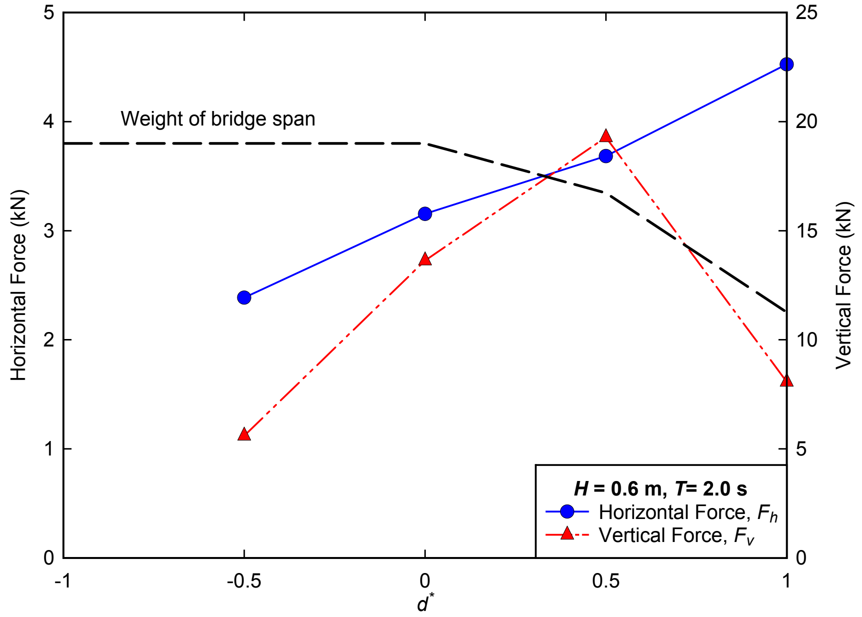

Figure C.1. Calculated force vs. water level for T = 2.0 s.

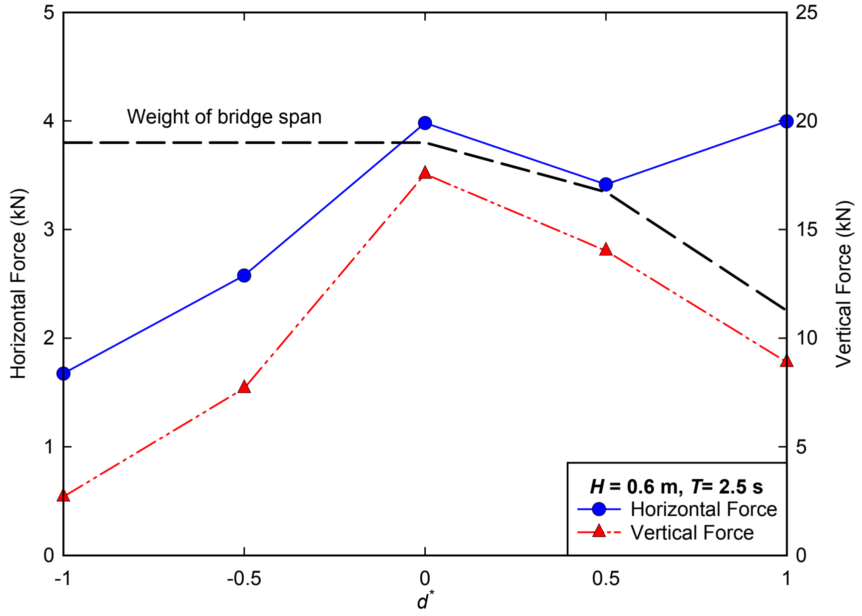

Figure C.2. Calculated force vs. water level for T = 2.5 s.

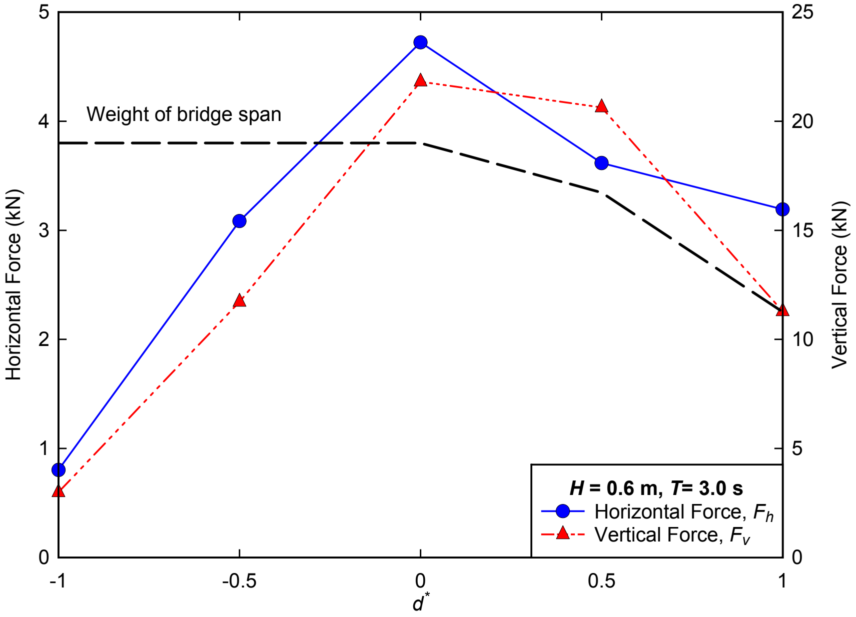

Figure C.3. Calculated force vs. water level for T = 3.0 s.

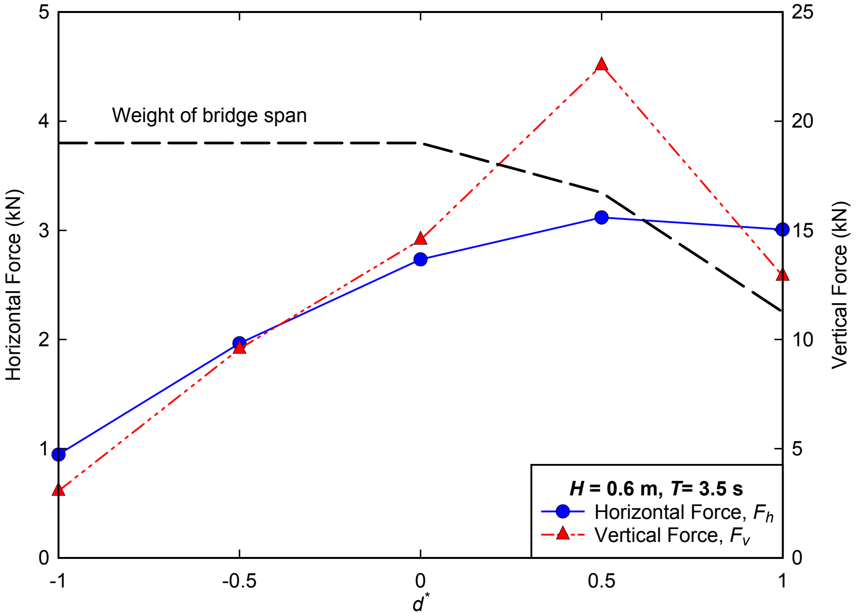

Figure C.4. Calculated force vs. water level for T = 3.5 s.

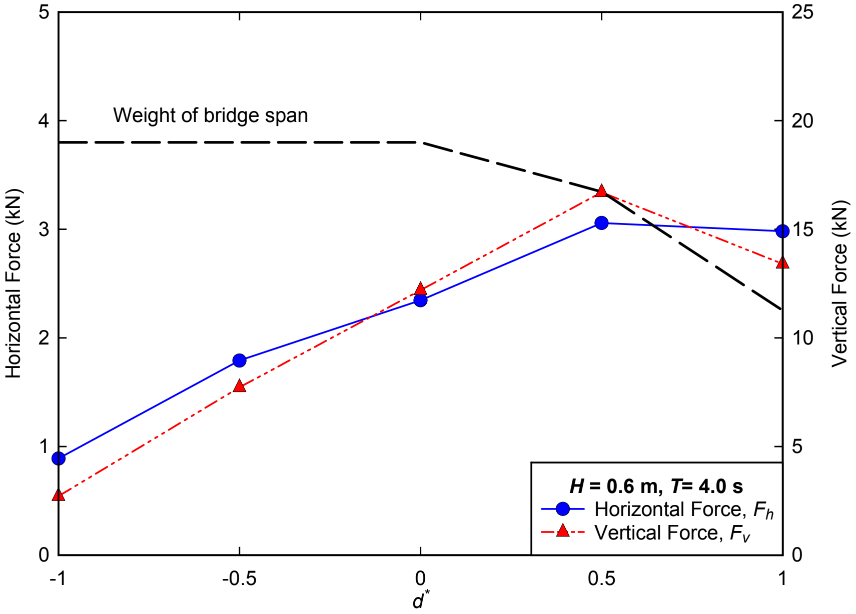

Figure C.5. Calculated force vs. water level for T = 4.0 s.

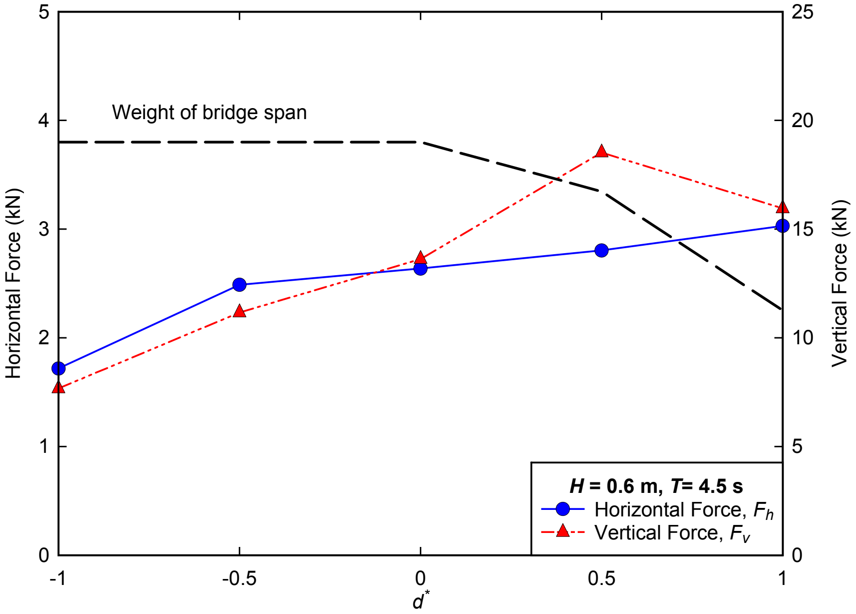

Figure C.6. Calculated force vs. water level for T = 4.5 s.

APPENDIX D:

MINIMUM REGULAR WAVE HEIGHT REQUIRED TO OVERCOME WEIGHT OF BRIDGE SUPERSTRUCTURE

Using the best-fit curves calculated from the measured data, the minimum regular wave height required to produce a vertical force that will exceed the net weight of the bridge (accounting for buoyancy) is predicted for a full range of conditions. Solid markers and lines indicate that the values are interpolated using the best-fit curve. Hollow markers and dotted lines indicate the data are calculated through extrapolation of the measured data and are not reliable. The red dashed line indicates the theoretical wave height limit due to wave steepness according to the Miche criteria. Cases where the extrapolated data approach or exceed the wave-height limit are likely not possible, but are shown to demonstrate the effect of water level on the net vertical forces experienced by the superstructure.

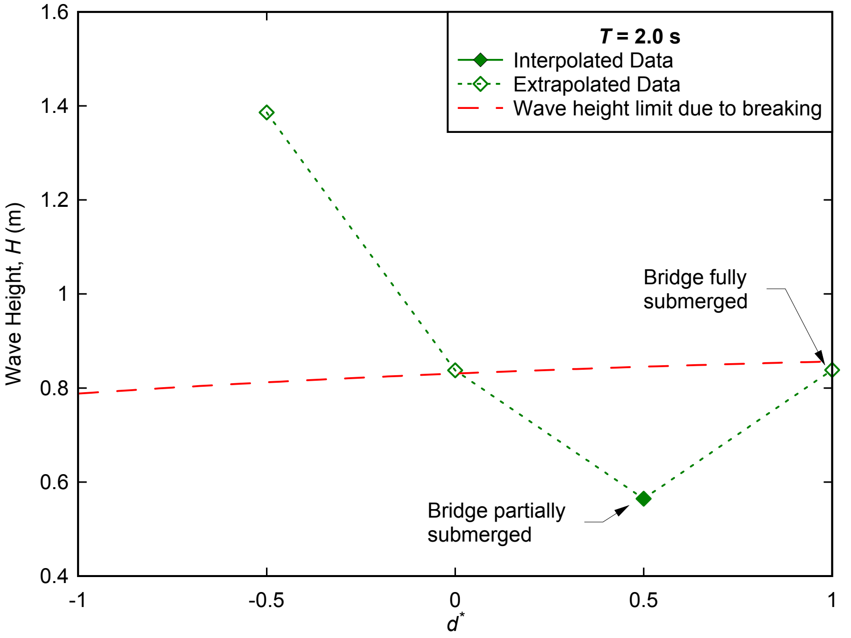

Figure D.1. Minimum wave height to overcome weight of superstructure, T = 2.0 s.

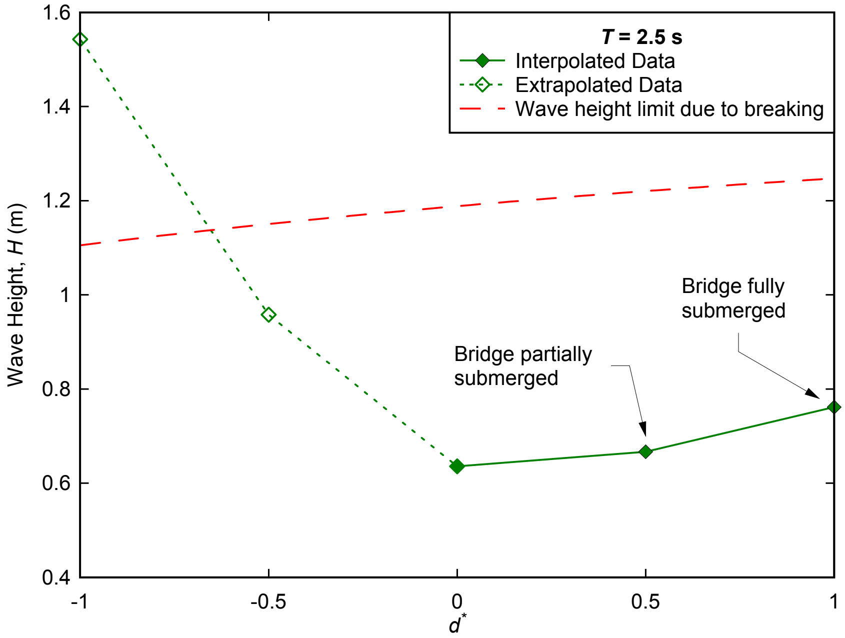

Figure D.2. Minimum wave height to overcome weight of superstructure, T = 2.5 s.

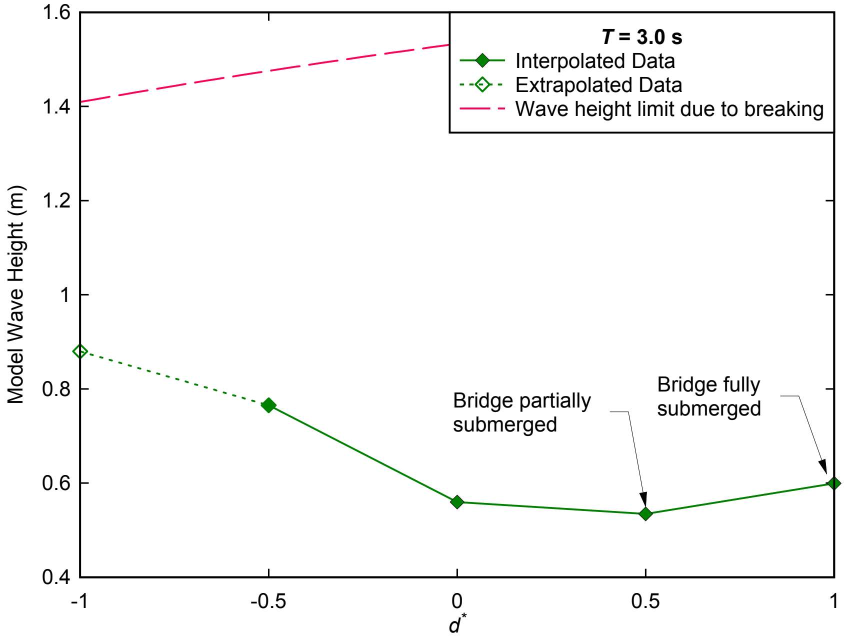

Figure D.3. Minimum wave height to overcome weight of superstructure, T = 3.0 s.

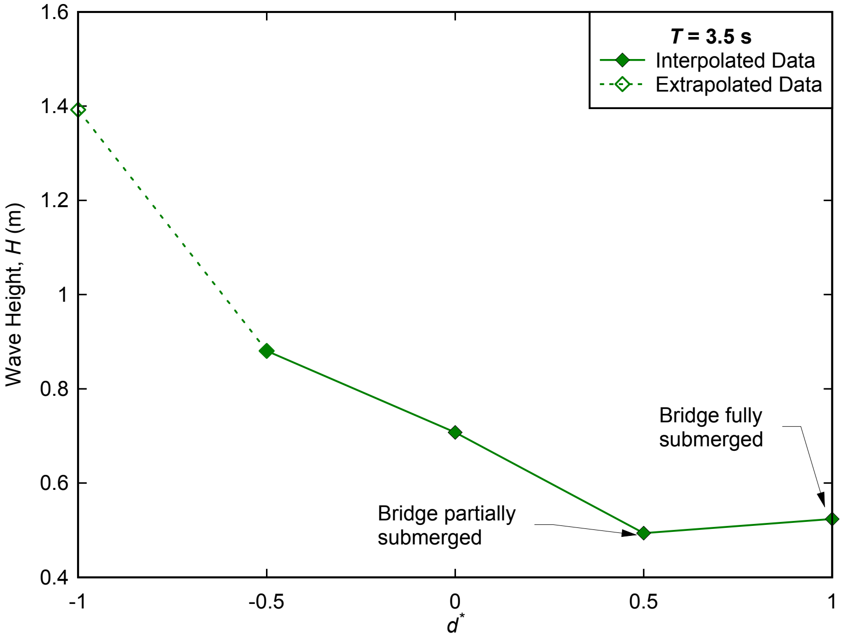

Figure D.4. Minimum wave height to overcome weight of superstructure, T = 3.0 s.

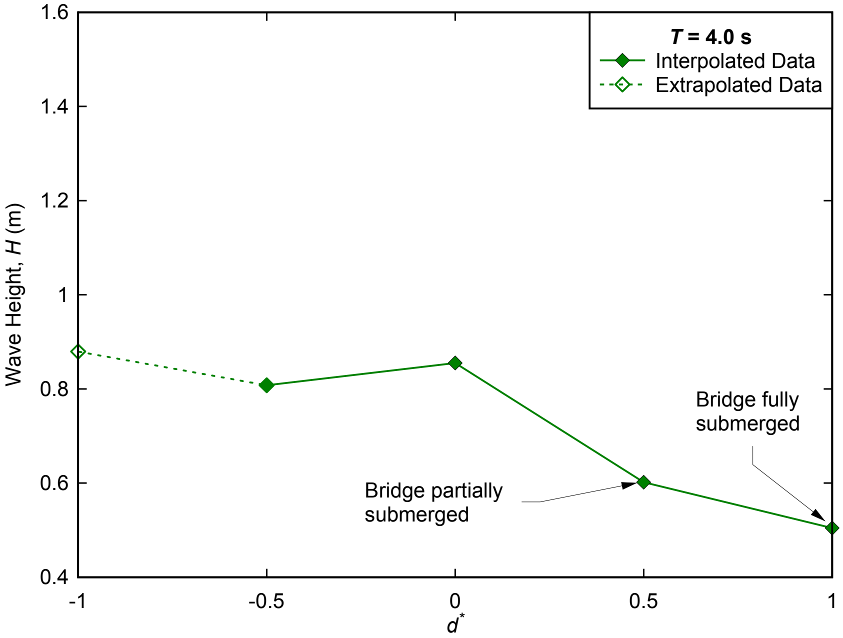

Figure D.5. Minimum wave height to overcome weight of superstructure, T = 4.0 s.

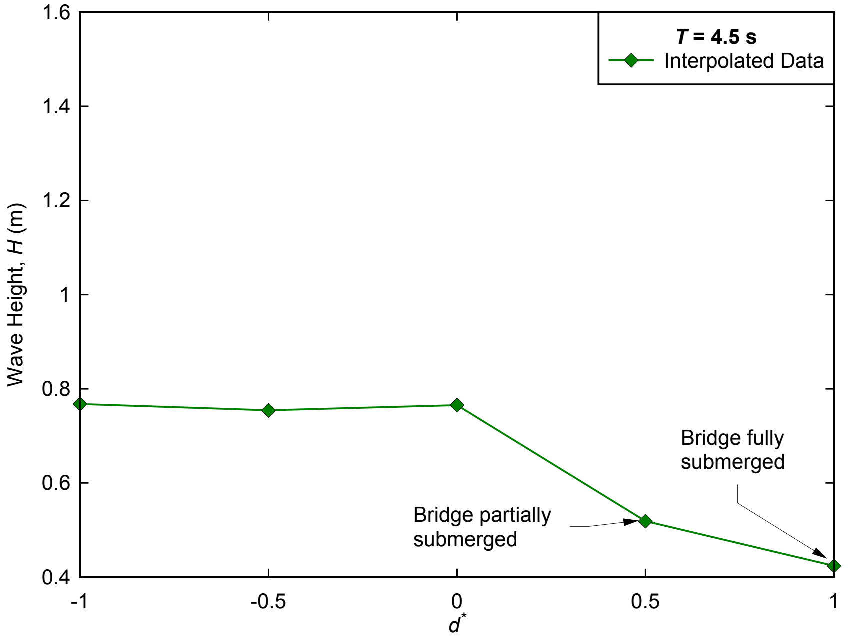

Figure D.6. Minimum wave height to overcome weight of superstructure, T = 4.5 s.

APPENDIX E:

EFFECT OF WAVE PERIOD ON FORCES FOR REGULAR WAVES

The graphs below demonstrate the effect of wave period on horizontal and vertical forces for regular waves. Using the best-fit curves calculated from the measured data, forces are calculated for a wave height of 0.6 meters at each wave period. Although not directly related to regular wave periods, the estimated peak period (scaled) at the U.S. 90 Bridge over Biloxi Bay, MS, during Hurricane Katrina is given as a reference to conditions during extreme events found in the shallow estuaries and bays where coastal bridges are typically located.

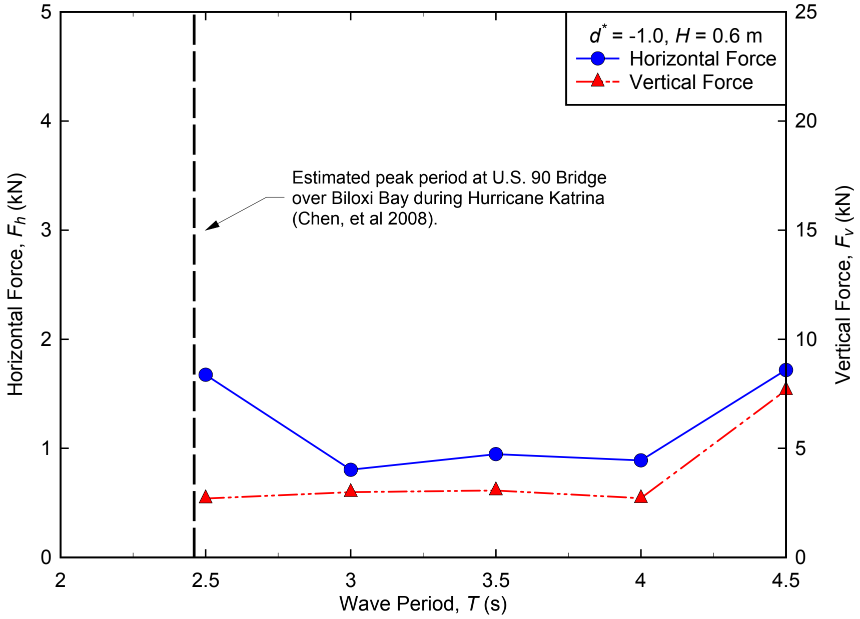

Figure E.7. Effect of wave period on forces for regular waves, d* = -1.0.

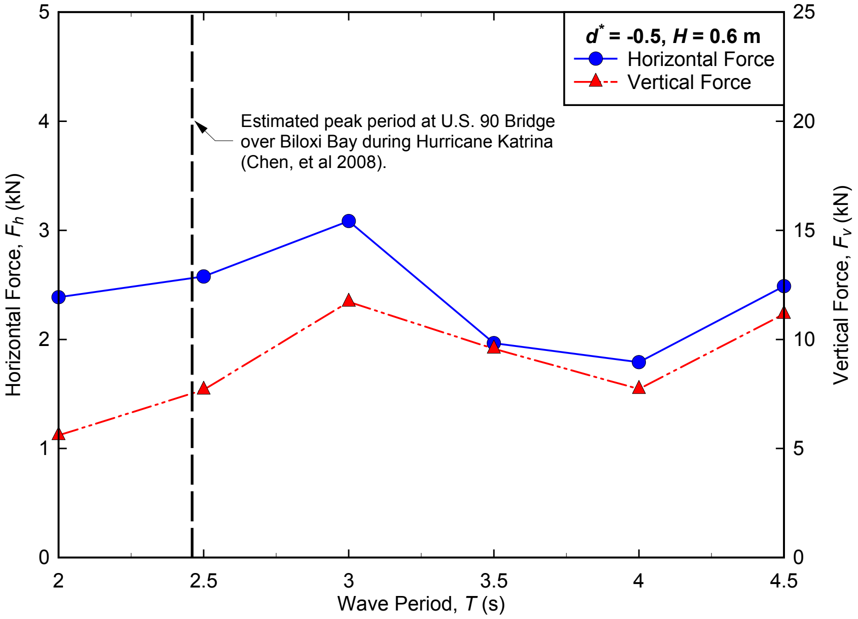

Figure E.8. Effect of wave period on forces for regular waves, d* = -0.5.

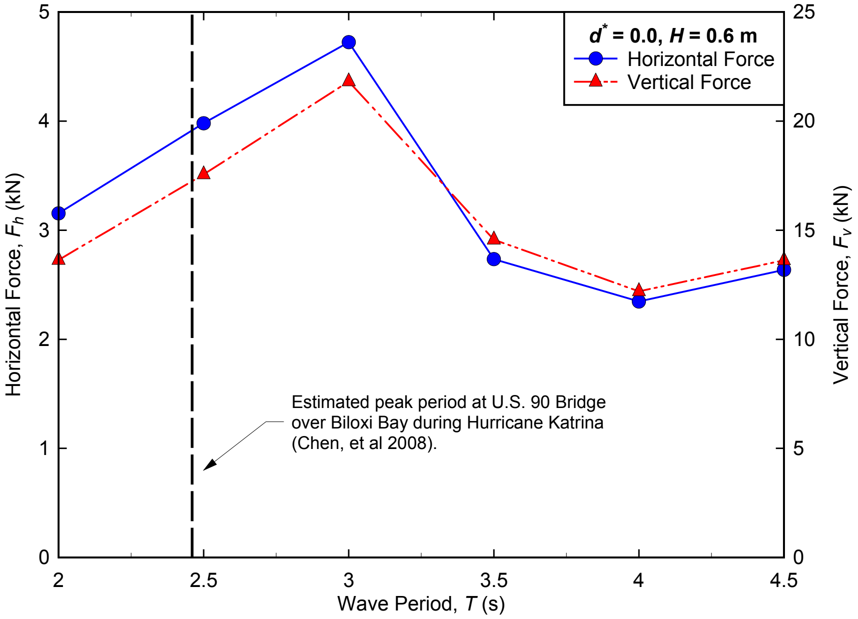

Figure E.9. Effect of wave period on forces for regular waves, d* = 0.0.

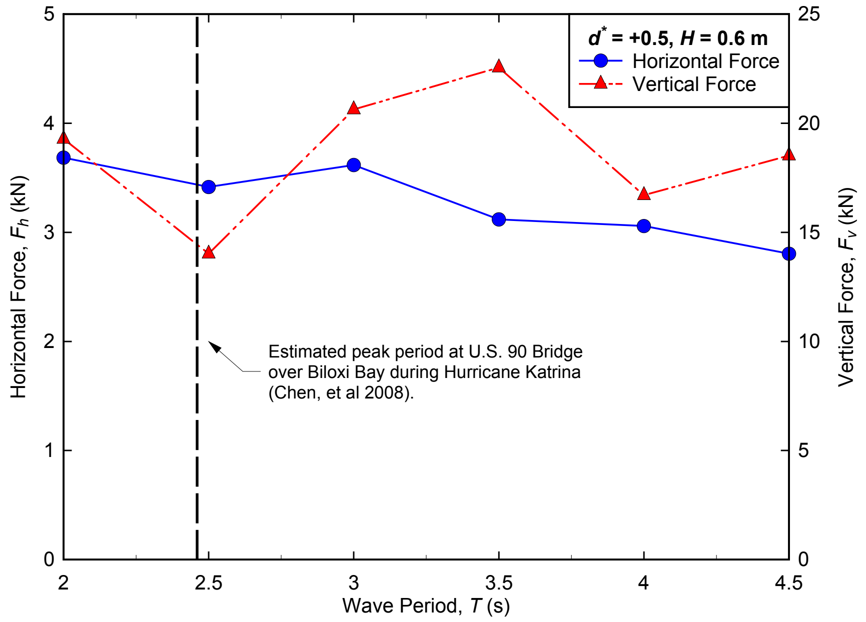

Figure E.10. Effect of wave period on forces for regular waves, d* = +0.5.

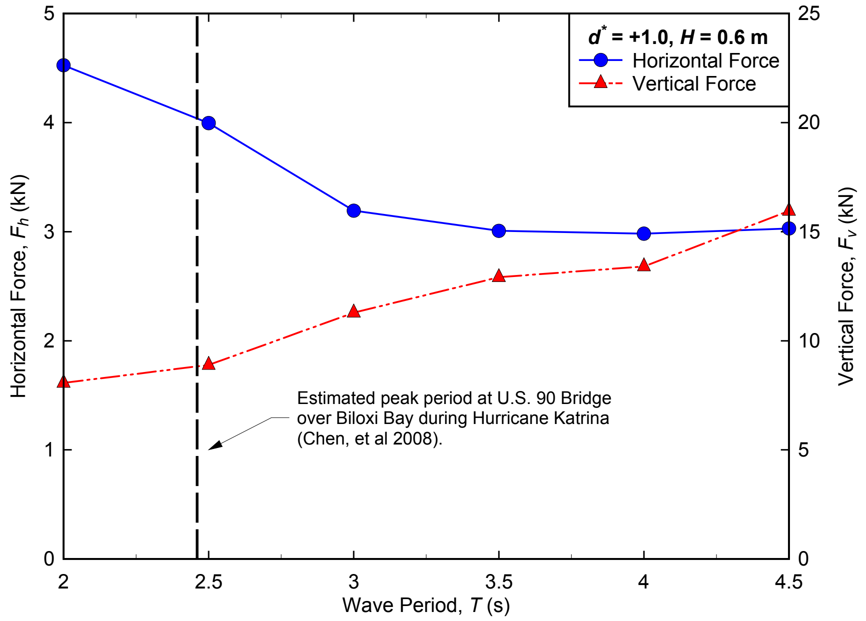

Figure E.11. Effect of wave period on forces for regular waves, d* = +1.0.

APPENDIX F:

FORCE VS. WAVE HEIGHT FOR RANDOM WAVES

From random wave trials consisting of approximately 300 waves, significant wave height, H_s, and the corresponding average of the highest one-third of the measured forces, $F_{1/3}$, are presented below. Note that for d^* = -1.0 and -0.5, the sample used to calculated $F_{1/3}$ may be significantly smaller compared to the others, as only the highest waves for trials at these depths struck the bridge superstructure. A curve was fitted to the horizontal and vertical data, except for trials at d^* = -1.0, where the range of the data was not sufficient to provide a reliable curve. For d^* = -0.5, the curve was forced through 0.17, 0 (H_s, $F_{1/3}$) as H_s = 0.17 m was calculated as the minimum condition that would produce a wave large enough to strike the bridge superstructure, assuming a Rayleigh distribution of wave heights and a sample size of 300 waves. For all other water levels, the curve was forced through the origin. H_s (scaled) for the U.S. 90 Bridge over Biloxi Bay during Hurricane Katrina, as estimated by Chen *et al*., (in press) is presented along with the weight of the bridge superstructure used in the experiment (accounting for buoyancy).

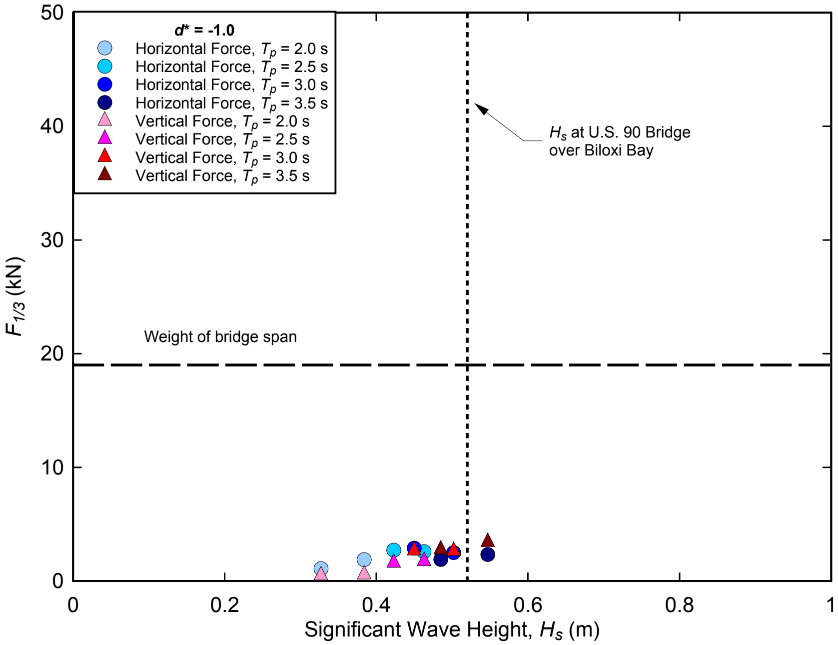

Figure F.12. Force vs. wave height for random wave trials, d* = -1.0.

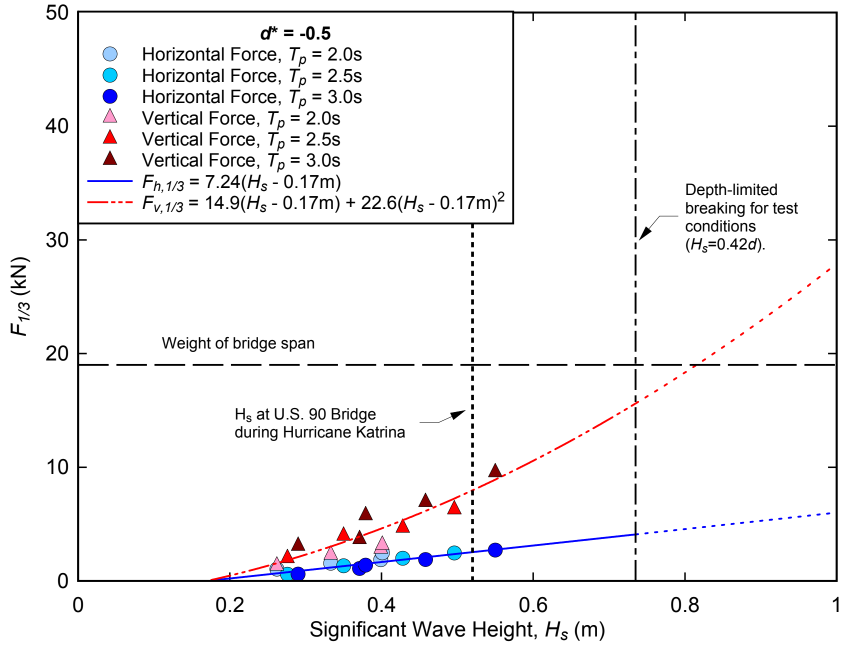

Figure F.13. Force vs. wave height for random wave trials, d* = -0.5.

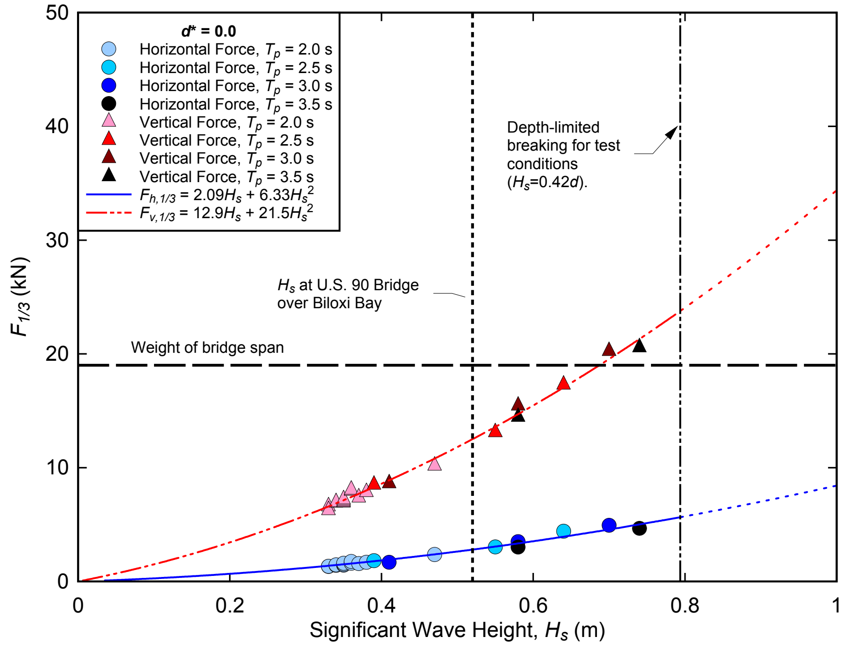

Figure F.14. Force vs. wave height for random wave trials, d* = 0.0.

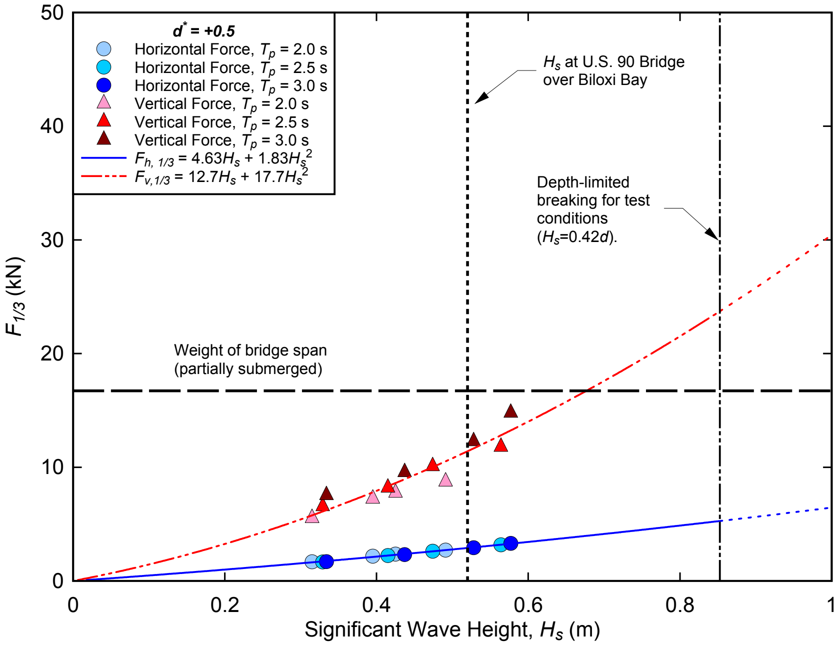

Figure F.15. Force vs. wave height for random wave trials, d* = +0.5.

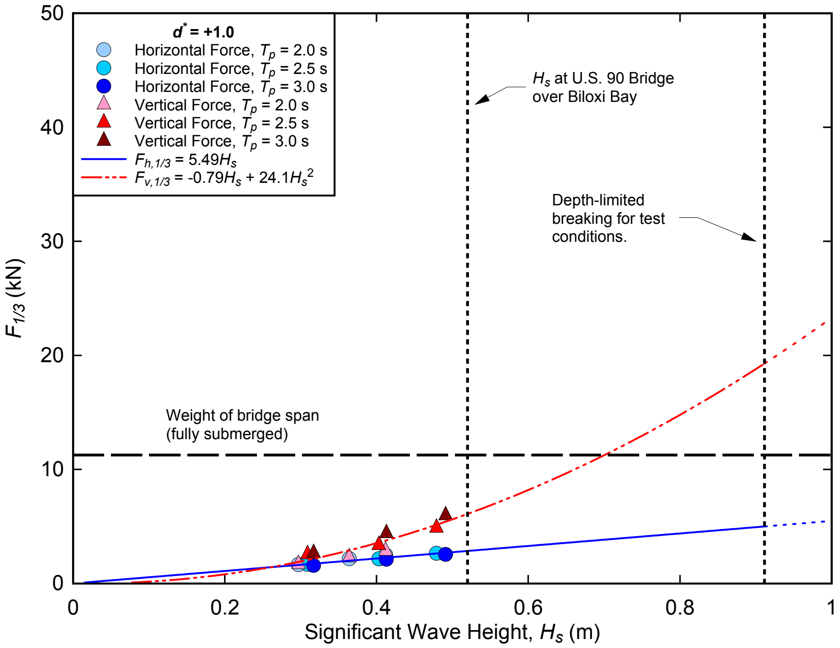

Figure F.16. Force vs. wave height for random wave trials, d* = +1.0.

APPENDIX G:
COMPARISON OF AASHTO GUIDELINES TO MEASURED DATA

Recently published AASHTO guidelines for coastal bridges vulnerable to storms provide a series of equations to estimate maximum quasi-steady and "slamming" forces due to wave impact. Because the equations require prototype-scale input parameters, the resulting forces were reduced to model scale using Froude criteria.

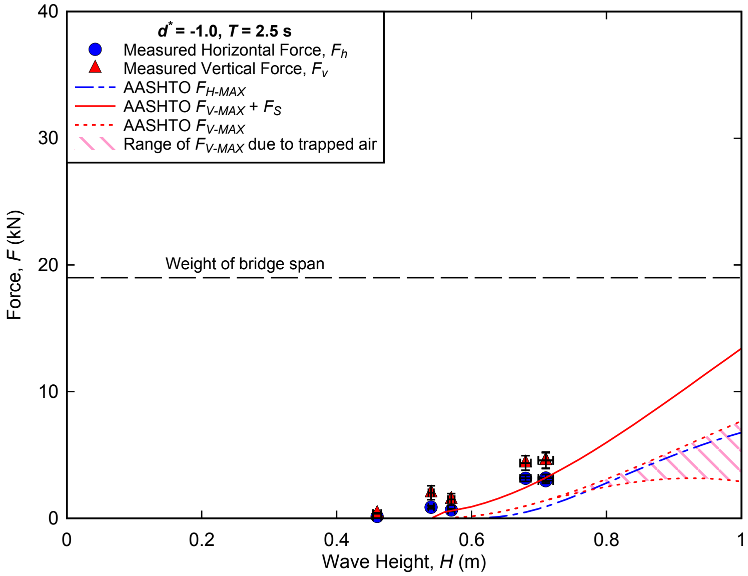

Figure G.1. Comparison of AASHTO guidelines with measured forces, d* = -1.0, T = 2.5 s.

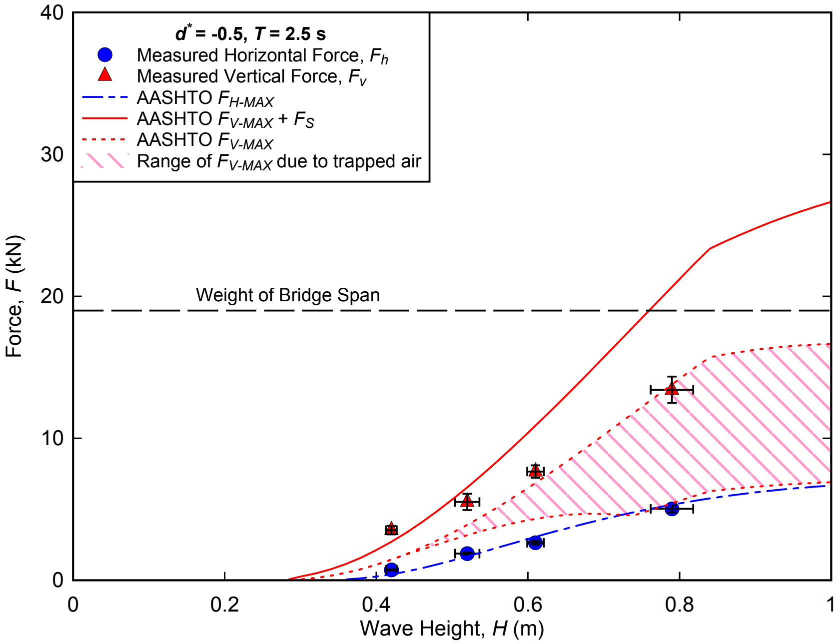

Figure G.2. Comparison of AASHTO guidelines with measured forces, d* = -0.5, T = 2.5 s.

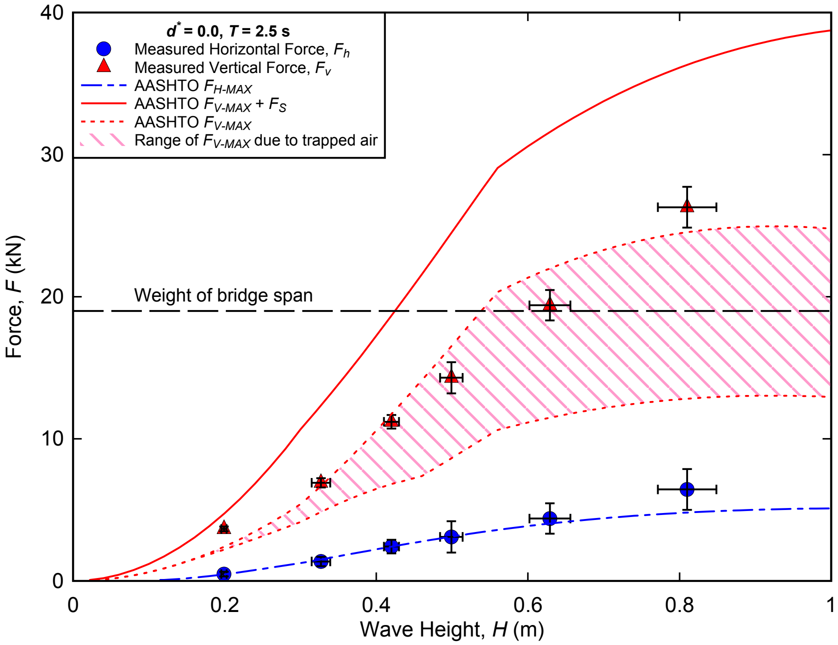

Figure G.3. Comparison of AASHTO guidelines with measured forces, d* = 0.0, T = 2.5 s.

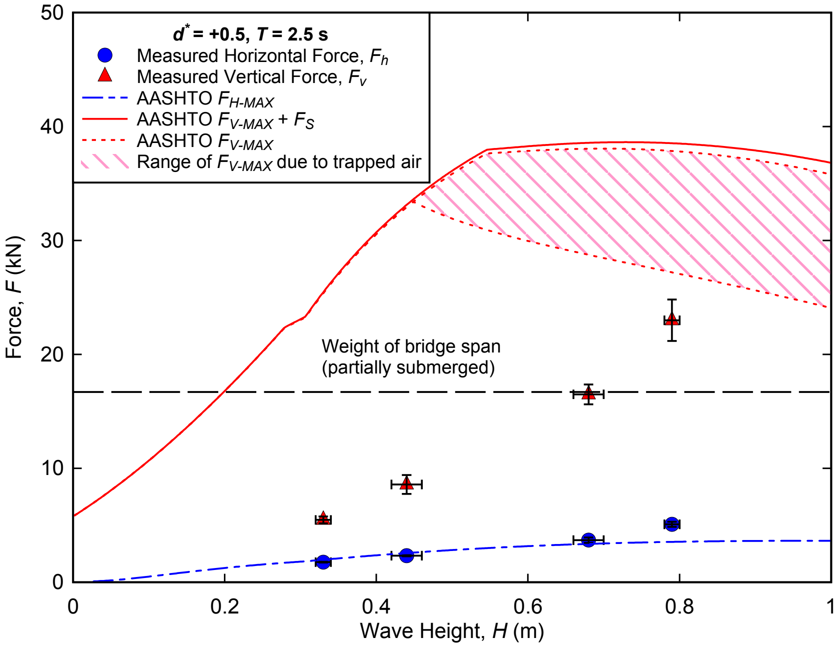

Figure G.4. Comparison of AASHTO guidelines with measured forces, d* = +0.5, T = 2.5 s.

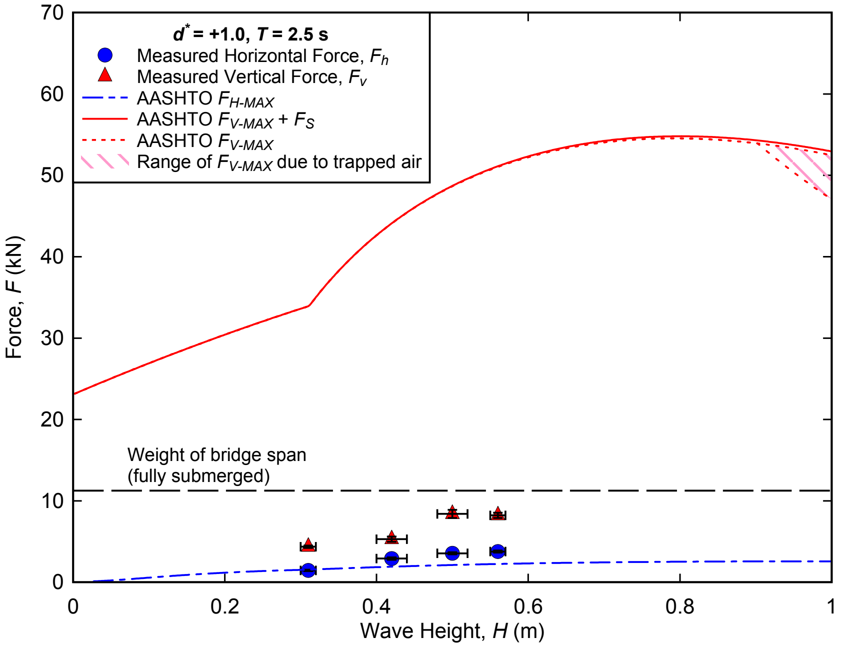

Figure G.5. Comparison of AASHTO guidelines with measured forces, d* = +1.0, T = 2.5 s.

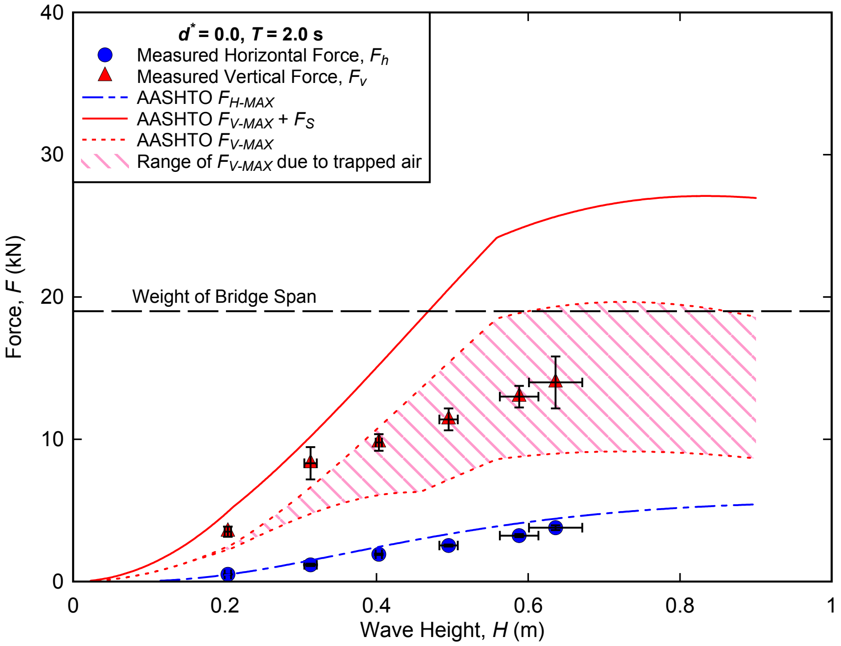

Figure G.6. Comparison of AASHTO guidelines with measured forces, d* = 0.0, T = 2.0 s.

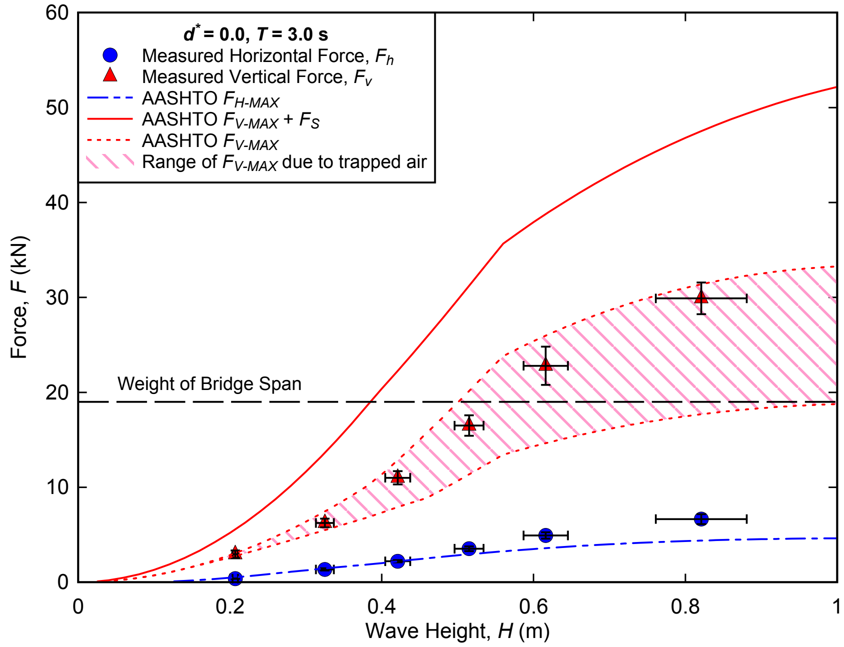

Figure G.7. Comparison of AASHTO guidelines with measured forces, d* = 0.0, T = 3.0 s.

APPENDIX H:

PROBABILITY DISTRIBUTION OF FORCES FOR RANDOM WAVE TRIALS

Table H-1. Summary of probability distribution analysis for random wave tests $d^* = 0.5$

			Horizontal Forces					Vertical Forces				
Trial	Hs	Tp	N	Distribution	A	B	R	N	Distribution	A	B	R
1201	0.26	2.0	3	FT-II k= 2.5	0.379	-1.029	0.962	6	FT-II k= 2.5	0.106	0.674	0.921
1202	0.28	2.5	5	Weibull k= 1.4	1.523	-1.814	0.949	7	FT-II k= 2.5	0.171	0.377	0.921
1203	0.29	2.9	5	Weibull k= 2.0	1.323	-0.659	0.986	9	FT-II k= 2.5	0.116	0.740	0.921
1204	0.33	2.1	10	FT-II k= 2.5	0.262	-0.167	0.962	14	Weibull k= 2.0	1.428	-0.992	0.968
1205	0.35	2.5	15	FT-II k= 5.0	0.262	0.468	0.852	10	Weibull k= 2.0	2.099	-2.031	0.968
1206	0.38	3.0	18	Weibull k= 1.4	0.619	0.066	0.949	16	Weibull k= 2.0	1.101	-0.497	0.968
1208	0.37	3.0	18	FT-II k= 2.5	0.103	0.832	0.962	26	Weibull k= 2.0	1.439	-0.972	0.968
1209	0.40	1.9	21	FT-II k= 2.5	0.123	0.705	0.962	21	Weibull k= 2.0	1.246	-0.770	0.968
1210	0.43	2.4	18	Weibull k= 2.0	2.334	-2.467	0.986	25	Weibull k= 2.0	1.232	-0.736	0.968
1211	0.46	3.0	24	Weibull k= 2.0	1.502	-1.119	0.986	24	FT-II k= 5.0	0.193	0.628	0.949
1212	0.40	2.0	6	Weibull k= 1.0	0.886	-0.877	0.949	6	FT-II k= 5.0	0.379	-0.098	0.949
1213	0.50	2.6	27	FT-II k= 5.0	0.234	0.468	0.852	30	Weibull k= 2.0	1.126	-0.548	0.968
1214	0.55	3.0	32	Weibull k= 1.4	0.578	0.095	0.949	34	Weibull k= 1.0	0.293	0.436	0.986

Table H-2. Summary of probability distributions for random waves at $p^* = 0$

			Horizontal Forces					Vertical Forces				
Trial	Hs	Tp	N	Distribution	A	B	R	N	Distribution	A	B	R
1301	0.37	1.8	26	Weibull k= 2.0	0.963	-0.324	0.981	28	Weibull k= 2.0	0.501	0.362	0.972
1302	0.35	2.1	45	FT-II k= 10.0	0.220	0.588	0.971	41	FT-II k= 10.0	0.152	0.742	0.985
1303	0.33	2.1	42	Weibull k= 1.4	0.763	-0.239	0.994	45	Weibull k= 2.0	0.974	-0.353	0.972
1304	0.38	1.9	45	Weibull k= 1.4	0.620	0.001	0.994	44	Weibull k= 2.0	0.588	0.223	0.972
1305	0.33	1.9	25	Weibull k= 2.0	1.943	-1.832	0.981	27	FT-I	0.235	0.593	0.965
1306	0.35	1.9	40	FT-II k= 3.33	0.125	0.765	0.994	42	Weibull k= 2.0	0.993	-0.366	0.972
1307	0.34	2.0	39	Weibull k= 2.0	1.578	-1.297	0.981	44	Weibull k= 2.0	0.837	-0.127	0.972
1308	0.36	1.9	15	Weibull k= 1.0	0.543	-0.119	0.990	13	Weibull k= 2.0	0.827	-0.074	0.972
1309	0.35	2.0	43	Weibull k= 2.0	1.292	-0.817	0.981	42	Weibull k= 2.0	0.744	0.002	0.972
1310	0.36	2.1	43	Weibull k= 2.0	0.801	-0.037	0.981	41	Weibull k= 2.0	0.824	-0.152	0.972
1311	0.34	1.9	31	Weibull k= 1.4	1.269	-1.267	0.994	42	Weibull k= 2.0	0.855	-0.110	0.972
1312	0.35	2.1	24	FT-II k= 2.5	0.128	0.633	0.983	31	Weibull k= 1.4	0.568	0.074	0.939
1314	0.47	2.1	51	Weibull k= 2.0	0.945	-0.258	0.981	40	Weibull k= 1.4	0.388	0.375	0.939
1315	0.55	2.5	49	Weibull k= 2.0	0.994	-0.320	0.981	50	Weibull k= 2.0	0.563	0.271	0.972
1316	0.39	2.4	46	Weibull k= 2.0	1.279	-0.839	0.981	46	Weibull k= 2.0	0.903	-0.270	0.972
1317	0.41	2.9	47	Weibull k= 0.75	0.255	0.326	0.946	39	FT-II k= 5.0	0.177	0.568	0.975
1318	0.58	2.9	40	Weibull k= 2.0	1.033	-0.450	0.981	42	Weibull k= 1.4	0.416	0.337	0.939
1319	0.64	2.5	24	Weibull k= 2.0	0.620	0.201	0.981	24	Weibull k= 2.0	0.413	0.481	0.972
1320	0.70	2.9	47	Weibull k= 2.0	0.729	0.018	0.981	44	Weibull k= 2.0	0.636	0.143	0.972
1321	0.74	3.6	45	Weibull k= 2.0	0.845	-0.167	0.981	44	Weibull k= 2.0	0.686	0.066	0.972
1323	0.58	3.5	40	Weibull k= 2.0	1.311	-0.847	0.981	39	Weibull k= 2.0	0.922	-0.293	0.972

Table H-3. Summary of probability distribution analysis for random waves at $p^* = +0.5$

			Horizontal Forces					Vertical Forces				
Trial	Hs	Tp	N	Distribution	A	B	R	N	Distribution	A	B	R
1401	0.39	2.2	49	Weibull k= 2.0	0.814	-0.168	0.988	42	Weibull k= 1.4	0.394	0.354	0.976
1402	0.41	2.5	47	Weibull k= 2.0	0.895	-0.268	0.988	34	Weibull k= 2.0	1.043	-0.561	0.986
1403	0.44	2.8	43	Weibull k= 2.0	1.087	-0.562	0.988	35	FT-II k= 10.0	0.230	0.475	0.965
1404	0.49	2.2	56	Weibull k= 2.0	0.609	0.176	0.988	52	Weibull k= 2.0	0.594	0.158	0.986
1405	0.56	2.4	48	Weibull k= 2.0	0.717	0.029	0.988	37	Weibull k= 2.0	1.115	-0.618	0.986
1406	0.58	2.9	43	Weibull k= 2.0	1.061	-0.512	0.988	36	Weibull k= 2.0	1.663	-1.480	0.986
1407	0.43	1.9	50	Weibull k= 1.4	0.528	0.114	0.986	47	Weibull k= 2.0	0.667	0.091	0.986
1408	0.47	2.4	51	FT-II k= 10.0	0.200	0.583	0.925	38	FT-II k= 5.0	0.181	0.556	0.981
1409	0.53	2.9	45	Weibull k= 1.0	0.307	0.394	0.991	42	FT-II k= 5.0	0.192	0.539	0.981
1410	0.31	2.1	49	Weibull k= 0.75	0.169	0.528	0.982	43	Weibull k= 2.0	0.860	-0.269	0.986
1411	0.33	2.5	47	Weibull k= 2.0	0.660	0.122	0.988	42	Weibull k= 2.0	0.630	0.091	0.986
1412	0.33	3.1	44	Weibull k= 1.4	0.477	0.191	0.986	45	Weibull k= 2.0	0.646	0.078	0.986

Table H-4. Summary of probability distributions [illegible] $p^* = 1 + 0$

			Horizontal Forces					Vertical Forces				
Trial	Hs	Tp	N	Distribution	A	B	R	N	Distribution	A	B	R
1501	0.30	1.9	53	Weibull k= 2.0	1.016	-0.446	0.985	37	Weibull k= 1.0	0.354	0.251	0.979
1502	0.31	2.5	39	Weibull k= 2.0	1.019	-0.452	0.985	40	Weibull k= 1.4	0.428	0.297	0.997
1503	0.32	3.1	47	FT-I	0.195	0.632	0.984	42	Weibull k= 2.0	0.746	-0.059	0.993
1504	0.36	2.2	54	Weibull k= 2.0	0.877	-0.193	0.985	46	FT-II k= 10.0	0.151	0.705	0.992
1505	0.40	2.5	47	Weibull k= 1.4	0.478	0.238	0.984	46	Weibull k= 1.4	0.366	0.407	0.997
1506	0.41	2.8	51	Weibull k= 1.0	0.204	0.618	0.991	42	FT-II k= 5.0	0.116	0.723	0.987
1507	0.41	2.0	54	Weibull k= 2.0	0.813	-0.143	0.985	43	Weibull k= 1.0	0.373	0.171	0.979
1508	0.48	2.5	43	Weibull k= 2.0	0.747	-0.069	0.985	42	Weibull k= 1.0	0.228	0.535	0.979
1509	0.49	3.1	40	Weibull k= 0.75	0.141	0.625	0.990	38	Weibull k= 1.4	0.595	-0.006	0.997

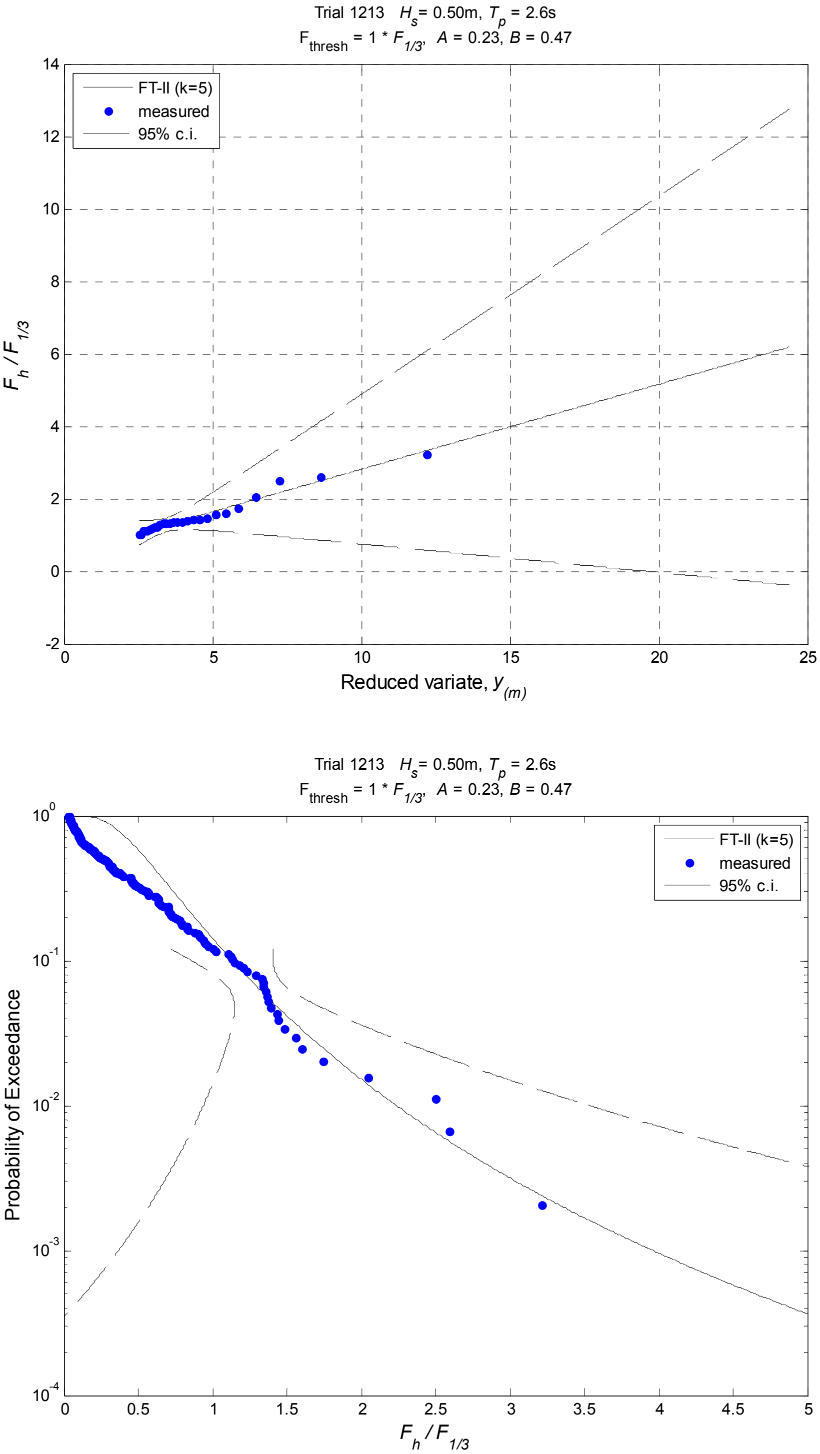

Figure H.8. Exceedance probabilities for normalized horizontal forces, d* = -0.5, Hs = 0.50 m, Tp = 2.6s.

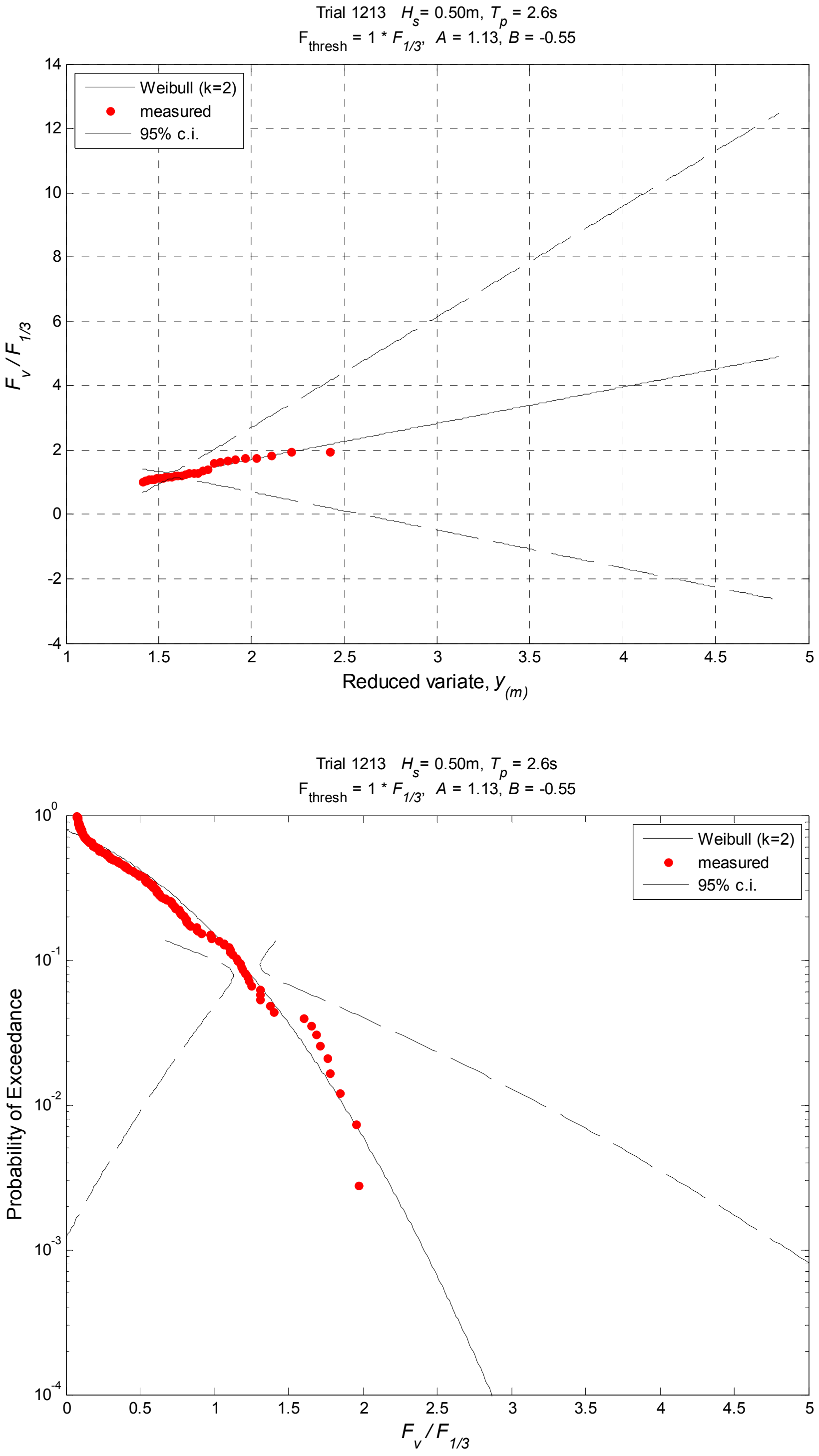

Figure H.9. Exceedance probabilities for normalized vertical forces, d* = -0.5, Hs = 0.50 m, Tp = 2.6s.

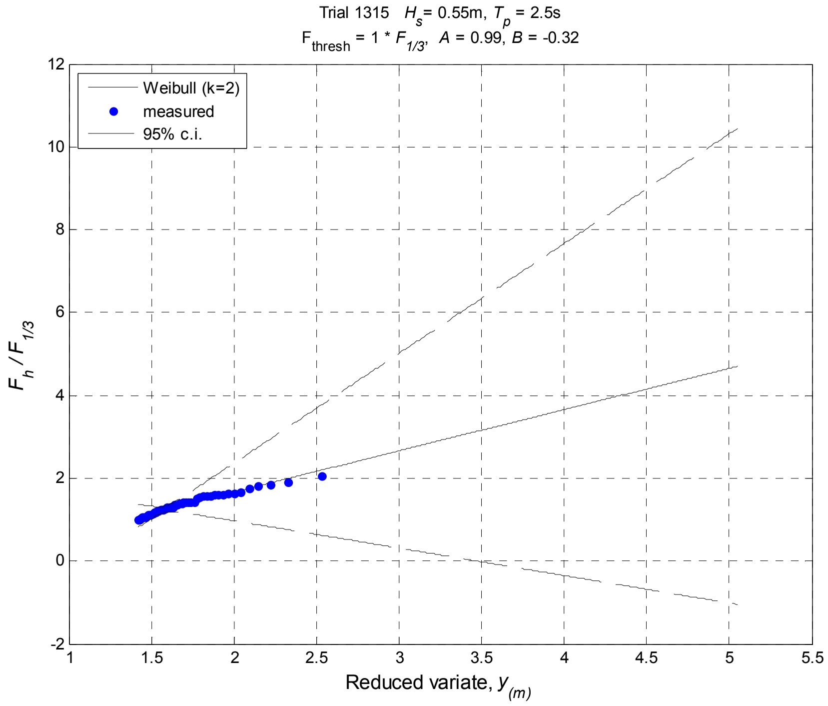

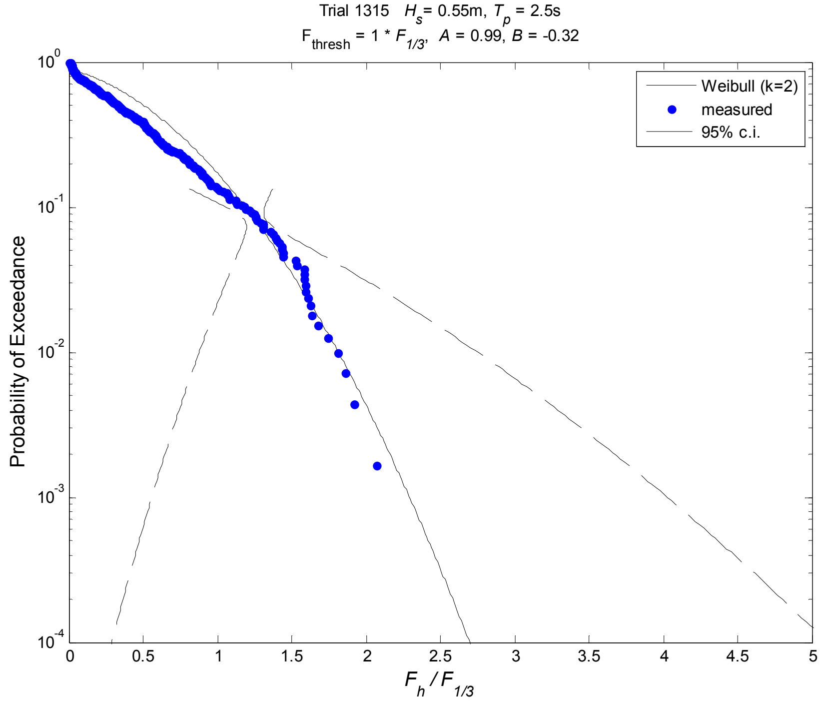

Figure H.10. Exceedance probabilities for normalized horizontal forces, d* = 0.0, Hs = 0.55 m, Tp = 2.5s.

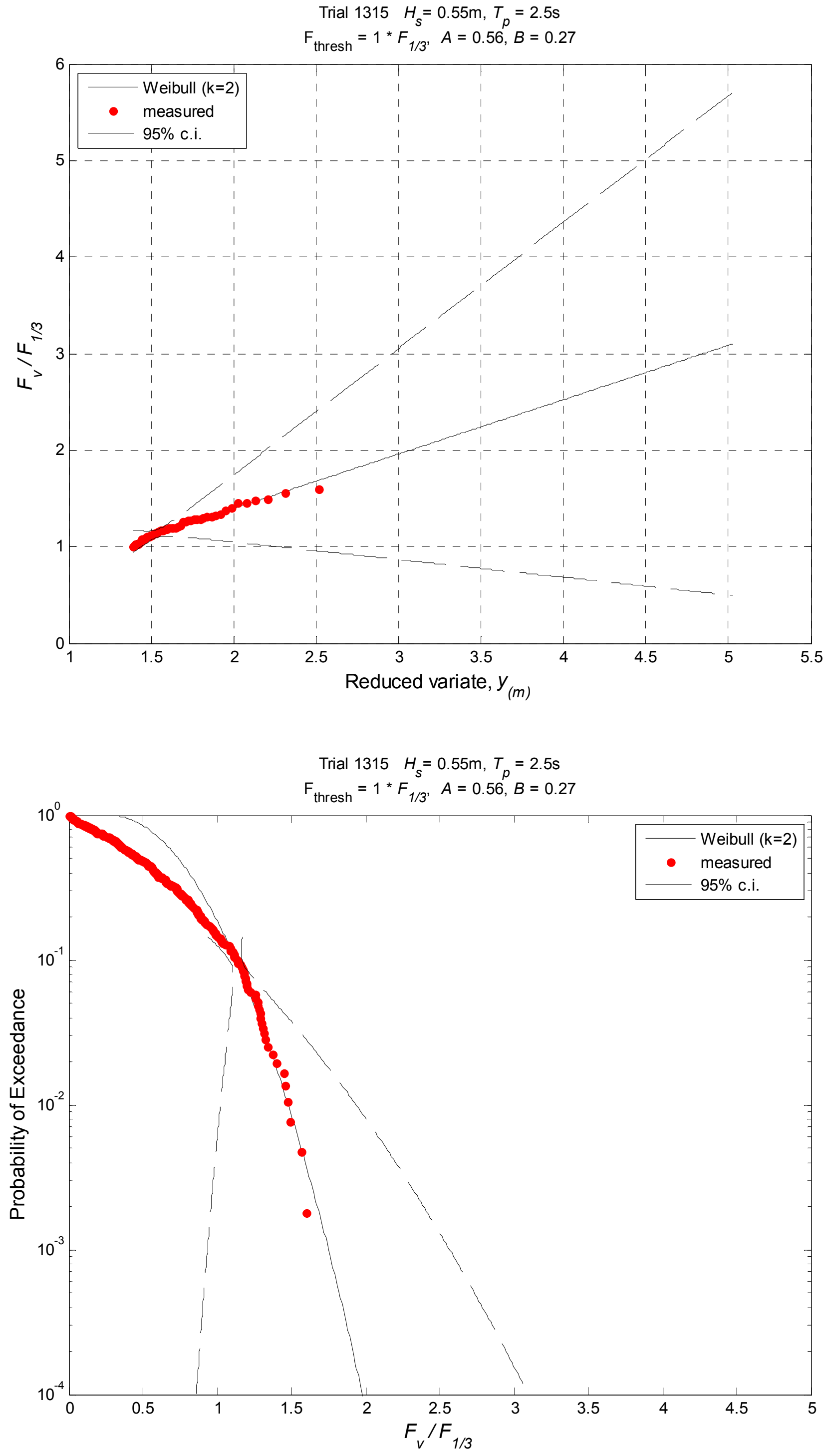

Figure H.11. Exceedance probabilities for normalized vertical forces, d* = 0.0, Hs = 0.55 m, Tp = 2.5s.

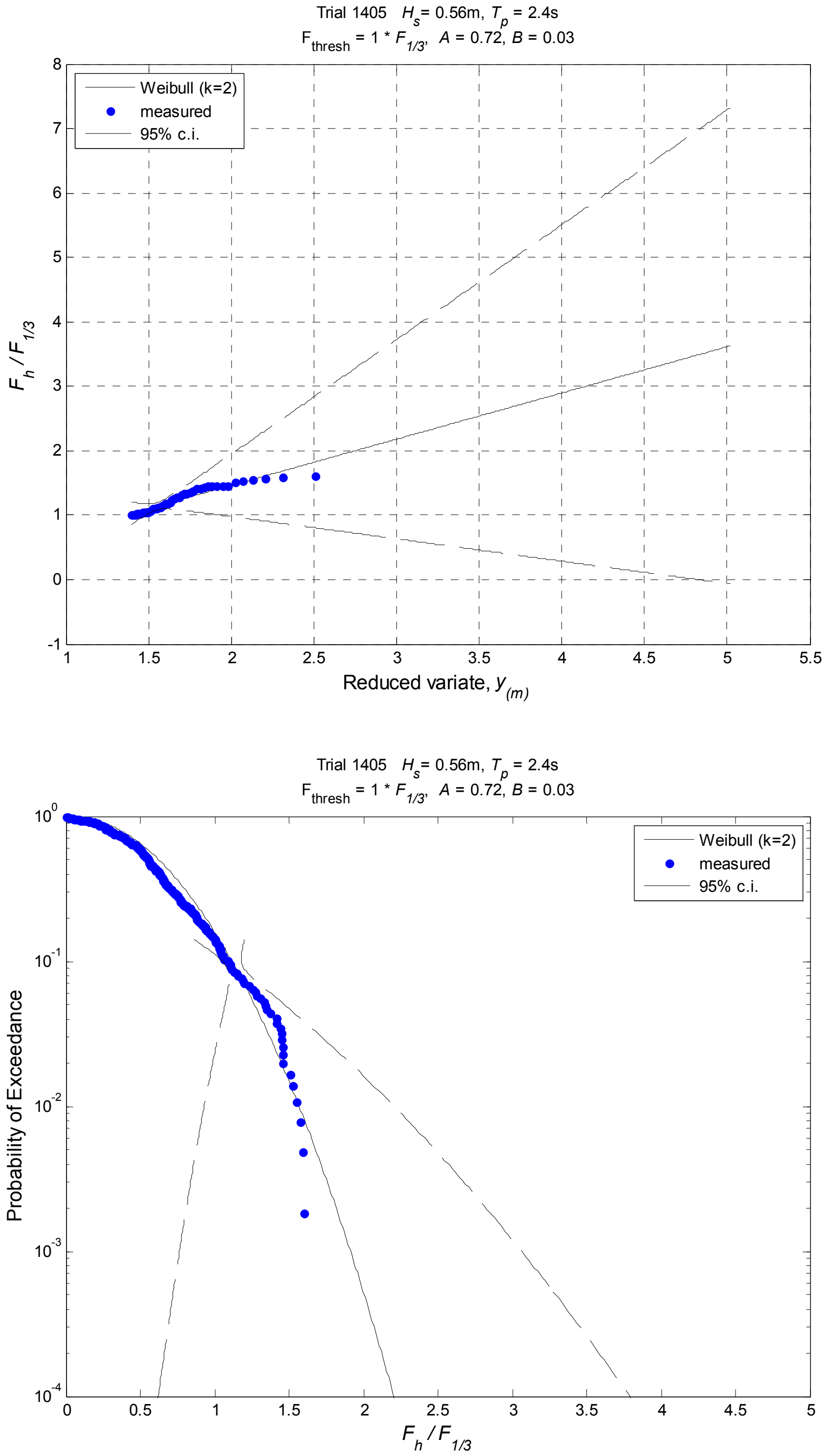

Figure H.12. Exceedance probabilities for normalized horizontal forces, d* = +0.5, Hs = 0.56 m, Tp = 2.4s.

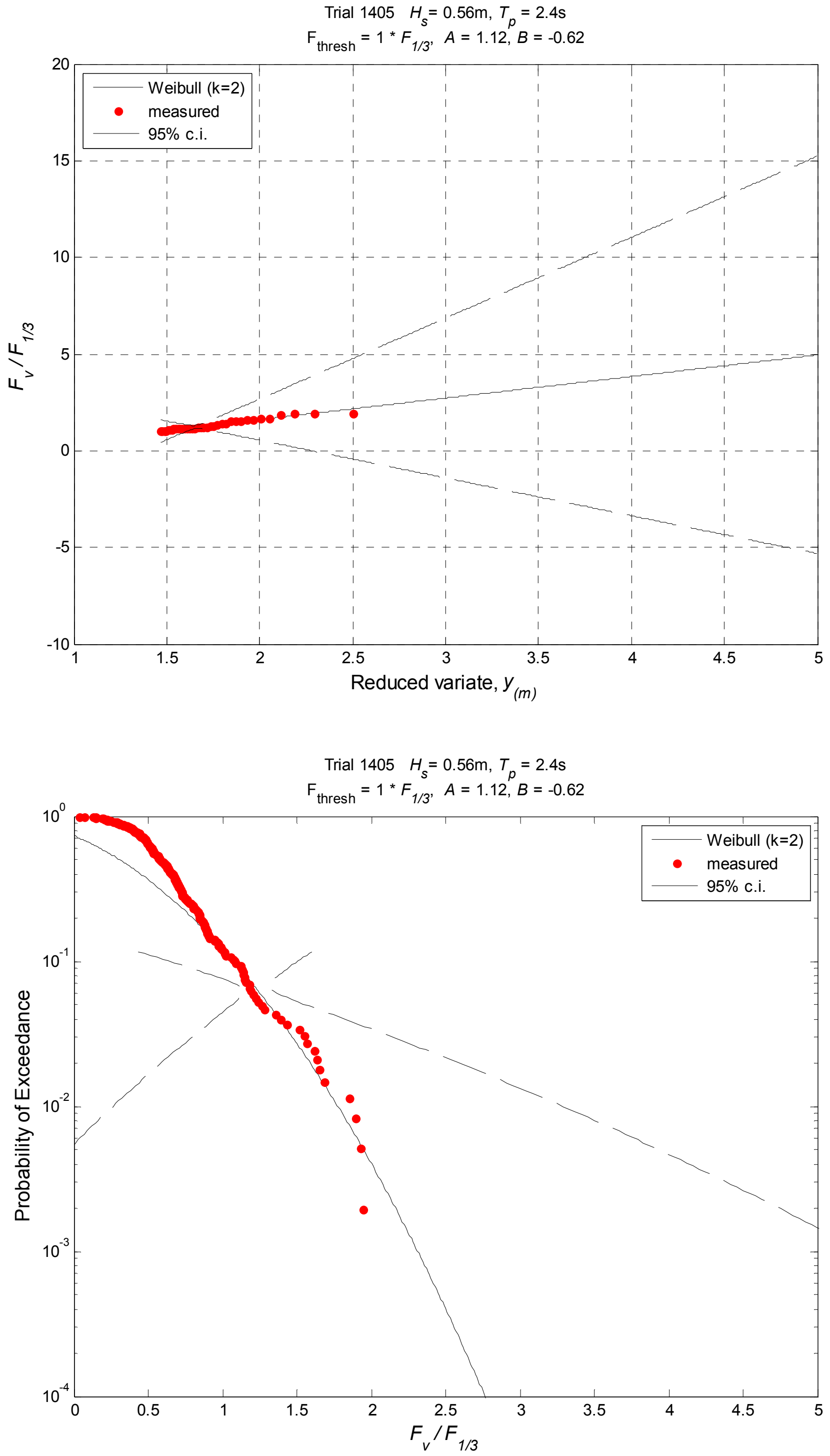

Figure H.13. Exceedance probabilities for normalized vertical forces, d* = +0.5, Hs = 0.56 m, Tp = 2.4s.

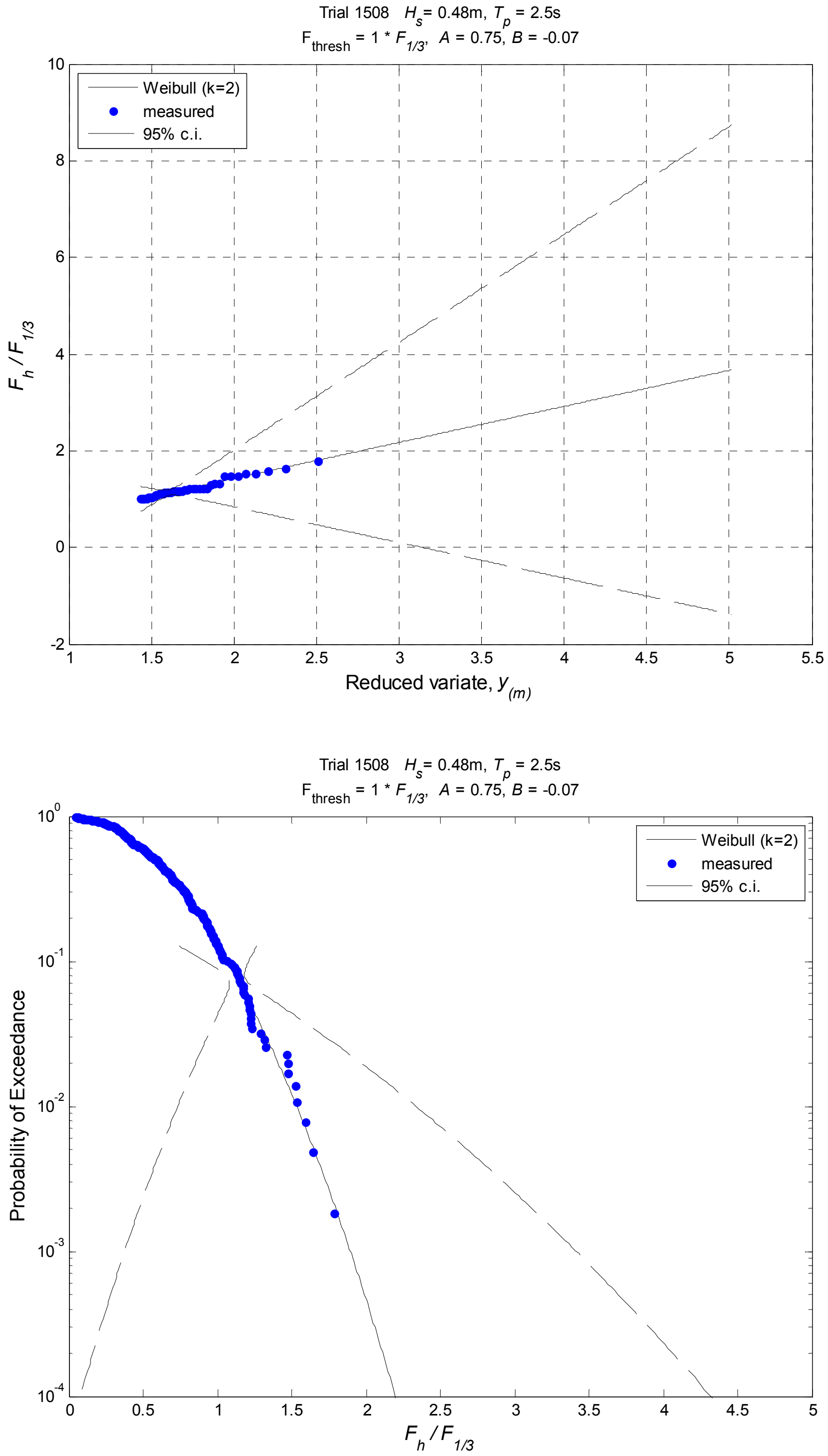

Figure H.14. Exceedance probabilities for normalized horizontal forces, d* = +1.0, Hs = 0.48 m, Tp = 2.5s.

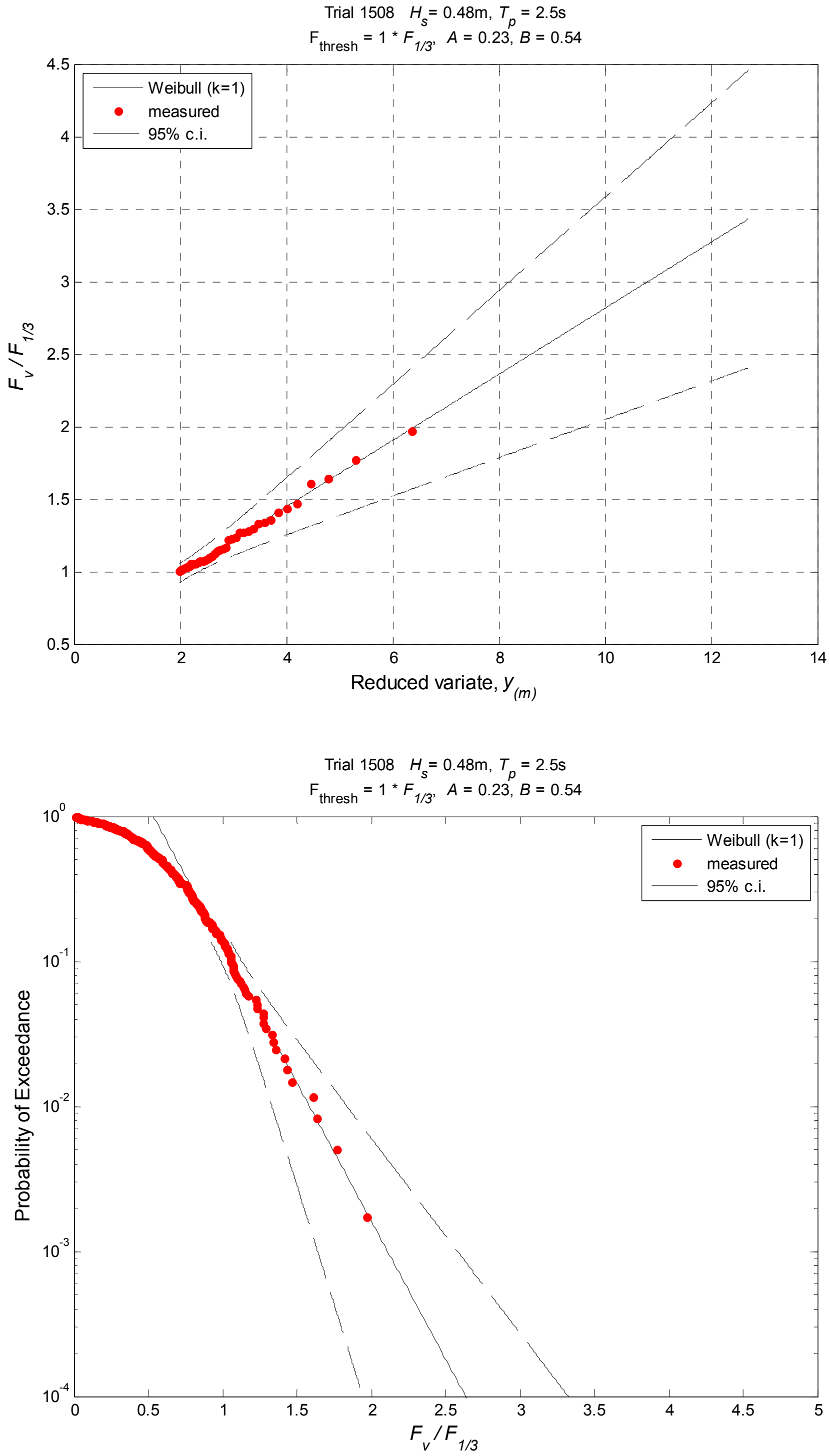

Figure H.15. Exceedance probabilities for normalized vertical forces, d* = +1.0, Hs = 0.48 m, Tp = 2.5s.

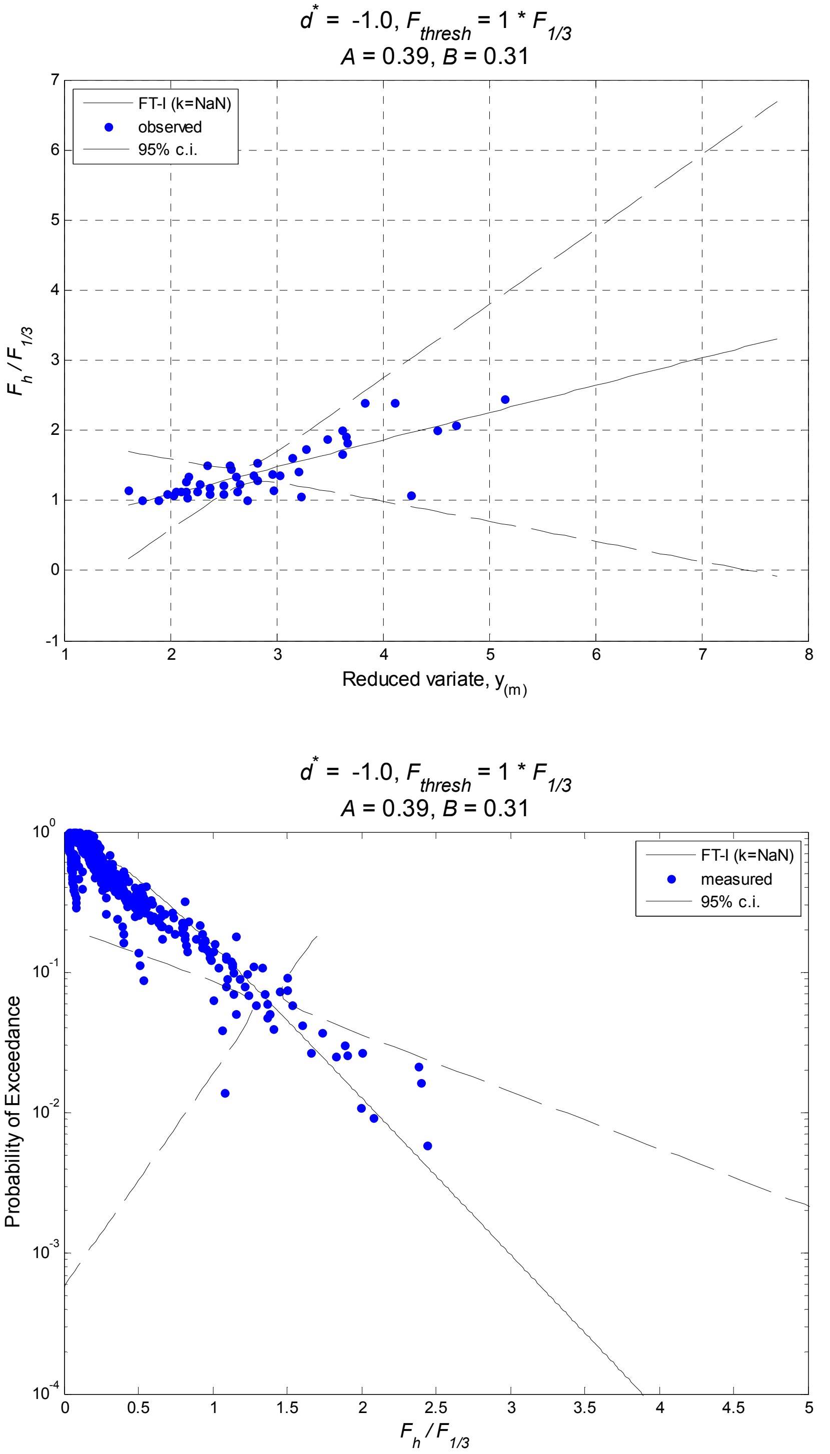

Figure H.16. Exceedance probability for normalized horizontal forces, d* = -1.0

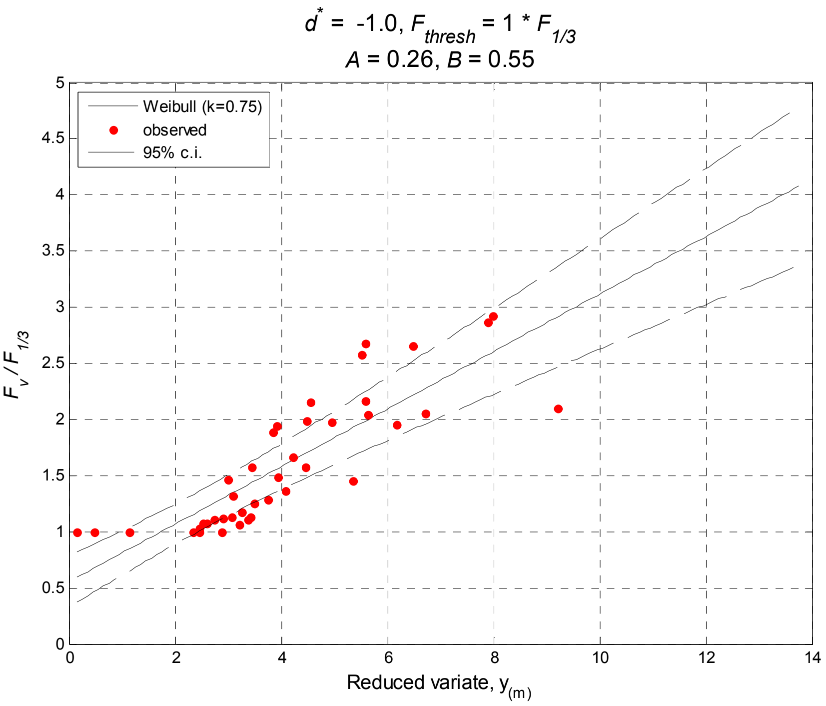

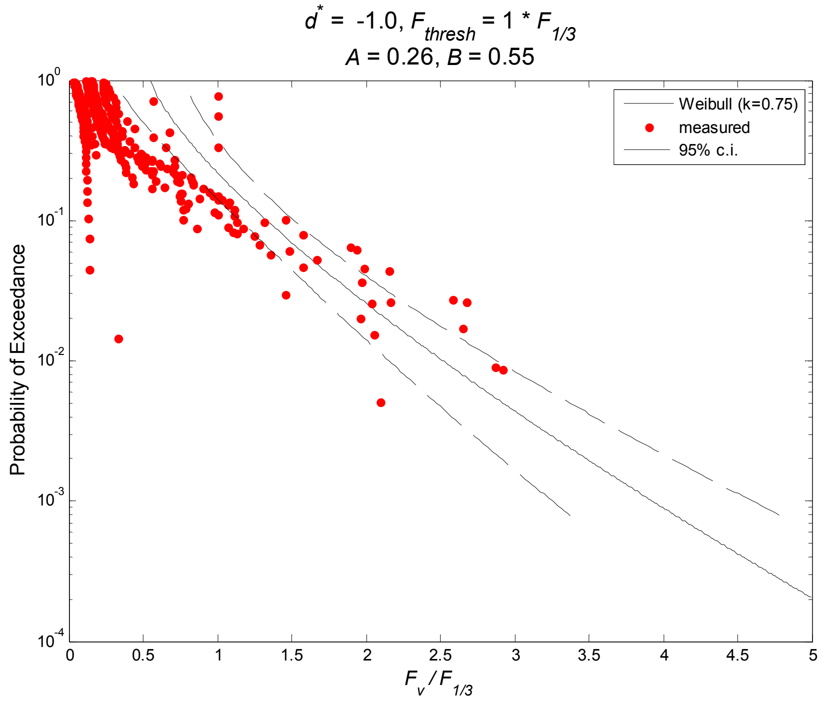

Figure H.17. Exceedance probability for normalized vertical forces, d* = -1.0

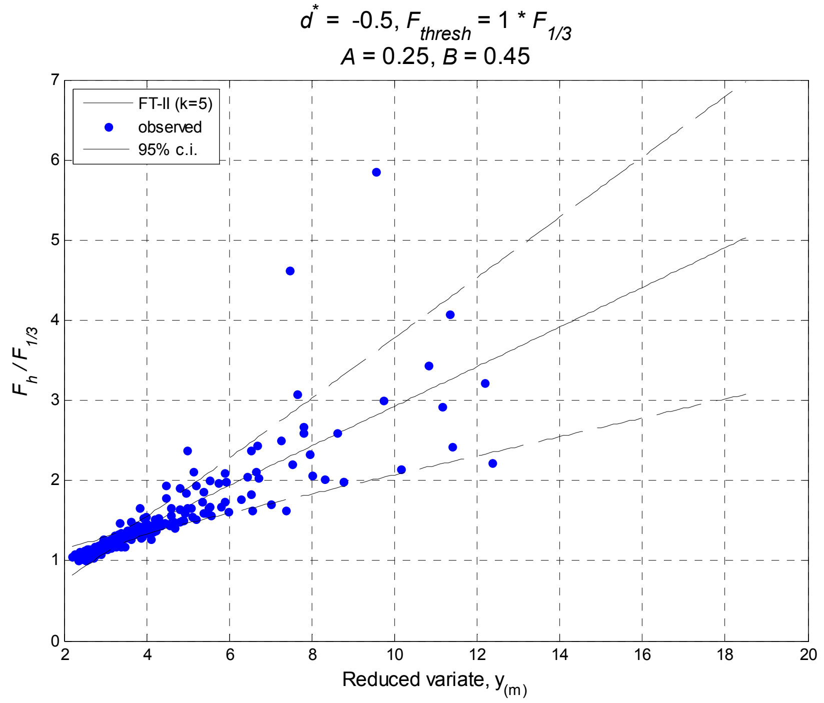

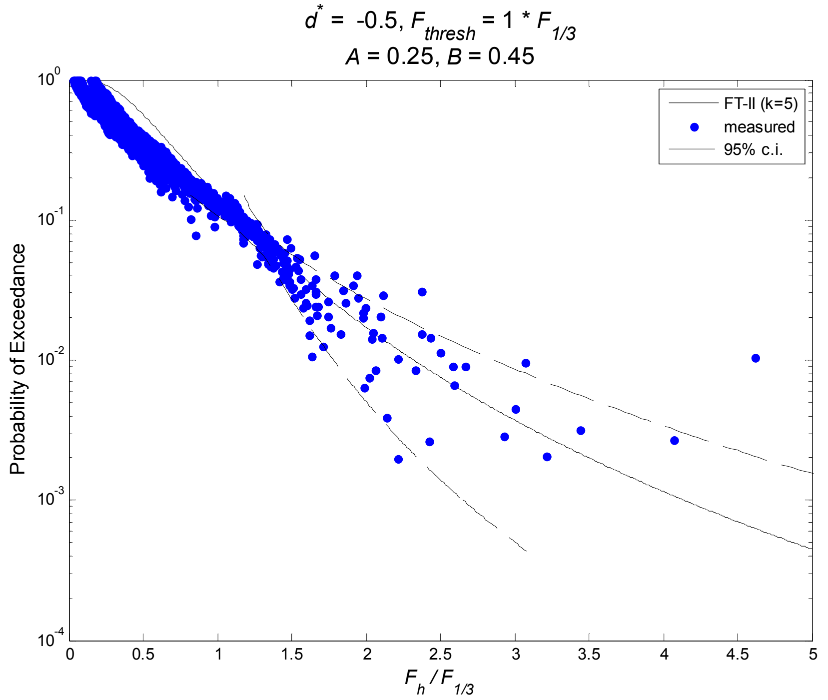

Figure H.18. Exceedance probability for normalized horizontal forces, d* = -0.5.

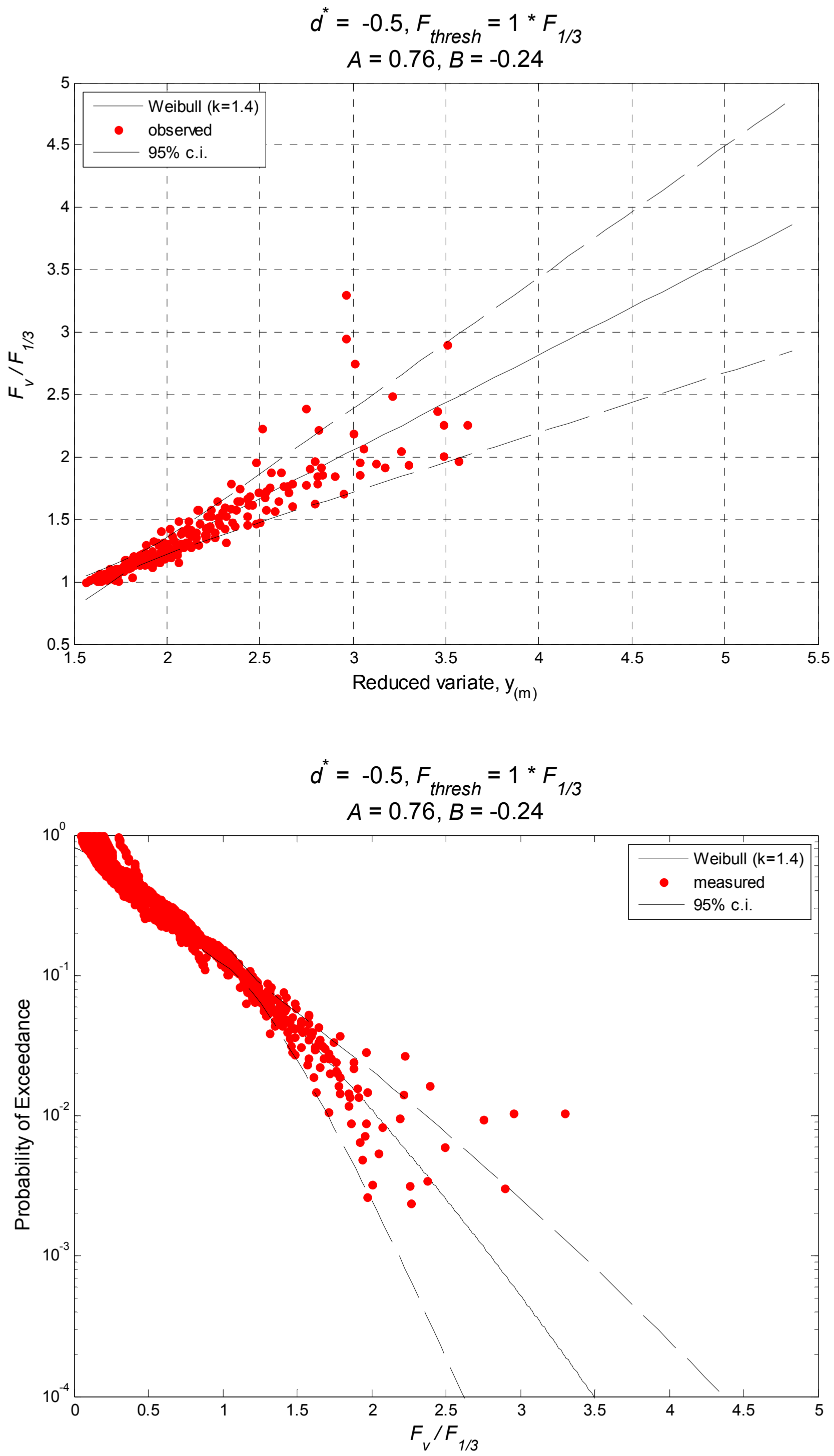

Figure H.19. Exceedance probability for normalized vertical forces, d* = -0.5.

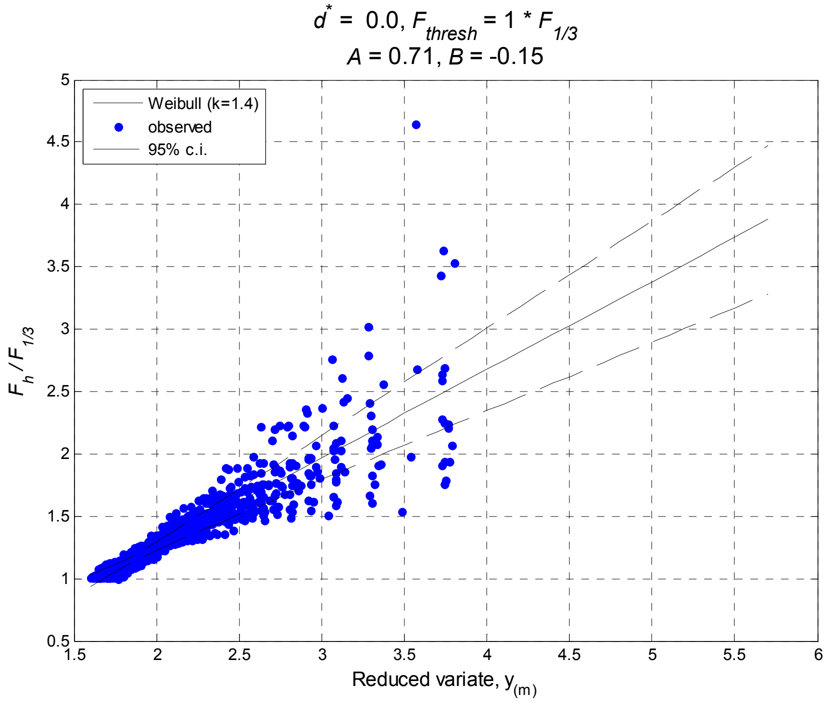

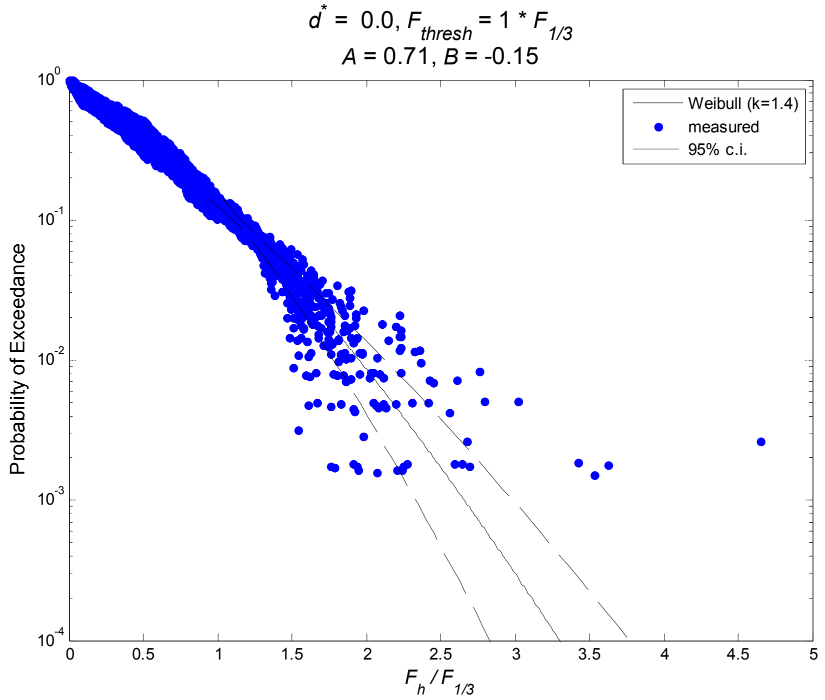

Figure H.20. Exceedance probability for normalized horizontal forces, d* = 0.0

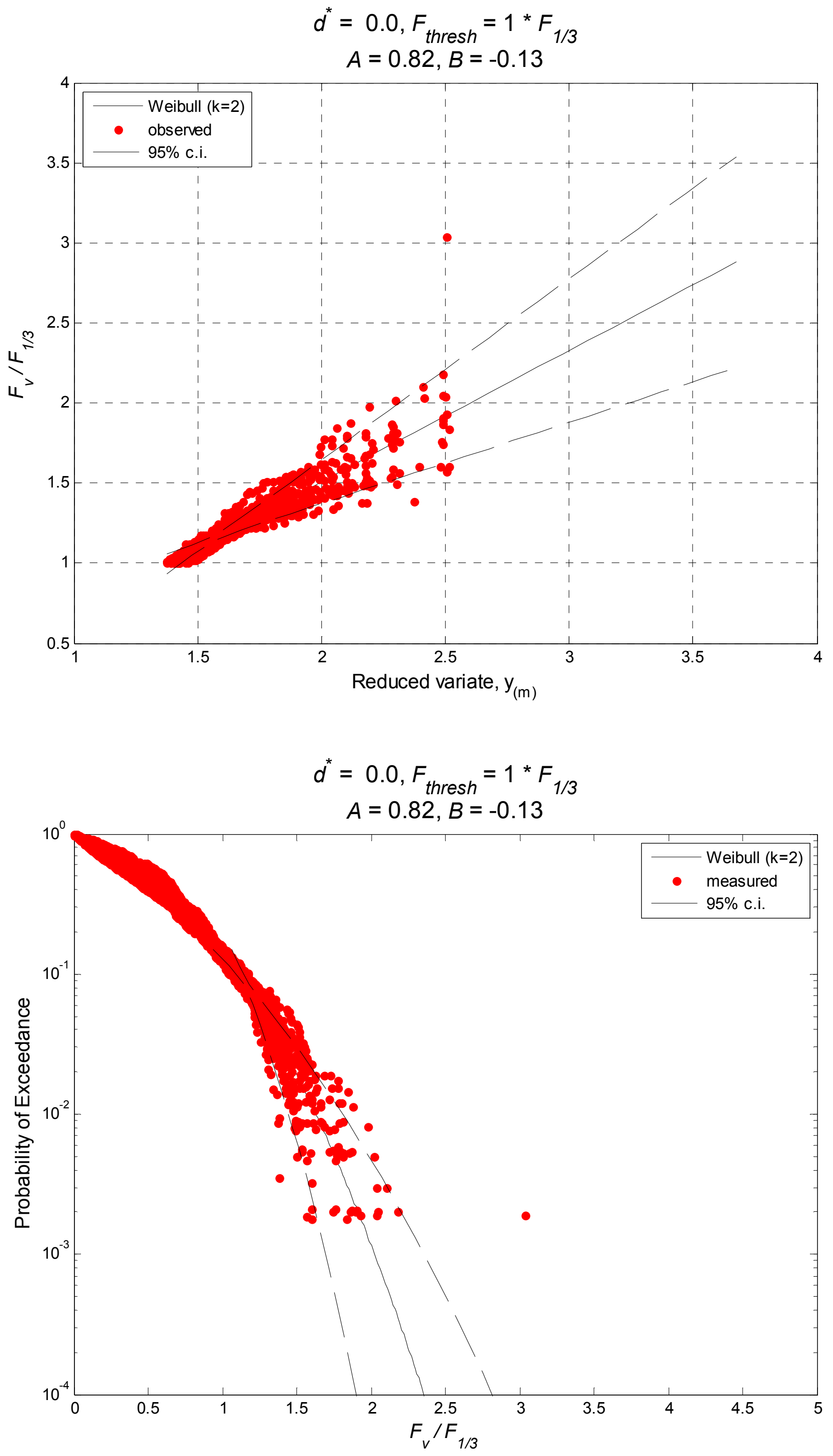

Figure H.21. Exceedance probability for normalized vertical forces, d* = 0.0

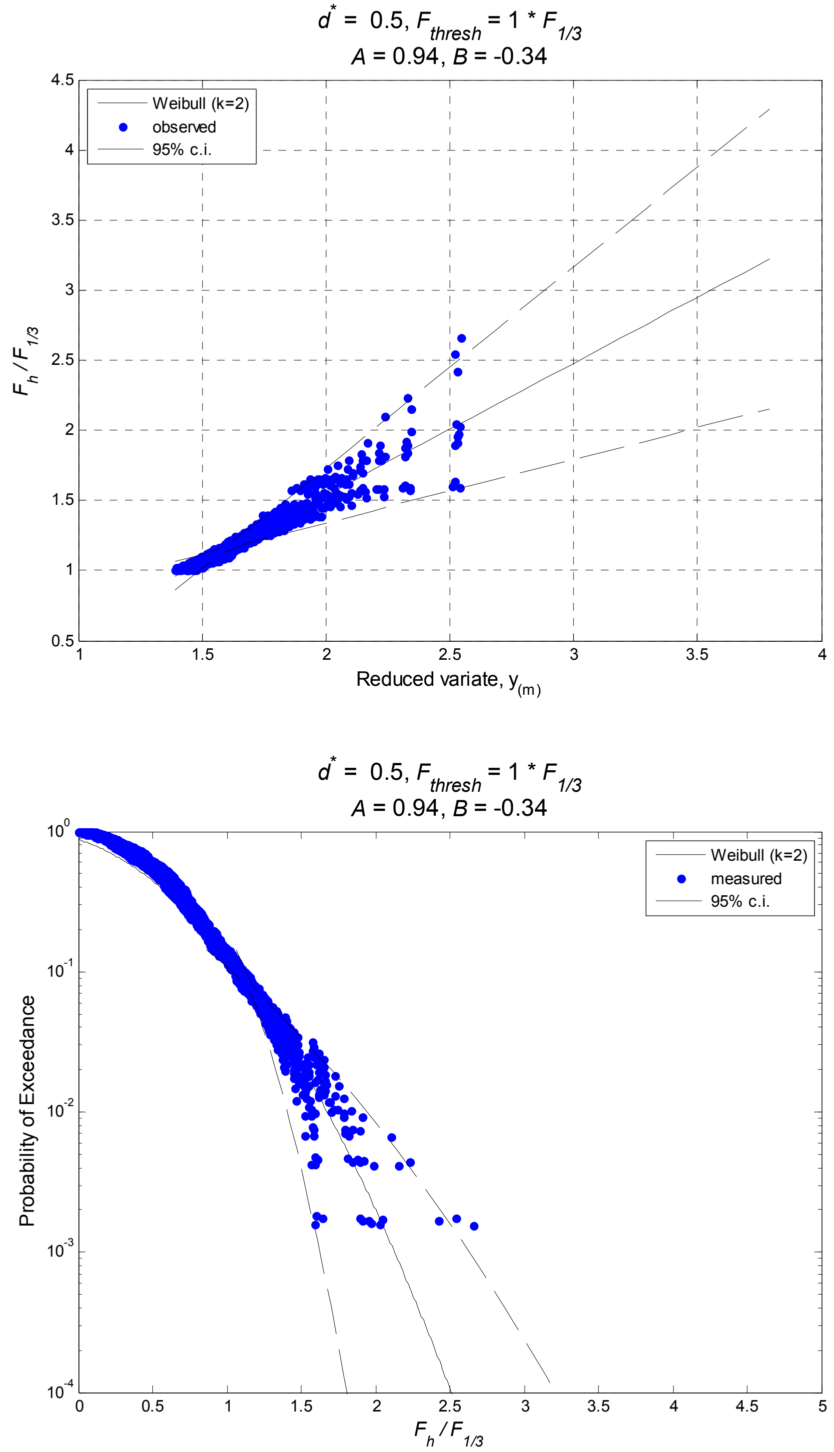

Figure H.22. Exceedance probability for normalized horizontal forces, d* = +0.5

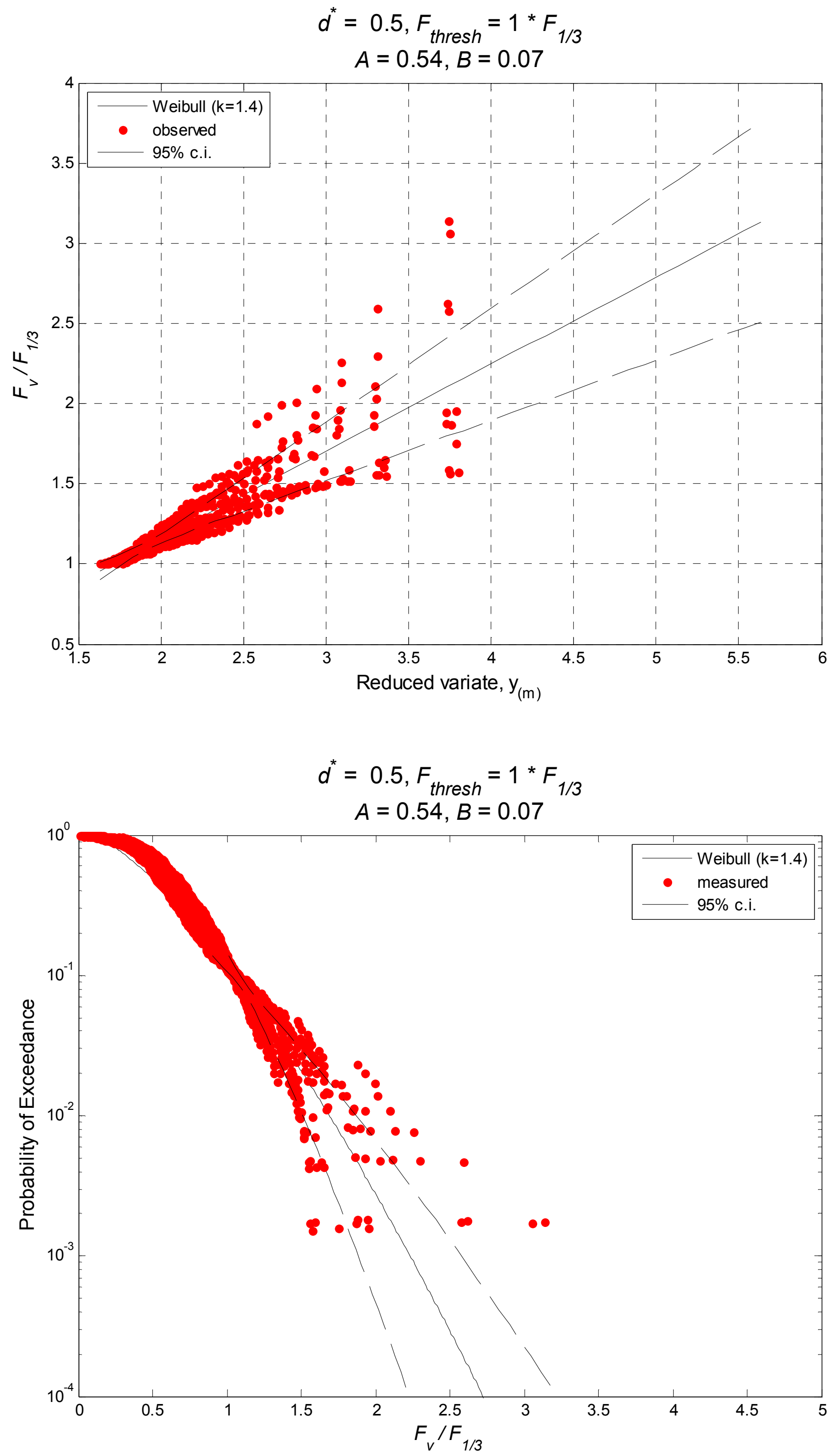

Figure H.23. Exceedance probability for normalized vertical forces, d* = +0.5

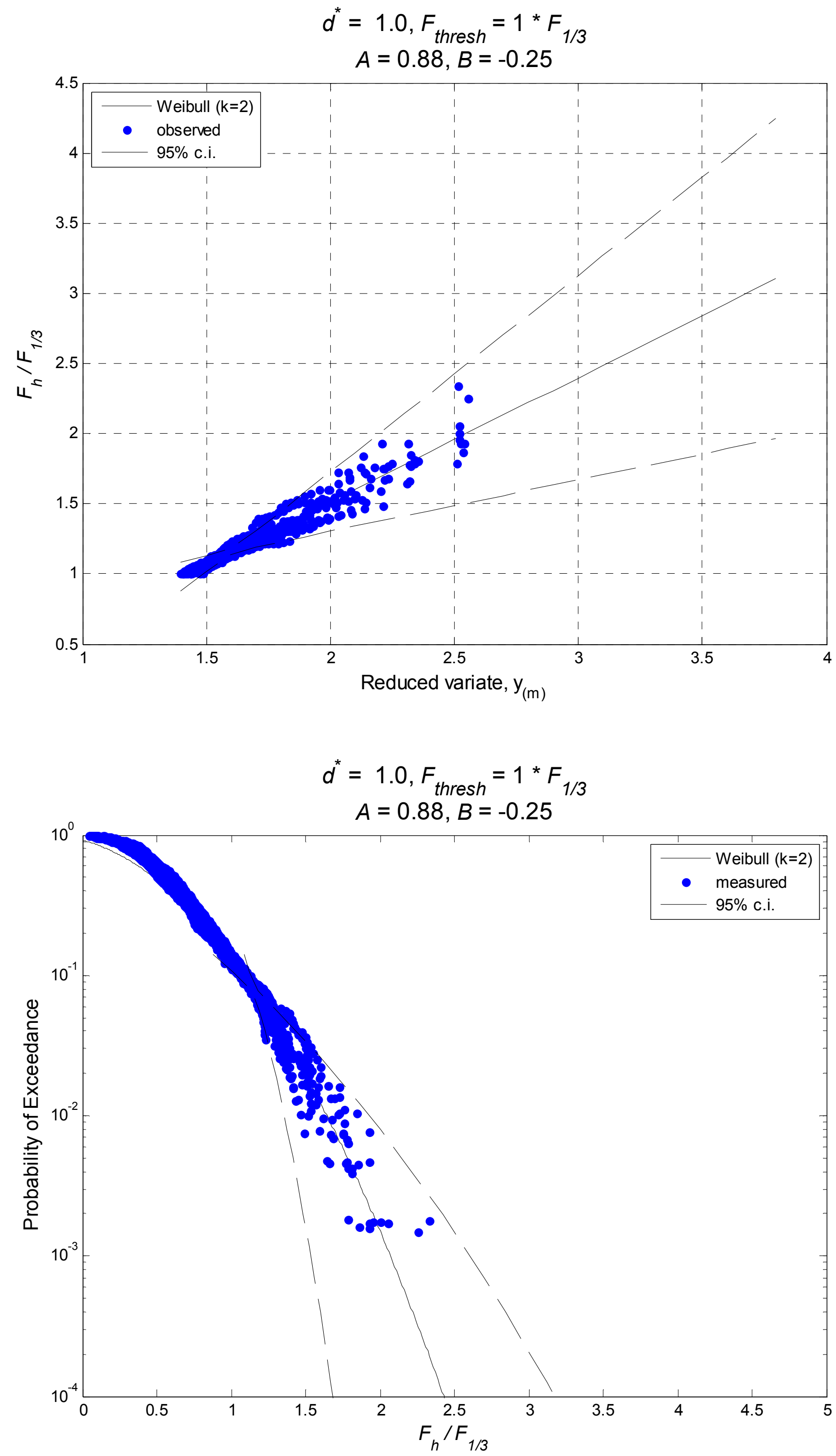

Figure H.24. Exceedance probability for normalized horizontal forces, d* = +1.0

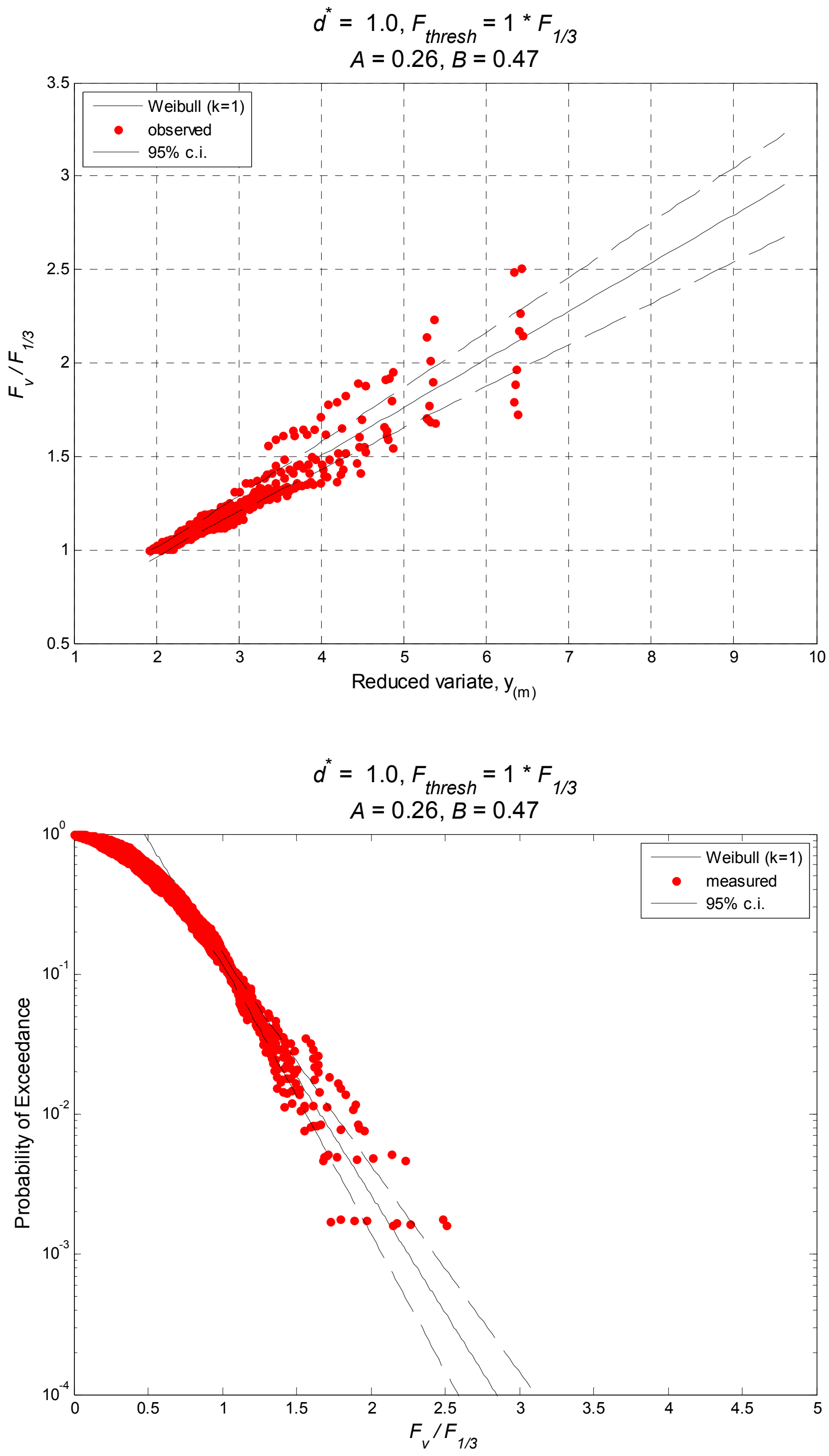

Figure H.25. Exceedance probability for normalized vertical forces, d* = +1.0

OTREC
OREGON TRANSPORTATION RESEARCH
AND EDUCATION CONSORTIUM

P.O. Box 751
Portland, OR 97207

OTREC is dedicated to stimulating and conducting collaborative multi-disciplinary research on multi-modal surface transportation issues, educating a diverse array of current practitioners and future leaders in the transportation field, and encouraging implementation of relevant research results.